Chapter 1

Introduction

1.1 Importance of Combustion Systems

Energy. Ever increasingly, the human race relies on energy to fulfil even the most basic of functions. Whether for heating or cooling, food production, lighting, transport, manufacture, or simply leisure, today's society demands the use of energy in a countless number of ways.

World energy consumption is projected to increase by 58% between 2001 and 2025 [43]. Over 85% of the energy is presently supplied through processes relying on combustion [111] and is a trend that appears will continue in the foreseeable future.

Figure 1.1 shows the energy production for each main energy source, and projections until the year 2025. The three main sources of energy are oil, natural gas, and coal — all of which are based on combustion. Over the prediction period, these three sources of energy are expected to continue dominating. Despite an expected growth of 1.9% annually between 2001–2025, renewable energy is only predicted to account for around 8% of the world's energy production [43].

Given that combustion is expected to continue to be the primary source of energy for supplying the world's demands, it is imperative that more efficient solutions which produce less pollutants are sought. Increasing efficiency is particularly important to address the issues of greenhouse warming and global climate change,

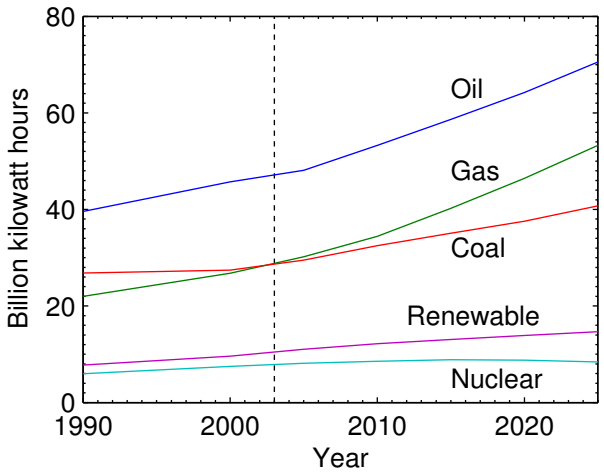

Figure 1.1: World energy production by source [43]

as well as looming fuel supply shortages. Improvements to combustion systems can only be achieved by advancing current understanding of the fundamental principles of these important devices.

Understanding of combustion has developed enormously, but it is not yet possible to create and solve models that truly simulate combustion systems. Even the most trivial situations involving turbulence can only be represented by approximations [111]. It is for these reasons that in order to further develop knowledge of combustion, experimental work is required to co-investigate the chemical and mechanical processes that occur [117].

1.2 Introduction to MILD Combustion

There is a continual requirement to improve and produce new combustion systems that lead to lower emissions, and reduce fuel consumption. Increasing efficiency plays a vital part in reducing emissions, most notably CO_2 emission, which is the main contributor to the greenhouse effect. Efficiency increase also has the important effect of reducing the demand for ever-diminishing fuel supplies. One technology that has the potential to meet these criteria is that known as Moderate or Intense Low oxygen Dilution (MILD) combustion.

The MILD combustion regime achieves a desirable combination of low pollutant

emissions and improved fuel savings. This is accomplished by simultaneously reducing the local oxygen concentration and increasing the temperature of the reactants used in the combustion. Generally this is performed by recirculating exhaust products back into the furnace. Worth highlighting is that although the oxygen levels used in MILD combustion are very low, furnaces are operated on a fuel-lean basis. By reducing the local oxygen concentration, the combustion reaction is impeded, leading to a distributed reaction zone which occupies a greater volume and therefore mass of gas. This in turn has the effect of creating a more uniform temperature distribution over the length of the flame. Distributing the reaction over a larger volume then decreases the temperature while maintaining the total heat production. A uniform temperature profile is typically advantageous for both heating and environmental perspectives.

A result of the reduced local oxygen concentration is that in order for the combustion reaction to occur, the temperature of the reactants must be increased. Preheating the air is often undesired, as it tends to increase peak flame temperatures and produce high emissions of some pollutants. However, the oxygen dilution associated with MILD combustion more than compensates for these unwanted effects introduced by preheating.

While the recirculation of exhaust gases is a long established technique to improve system efficiency, MILD combustion is very different. It is a well known fact that if the oxygen concentration of air is reduced, there becomes a point where combustion cannot be sustained. In MILD combustion the reactants are mixed with large quantities of products at the reaction zone. This draws much of the energy released from the reaction to a larger volume of gas, and can prevent its sustainability. Preheating of the mixture, usually through the recirculation of hot exhaust gases, helps to maintain the reaction even when the O_2 concentration locally is very low. It is the combination of the low oxygen and the preheating that gives MILD combustion it's unique features.

Due to the attractiveness of the MILD combustion regime, a better understanding of the processes involved is required before it can see widespread implementation.

1.3 Approach

In order to benefit from the many advantages of MILD combustion, it is necessary to better understand the reaction regime involved so that it may be applied to a variety of combustion systems. Although there has been some research previously conducted in the area of MILD combustion, most work has predominately concentrated on large-scale systems. This project seeks to differ from much of this existing research by using a well controlled experimental burner. The use of such a burner enables a wide range of combustion parameters to be easily varied, whereas the existing research has been limited in this respect. In addition, the use of an experimental burner enables advanced measurement techniques to be employed, which cannot be used effectively in existing systems. In this way, utilising an experimental burner will avoid the limitations of previous investigations, whilst simultaneously enabling the required conditions to be emulated.

The burner to be used is known as a Jet in Hot Coflow (JHC) burner, which is shown schematically in Figure 1.2. This burner consists of an insulated central fuel jet, and a coflow stream from an annulus with a secondary burner mounted upstream of the exit plane. The secondary burner provides hot combustion products, which are mixed with air and nitrogen to enable the composition of the coflow to be varied. The burner allows optical access to measure the reaction region, including conditions at the exit plane.

The use of a secondary burner upstream of the primary burner for use in experimental burners has previously been employed (e.g. [31, 87]) and enables decoupling of the chemical kinetics from a complex recirculating flow [21].

For experimental work in the field of combustion to be useful, it is important for it to have well defined boundary conditions and relatively simple geometric configurations [7]. The JHC burner meets these criteria, and while the burner design is not directly applicable to industrial situations, it facilitates the observation of MILD combustion under controlled conditions. It is only by better understanding the fundamental aspects in such controlled conditions that it will be possible to better understand more complex systems.

A combination of laser diagnostic techniques is used to simultaneously and instan-

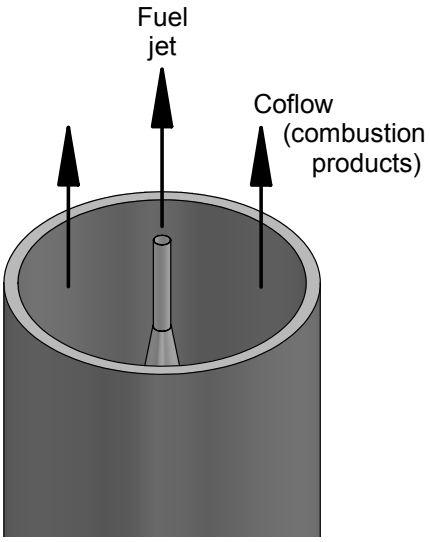

Figure 1.2: Jet in Hot Coflow (JHC) burner schematic

taneously image the temperature, and the distribution and concentration of the two key flame intermediates hydroxyl radical (OH) and formaldehyde (H_2CO). Temperature measurements are achieved using Rayleigh scattering, while OH and H_2CO concentrations are measured using laser-induced fluorescence (LIF).

Although the reaction kinetics of minor species are generally of little importance from the perspective of system efficiency, such intermediate species ranging in concentration from 1% down to the order of parts per billion play a key role in the combustion process, affecting pollutant formation, flame ignition and inhibition of flames [65]. Most of the species of interest are produced and consumed during the reaction process itself, implying that they need to be measured in-situ. Since flames are very sensitive to the disturbances imposed by mechanical probes it is highly advantageous to measure these important species with an (essentially) non-intrusive technique. LIF has been proven to be the most successful technique for identifying concentration of minor species [65].

The aim of simultaneous imaging of OH, H_2CO and temperature is to examine the structure of MILD combustion, under simplified experimental conditions. By examining the effects of varying certain parameters in isolation the fundamental understanding of this unique combustion regime is developed.

This thesis describes the reasoning, results and findings of some of the fundamental aspects of the MILD combustion regime. The proceeding chapter outlines some of the technical background relevant to this study. The elementary principles of combustion are discussed and progress is made through the basic theory behind the techniques which are used in the experiments. Chapter 3 elaborates on the technical details of the experimental setup. Chapters 4, 5, and 6 are dedicated to the presentation of the experimental results and the description of the findings. Chapter 7 ties together the experimental results and discusses the implications of the findings to the understanding of MILD combustion. Chapter 8 finally provides a conclusion to this work.

Chapter 2

Background

2.1 Fundamentals of Combustion

The process of combustion may be vaguely described as a chemical reaction which releases heat. While this definition is very broad, so too is the scope of combustion, and so finding a succinct definition is difficult, if not impossible. As an example, the *Oxford English Dictionary* define combustion as "The development of light and heat accompanying chemical combination" [109]. The area of interest of this project is the study of MILD combustion, which under certain conditions does not involve the emission of light. Thus according to the dictionary definition, the MILD combustion regime should not be termed combustion at all, when most certainly it is. It is these sorts of complications which make a generic definition arduous.

Irrespective of the semantics associated with the word, combustion has for thousands of years played a vital role in the human community. As outlined in Chapter 1, the world has ever-increasing energy demands. It will be combustion that is required to fulfil these requirements until feasible alternatives are found, which is not in the foreseeable future.

It is well known that for combustion to occur, a source of fuel and oxidant must be present, and exposed to a minimum amount of heat. Once the combustion process is started it is self-sustaining, providing these attributes remain present.

Typically the oxidant stream is air, although other substances are capable of fulfilling the same role (such as nitrous oxide, N_2O). For a chemical reaction to occur, the fuel and the oxidant must interact at a molecular level. In addition, for combustion to occur the local temperature must also be sufficiently high. It is the interaction of fluid mechanics and chemical kinetics that dictate whether or not the reaction will be self-sustaining, resulting in an ongoing global reaction. The location where the required conditions are fulfilled, and the combustion occurs is referred to as the *flame front* or *reaction zone*.

Flames generally fall into two categories, either *premixed flames*, or *nonpremixed flames*. The differences between these two types of flames is the way in which the fuel and the oxidant are introduced. In premixed flames the fuel and oxidant are combined prior to combustion. In nonpremixed flames the fuel and the oxidiser are initially separated. In a nonpremixed flame, for a reaction to occur the fuel and oxidant must diffuse into one another, as such, nonpremixed flams are also referred to as *diffusion flames*. This term is not particularly ideal in the sense that diffusion is not the only means by which the fuel and the oxidant mix, and also diffusion occurs in premixed flames as well. As such, the term nonpremixed is used in this document. The classification of a flame as either premixed or nonpremixed is not a binary relationship, and it is possible that a flame may have the attributes of both flames. Such a flame is referred to as partially premixed.

For conventional flames, the reaction efficiency is generally high (that is, the chemical reaction is described as "complete"), but it is often the efficiency of heat utilisation that limits the overall system performance [27]. One technique that is frequently employed to increase the thermal efficiency is that of regeneration or recuperation. Both of these devices aim to recover some of the heat that would otherwise be lost through the exhaust gases. The main difference between the two systems is that a recuperator transfers the heat from a steady flow of flue gases, whereas the regenerator stores the energy into a medium from which the air is later heated [111]. As an example of the benefits of heat recovery, Nishimura et al. [87] claim that in a heavy forge furnace, heat loss through the exhaust can be kept below 5%, compared to 60% when using a conventional burner. Alternatively, it is possible for the exhaust gases to be recirculated internally within the combustor as a means of recovering heat.

2.2 Fluid Mechanics Overview

2.2.1 Introduction to Turbulence

The phenomenon of turbulence is relevant to all aspects of fluid mechanics, of which combustion is a part thereof. The proceeding discussion is in no way meant as a comprehensive explanation of turbulence, but merely provide some background to the aspects relevant to the current study.

Turbulent flows are characteristically unsteady, irregular, random and seemingly chaotic [96]. In contrast, laminar flows are steady and do not vary over time. A turbulent flow could simply be described as one in which the velocity field varies significantly and irregularly in position and time (spatial and temporal). Common examples of turbulent flows are smoke from a chimney, water in a river, flow over vehicles, or simply the wind [96].

Turbulence is the result of instabilities in a flow that are not sufficiently damped by the fluid's viscosity [117]. Two basic conditions lead to the observation as to whether or not a particular condition will be turbulent [96]: Firstly, there must be some form of perturbation. No matter how exacting a particular device is, there will always be the potential for perturbations to form, which may be the result of initial or boundary conditions or material properties, amongst other potential sources. Even if such a perturbation exists, for turbulence to occur, the flow must respond to this perturbation. If the initial fluctuation cannot be suppressed, random velocity fluctuations result, thereby creating the turbulence [111]. At low velocity, the perturbations of the system are essentially "damped out" by the surrounding fluid, and so instabilities do not have the opportunity to form. As the velocity is increased, the system has less time to respond to the perturbations and so manifest themselves on the entire flow, giving rise to the turbulent response of the flow.

It is possible to predict whether or not a flow will be turbulent or not based on its Reynolds number, Re. The Reynolds number relates the inertial and viscous forces, and is defined as;

$$Re = \frac{V \cdot l \cdot \rho}{\mu} = \frac{V \cdot l}{\nu} \tag{2.1}$$

Where;
V is the velocity
l is a characteristic length
ρ is the fluid density
μ is the dynamic viscosity
ν is the kinematic viscosity ($\nu = \mu/\rho$)

While the Reynolds number is only a guide to the turbulence of a flow, for a pipe, generally $Re < 2300$ is considered laminar and $Re > 4000$ turbulent [96]. For Reynolds numbers between these values the flow is considered transitional, and does not exhibit strong laminar or turbulent behaviour.

The motion of turbulent flows is described by eddies, and the flow is said to be comprised of a series of eddies. Each eddy has a characteristic property that essentially exhibits movement as a single unit, while actually consisting of a fluid continuum. An eddy frequently forms a vortex, whereby the eddy rotates. Also, it is common for an eddy to form within another eddy. An important implication of eddies is that they engulf the surrounding fluid causing a transfer of matter, heat and momentum.

2.2.2 Turbulence Length Scales

One key feature of turbulent flows is the production of eddies. The overall flow may be thought of as consisting of a series of such eddies, each having a different size, structure and orientation [26]. The size of an eddy is characterised by length scales. The following four (listed in decreasing magnitude) are most often used;

Characteristic width of flow or macro scale, L; This is the largest length scale within a turbulent flow, and represents an upper bound of eddy size. Generally this quantity is dictated by the physical dimensions of the system rather than the properties of the flow itself [111]. Due to the size of these

eddies, they are of most importance when looking at large-scale mixing.

Integral scale or turbulence macro scale, l_o; This represents the mean size of the large eddies. Obviously this quantity must be smaller than L (as it represented the upper bound), but l_o is of a similar order of magnitude.

Taylor micro scale, l_λ; This scale is related to the mean rate of strain, and is of magnitude between l_o and l_K.

Kolmogorov micro scale, l_K; The Kolmogorov micro scale is the smallest turbulent length scale, and it related to the ratio of viscosity to the rate of dissipation [111].

An issue associated with the various turbulent scales is that of determining the various length scales. Putting a numeric value to these can be very difficult, and is made even more difficult when taking measurements downstream, away from any reference length. The ambiguity associated with defining length scales manifests itself in the literature, with seemingly each study assuming a slightly different definition. Such differences have been noted by [93].

While the length scales within a turbulent flow can be quite small, it is important to note the difference between the mixing scales of flow compared to the diffusion scales. As an example, for air at standard conditions the diffusion scale, as measured by the mean free path (λ), is 6×10^{-8} m, and the mean time between successive collisions is 10^{-10} s [96]. When this is compared to the smallest length scale encountered in flows is generally no smaller than 10^{-4} m, which for flows of 100 m/s gives a minimum time-scale of 10^{-6} s, and even longer for many flows [96]. It is apparent that there are several orders of magnitude difference between the diffusion and flow time scales. The Knudsen number, Kn, relates the length scales of the flow to the dissipation [96];

$$Kn = \frac{\lambda}{l_K}$$

Where;
λ is the mean free path

l_K is the smallest geometric length scale

The Knudsen number is therefore an indicator of the relative effect of the diffusion and flow on the fluid.

2.2.3 Introduction to Jets

A jet may be described as the discharge of fluid from a nozzle. The nature of the nozzle impacts the development of the jet fluid, and so it is important to classify the type of nozzle. Generally a nozzle may be described as either a pipe or smooth contraction. A pipe is the most simple jet, and solely consists of a tube. The smooth contraction is a contoured nozzle, shaped so that the velocity of the flow is essentially constant across the cross-section of the exit. In the present discussion, the term nozzle is used to generalise both a pipe and smooth contraction, however, in some circumstances, the term nozzle is used to describe a smooth contraction.

It is also useful to identify that the cross-sectional shape of a nozzle may be circular, square, or some other shape for that matter. Generally circular nozzles are used due to their symmetry, and are often referred to as axisymmetric jets.

The fluid issuing from a jet mixes with its surroundings as it evolves downstream. When the jet fluid has barely left the exit plane, it is expected to have the same scalar properties as the fluid within the nozzle. This region in which the jet fluid has not yet interacted with the surrounds is known as the potential core. The extent to which this potential core remains is dependent on a number of conditions, however generally for flow issuing from a pipe the potential core is expected to last around five jet diameters downstream from the exit plane, and three jet diameters for the smooth contraction [79].

While the potential core region of a jet is important to note, it is further downstream, where the mixing occurs, that is of more interest. As the jet entrains and mixes with the surrounding fluid the mass flux increases, the jet flow becomes wider, and subsequently its velocity and concentration (proportion of jet fluid) decrease. The rate at which the jet widens is referred to as the spreading rate,

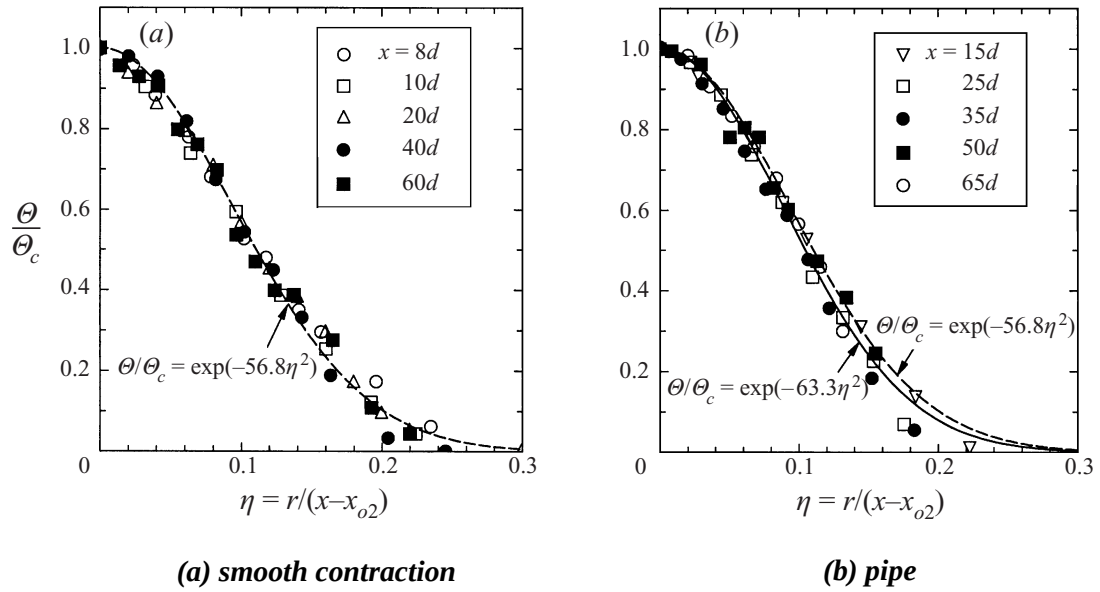

Figure 2.1: Radial profile of normalised scalar mean [79]

and may be expressed mathematically as [96];

$$S = \frac{dr_{1/2}(x)}{dx}$$

Descriptively, the spreading rate is the rate at which the jet half-width increases with downstream distance. The jet half-width is the radius at which the velocity is half the value as at the centreline. Similarly, it is possible to describe the spreading rate based on concentration, or other scalar measurements.

An important observation from the spreading rate is that after the developing region of the jet, the spread is linear and so S becomes a constant. The implication is that the shape of the radial profile remains constant. This may be observed graphically if the radial profile is normalised by the centreline value. The resultant abscissa overlap, as is shown in Figure 2.1 (from Mi et al. [79]) for normalised scalar profiles of both a smooth contraction and pipe.

Due to the similarity of the profiles with downstream distance, this condition is generally referred to as self-similarity. Self-similarity occurs when the mean axial velocity (normalised by the mean centreline velocity) is the same, irrespective of

the x/d [81]. As was the case for the spreading rate, self-similar conditions exist for scalar properties as well as velocity.

2.2.4 Introduction to Mixing

In any combustion system, it is essential that the fuel and oxidant streams are mixed before the chemical reactions can occur. The mixing cannot simply be taken as the macroscopic stirring of the two streams, it must occur on a molecular basis before reactions can occur [62].

The mixing process involved in turbulent flows may be separated into a number of processes [26]. The first is the large-scale engulfing process whereby the large vortices entrain surrounding fluid. Once the fluid streams have been amalgamated on a macro-scale, the smaller scale eddies are able to promote micro-scale mixing, finally resulting in molecular dissipation. Molecular processes are restricted to small spatial scales, while turbulent mechanisms depend on the eddy currents as a result of the fluid mechanics [111].

Mixing in combustion is not only important to ensure the chemical reactions, but also affects the formation of the flame as a whole [51]. Mixing can lead to limits on the energy release rate, and impact soot and pollutant formation [15].

One indicator of the extent of mixing relevant to combustion is scalar dissipation. The quantities of the strain rate and the scalar dissipation are often used interchangeably, and in a numerical study it was found that the two do in fact correlate [55]. Scalar dissipation is a measure of the extent of diffusion between two streams and quantifies the molecular mixing rate. Due to its direct relation to molecular mixing it can therefore be identified as one the most important parameters in the description of combustion [92]. Scalar dissipation, χ, is defined as;

$$\chi = 2\mathcal{D}\left(\nabla\phi \cdot \nabla\phi\right) \tag{2.2}$$

Where;
$\mathcal{D}$ is the diffusivity

$\nabla\phi$ is the gradient of scalar ϕ in the flow

To completely characterise the instantaneous scalar dissipation requires simultaneous measurement of the three spatial components to allow determination of the gradient of the scalar [93]. Due to physical difficulties in obtaining three-dimensional measurements, especially at high spatial resolution, it is often the case that one- or two-dimensional measurements are recorded and the remaining dimensions are either inferred or neglected.

Scalar dissipation is important for the entire combustion process, and particularly for minor species as these tend to be most sensitive to the local scalar dissipation rate [7].

2.2.5 Interaction of Combustion and Turbulence

Turbulent diffusion flames may be considered as being composed of wrinkled, moving, laminar sheets of reaction – or flamelets [117]. Laminar flames in turbulent flows are subjected to strain and develop curvature as consequences of the velocity fluctuations. The extent of the turbulence on the laminar flamelets is indicated by the non-dimensional flame stretch, κ. If the non-dimensional flame stretch is negligibly small, the laminar burning velocity may be considered to be unaffected by the turbulence [117].

The key parameter in the interaction of combustion and turbulence in non-premixed flames is the Damköhler number, Da, which relates the time scales of the chemistry and the flow;

$$Da = \frac{characteristic\ flow\ time}{characteristic\ chemical\ time} = \frac{\tau_{flow}}{\tau_{chem}} \tag{2.3}$$

The Damköhler number therefore describes the time available for the chemistry within the time scales of the flow. When $Da \gg 1$ the chemistry is fast enough to not be influenced by the turbulence. For $Da \lesssim 1$ the turbulence has sufficient opportunity to affect the mixing before the reaction is complete, leading to the reaction zone consisting of partially premixed flamelets [35].

As is the case in defining turbulent length scales, characteristic time scales can be difficult to quantify. To simplify the process, the time scales are often defined as; $\tau_{flow} = l_0/v'_{rms}$ and $\tau_{chem} = \delta_L/S_L$ [111]. The flow time scale is based on l_0, the integral length-scale and v'_{rms} the RMS velocity fluctuations. Although the τ_{chem} described here is used for turbulent flows, it is based on laminar parameters: δ_L is the laminar flame thickness and S_L the laminar flame speed.

A parameter closely related to the extent of turbulence within the flame is the strain rate, which is essentially a velocity gradient. At large strain rates, the fluidic time scales are short in relation to the chemical time scales, and can cause local flamelet extinction [117]. Another important parameter to nonpremixed turbulent flames is the scalar dissipation, χ (introduced previously in §2.2.4) which describes the gradients of scalar quantities. Coupled with the mixture fraction (ξ), the scalar dissipation may be used to examine turbulent flames based on laminar flames with similar stoichiometry and strain rate [13].

The fluidic parameters affect the combustion, similarly the combustion influences the turbulence due to changes in the viscosity and density. In general, in nonpremixed flames the combustion tends to decrease the level of turbulence [35].

2.3 Chemistry Overview

2.3.1 Chemical Kinetics

In order to study combustion, it is essential that the underlying chemical processes are understood [111]. An important aspect of combustion chemistry is to differentiate between global and elementary reactions. On a global scale, combustion involves the reaction of the fuel and an oxidiser to form products. While such a simplistic approach may yield sufficient information in certain applications, for more comprehensive studies, it is necessary to examine the intermediate reactions that take place. These elementary reactions essentially are a series of possible steps which cumulatively form the global reaction.

As an example, the simplified complete combustion of methane in air may be expressed globally as:

$$CH_4+2(O_2+3.76N_2) \rightarrow CO_2+2H_2O + 7.52N_2 \quad (2.4)$$

While the global reaction appears quite straightforward, some 279 elementary reactions and 49 intermediate species have been identified as taking place within the overall reaction [111].

Various parameters affect the extent of each of the reactions and intermediate species, including flow parameters (described by the Damköhler number, equation 2.3) and as may also be expected, the temperature of the reactants also plays a crucial role in the combustion process. Turns [111] gives an overview of the chemical reactions and the effect of temperature on the combustion of methane.

The influence of temperature and flow structure on the chemical reactions is one of the key influences driving the current research. While there has been a great deal of work done on methane combustion, the influence on the reactions under MILD combustion conditions are not as well understood. Nonetheless, some previous studies have been undertaken in somewhat similar conditions. For example, it has long been known that under certain combinations of temperature and pressure that the combustion process is a lot slower, and so the flame temperature is reduced [26]. Such flame conditions are referred to as cool flames, and a different set of intermediate species form, predominately carbon monoxide (CO) and formaldehyde (H_2CO) [26]. While MILD combustion is not strictly under the configuration of a cool flame, it is a considerably lower temperature flame than conventional combustion.

The combustion of hydrocarbon fuels (and in fact fuels in general) consists primarily of the sequential fragmentation of the initial fuel molecule into smaller intermediate species which are ultimately converted to final products, usually dominated by H_2O and CO_2 [116]. In many cases the intermediate species can be fuels themselves [116].

The combustion of simple hydrocarbon fuels may be loosely thought of as comprising a series of oxidation mechanisms at various stages of the overall reaction. For example, Figure 2.2 (reproduced from Westbrook & Dryer [116]) shows the key reaction sub-elements of simple hydrocarbon fuel ($\leq C_3$). If the initial reactants were simply H_2 & O_2, then only the reactions in the lower part of the

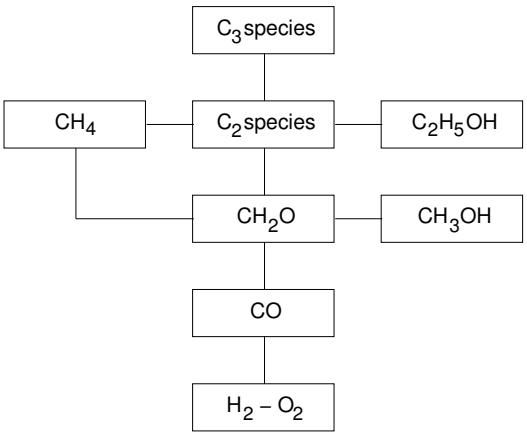

Figure 2.2: Hierarchy of simple hydrocarbon fuels (adapted from Westbrook & Dryer [116])

structure become important. If the initial fuel is of a higher order, then as the fuel is decomposed during the combustion then simpler subsets of reactions become important.

For methane, the general destruction takes place in the following steps [85];

$$CH_4 \xrightarrow[O_2,M]{H,OH,O} CH_3 \xrightarrow[O_2]{O,OH} H_2CO \xrightarrow[M]{H,OH,O} HCO \xrightarrow[O_2,M]{H,OH,O} CO \xrightarrow[O_2]{OH,O} CO_2 \qquad (2.5)$$

Other slightly larger simple hydrocarbons (e.g. C_2H_4 and C_3H_8) follow a similar destruction path, but because the starting molecule is larger, additional intermediates can also be formed (e.g. C_3H_6, C_2H_5, C_2H_3, C_2H_3O, C_2H_2, amongst *many* others). One of the most important intermediates in C_2- and C_3- species is CH_3, which was also seen to be in the destruction path of methane (equation 2.5). Referring to Figure 2.2, another species common to all of the hydrocarbon fuels is H_2CO. Therefore, although various hydrocarbon fuels have different starting points, and so may take a slightly different route, the general process of the destruction into combustion products is similar in each case.

Figure 2.3 (from Refael & Sher [99]) shows the kinetic flow chart for the combustion of propane (C_3H_8) into CO_2. Along the central oxidation path, starting

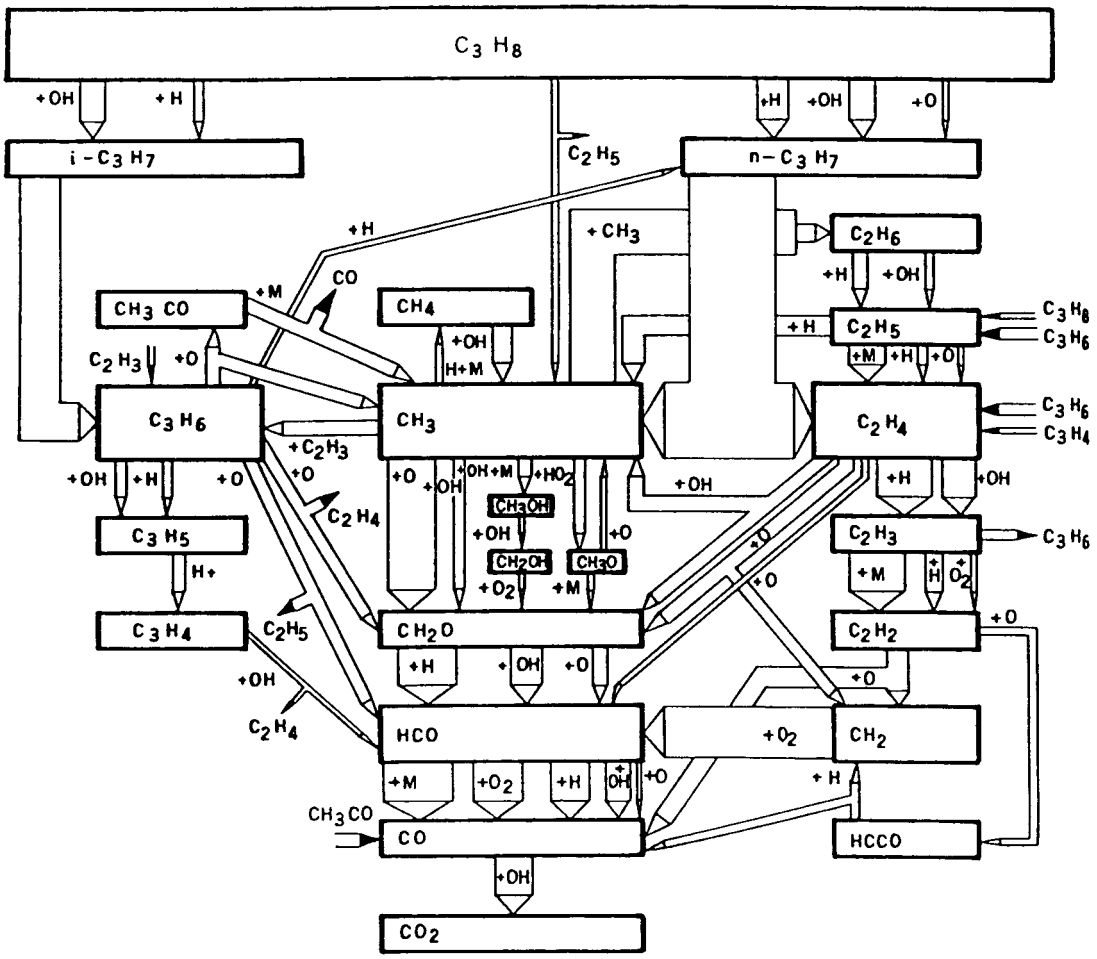

Figure 2.3: Kinetic flow chart of carbon for propane/air flame. Stoichiometric, at: 1600K, P_u=100kPa, T_u=298K [99].

from CH_3, it is seen the general flow of carbon is very similar to that of methane (equation 2.5). Feeding into the C_1-carbon chain are C_2- and C_3-species, starting as either *i*-C_3H_7 or *n*-C_3H_7, which are progressively broken down to yield the C_1-species.

It is easily seen that even simple fuel chemistry gets rather complicated. For higher order hydrocarbon fuels the situation becomes far more complicated. For example, considering standard petrol, and making the gross over-simplification that it consists of just *n*-heptane and *iso*-octane, the reaction involves about 1000 species and 4000 chemical reactions [97].

Since there are many different types of hydrocarbon fuel, with varying degrees of complexity, it is practically impossible for a single study to address every detail. Nevertheless, by noting that the higher order hydrocarbons eventually pass through some of the more simple species, it is possible to build-up information by starting with the simple fuels and then progressing to more complex fuels.

2.3.2 Flame Intermediates

Numerous radicals are of importance to the combustion of even the most simple fuels. For methane (and subsequently higher-order fuels) a selection of the important radicals include; CO, H_2, H, O, OH, HO_2, HCO, CH_3, CH_2, CH, amongst many others. Below are some of the more important measurable intermediates, primarily relevant to CH_4 combustion, although are also of vital importance to other fuels as well.

2.3.2.1 Hydroxyl radical (OH)

The hydroxyl radical (OH) is a primary component of combustion chain chemistry [65]. Referring to Figure 2.2, it is apparent that any hydrocarbon fuel involves H_2–O_2 reactions, of which OH is a major contributor; but the role of OH is far greater than that. Due to its importance, and relatively high concentrations, OH has been probed diagnostically in countless combustion experiments.

Hydrocarbon combustion, in lean to moderately rich conditions is mainly governed by two elementary reactions [44];

$$\mathrm{H + O_2 \rightarrow OH + O} \tag{2.6}$$

$$\mathrm{CO + OH \rightarrow CO_2 + H} \tag{2.7}$$

About 80% of O_2 consumption in stoichiometric hydrocarbon fuels takes place via equation 2.6 [44]. Due to the relatively high activation energy of equation 2.6, flame propagation is sensitive to this reaction. OH production occurs primarily in the mid- to high-temperature range [24].

Contrary to a long held belief [17], Paul & Najm [91] and Brockhinke et al. [16] indicate that imaging of OH does not uniquely identify the flame front. This is a result of OH existing in essentially a quasi-equilibrium state at higher temperatures, and so therefore gives an indication of the flame burning, but not necessarily of the flame chemistry [65]. The measurements of Najm et al. [85] also suggest that the OH mole fraction shows little sensitivity to heat release rates at regions of high unsteady curvature. Similarly, it has been suggested that OH does not change much with imposed strain rate [12]. Nevertheless, OH is still a vital intermediate and extremely useful in diagnostics, giving a good indication of the location of the flame front.

In-depth analysis of the reactions involving OH are beyond the scope of this work, suffice to say that OH plays an important part in hydrocarbon combustion, particularly in the latter stages of fuel consumption.

2.3.2.2 Methyl radical (CH_3)

One of the first steps in the consumption of methane (CH_4) is the formation of methyl (CH_3). CH_3 is a key species in the progress of most hydrocarbon fuels to CO_2, as all carbon flux must pass through it [84]. Conversion of CH_4 to CH_3 may occur through decomposition via [116];

$$CH_4 + M \rightarrow CH_3 + H + M \tag{2.8}$$

$$CH_4 + O_2 \rightarrow CH_3 + HO_2 \tag{2.9}$$

Equation 2.8 is the more dominant of these two [116].

Production of CH_3 from CH_4 may also occur through radical reactions [116];

$$CH_4 + H \rightarrow CH_3 + H_2 \quad (2.10)$$
$$CH_4 + OH \rightarrow CH_3 + H_2O \quad (2.11)$$
$$CH_4 + O \rightarrow CH_3 + OH \quad (2.12)$$
$$CH_4 + HO_2 \rightarrow CH_3 + H_2O_2 \quad (2.13)$$

Following the production of CH_3, it may dissociate (equation 2.14) which is generally limited to very high temperatures, recombine (equation 2.15, plus some other minor recombinations may occur at high temperatures), or react (equations 2.16–2.22, principally equation 2.16 and also equation 2.17, which is very fast and therefore one of the main consumption paths of CH_3 [44]) [116];

$$CH_3 + M \rightarrow CH_2 + H + M \quad (2.14)$$
$$CH_3 + CH_3 \rightarrow C_2H_6 \quad (2.15)$$
$$CH_3 + O_2 \rightarrow CH_3O + O \quad (2.16)$$
$$CH_3 + O \rightarrow H_2CO + H \quad (2.17)$$
$$CH_3 + OH \rightarrow H_2CO + H_2 \quad (2.18)$$
$$CH_3 + OH \rightarrow CH_3O + H \quad (2.19)$$
$$CH_3 + H_2CO \rightarrow CH_4 + HCO \quad (2.20)$$
$$CH_3 + HCO \rightarrow CH_4 + CO \quad (2.21)$$
$$CH_3 + HO_2 \rightarrow CH_3O + OH \quad (2.22)$$

From this set of reactions it is clearly apparent the important role formaldehyde (H_2CO) has. This is further enhanced when it is considered that the methoxy radical (CH_3O) also produce formaldehyde [116];

$$CH_3O + M \rightarrow H_2CO + H + M \quad (2.23)$$

$$CH_3O + O_2 \rightarrow H_2CO + HO_2 \quad (2.24)$$

$$CH_3O + H \rightarrow H_2CO + H_2 \quad (2.25)$$

2.3.2.3 Formaldehyde molecule (H_2CO)

Formaldehyde (H_2CO) may also be designated CH_2O or HCHO. Throughout this manuscript, H_2CO is favoured due to its description of the atomic layout of the molecule.

Formaldehyde is one of the oxygenated hydrocarbons [78], and is an intermediate in the oxidation of most hydrocarbon fuels [116]. In particular, formaldehyde is an important first-step flame intermediate formed in the low temperature regions of combustion of hydrocarbons [14], formed as a product of fuel decomposition in the cool and negative temperature coefficient reaction phases [65]. There are two key combustion chains which involve H_2CO [12]; At low temperatures (<1000K) formaldehyde is produced: CH_3+O_2 → H_2CO+OH, then at higher temperatures it is destructed through H_2CO → HCO → CO.

In laminar flame calculations, Westbrook & Dryer [116] have shown that the concentration of formaldehyde increases rapidly before the region of the flame where the majority of fuel consumption occurs. Experimentally, data suggests that a major chemical source of formaldehyde occurs low in the flame and the rate of formation is reduced at higher flame positions [52]. Both the models and experiments confirm the suggestion that formaldehyde favours the pre-reaction zone region, existing over a wide but comparatively low temperature range, viz., 700–1800K [64]. In particular, for a well-stirred reactor, oxygenated hydrocarbons favour inlet temperatures around 1000K [34].

The presence of O_2 in the fuel allows formation of H_2CO in the fuel consumption regions where its destruction rates are not large, and so higher concentrations can develop [77]. The effect of partial premixing can increase the mole fraction of H_2CO by up to five-fold as compared to the nonpremixed case [78].

Formaldehyde has also been suggested as a marker of the strain rate at the stoichiometric surface, but application is limited due to the substantial thickness of the H_2CO sheet [12]. Supporting the observation of broad H_2CO, imaging has suggested a uniform concentration in the spray vapour in direct-injection (DI) diesel engines [65].

Formaldehyde is a toxic emission resulting from incomplete combustion [64] and a probable human carcinogen, so therefore classified as a hazardous air pollutant if it escapes the combustor [77].

Two main thermal decomposition mechanisms of formaldehyde have been proposed [116];

$$H_2CO + M \rightarrow HCO + H + M \quad then \quad HCO \rightarrow CO + H \tag{2.26}$$

$$H_2CO + M \rightarrow CO + H_2 + M \tag{2.27}$$

Typically, the activation energy of the decomposition reaction is substantially higher than that of reactions with radicals, therefore the decomposition effects will tend to dominate only at high temperature [116].

Formaldehyde consumption by radicals occurs through three main paths, each producing the formyl (HCO) radical [116];

$$H_2CO + OH \rightarrow HCO + H_2O \tag{2.28}$$

$$H_2CO + H \rightarrow HCO + H_2 \tag{2.29}$$

$$H_2CO + O \rightarrow HCO + OH \tag{2.30}$$

In fuel-rich mixtures, equation 2.29 dominates, while if the mixture is lean or stoichiometric, equations 2.28 & 2.30 are more important [116]. The role of OH in the consumption of H_2CO indicates why OH-LIF imaging complements H_2CO-LIF [19], except in the higher temperature flame regions where the H_2CO decomposes.

2.3.2.4 Formyl radical (HCO)

The HCO radical lies in the primary oxidation path for hydrocarbon fuels. In the oxidation of methane, 60–90% of the carbon flow is through the HCO species [85].

HCO has been shown to be an excellent marker for flame burning and heat release rate [65, 85]. HCO, in conjunction with CH, also provides a good test of combustion chemistry [65]. Despite its apparent attractiveness, detection schemes are not sufficiently sensitive to permit single shot imaging, required for turbulent flows [85].

HCO is produced predominately from formaldehyde reactions (§2.3.2.3) and so is directly dependent on the concentration of H_2CO.

Consumption of HCO is via two main paths [116];

$$HCO + M \rightarrow H + CO + M \quad (2.31)$$

$$HCO + O_2 \rightarrow CO + HO_2 \quad (2.32)$$

The first equation relates to thermal decomposition, which will dominate at rich, high temperature conditions, whilst the second dominates in lean, low temperature mixtures [116]. It is also possible that HCO will react with other radicals [116];

$$HCO + OH \rightarrow CO + H_2O \quad (2.33)$$

$$HCO + H \rightarrow CO + H_2 \quad (2.34)$$

$$HCO + O \rightarrow CO + OH \quad (2.35)$$

The primary source of heat in the flame is the production of H_2O and CO_2, not the HCO reactions — but HCO is a good rate-measure of the forward progress of hydrocarbon conversion to H_2O and CO_2 [85].

Direct and accurate measurement of formyl is difficult due to low concentrations and the weak signal it generates by available techniques. As HCO is primarily formed via reactions involving H_2CO [84], an alternative to inferring heat release from HCO is to take the product of the concentration maps of OH and H_2CO to estimate the reaction rate [91].

2.3.2.5 Methylidyne radical (CH)

The CH radical (also known as methylidyne [100])) is often considered a typical marker of the flame front [14]. Donbar et al. [39] claims that CH marks the fuel-rich side of a non-premixed flame (and OH the fuel-lean side). However, CH abundance is typically $1/1000^{\text{th}}$ that of OH, and detection schemes have been difficult to develop and implement [14].

CH is one of the most reactive species [44]. Being short lived, CH disappears early in the vortex/flame interaction, while the evidence from HCO, OH and H_2CO can suggest that the flame continues to burn [84]. It is therefore possible that CH may incorrectly identify breaks in the flame front [91].

2.3.3 Pollutant Emissions

2.3.3.1 Nitrogen oxides (NO_x)

Nitrogen oxides, commonly referred to as NO_x, consist primarily of NO and NO_2. Nitrogen oxides can be ranked one of the most relevant pollutants since they are emitted even with the combustion of "clean gases", because it is formed anywhere nitrogen and oxygen exist together at high temperature [118].

Of the different forms of nitrogen oxides, nitric oxide (NO) is typically the species most of interest in combustion research, since this is the most prevalent form around the combustion region. Away from the combustion zone, the NO can lead to the formation of nitrogen dioxide, NO_2, which results in a brown haze, and can lead to the formation of ozone when interacting with oxygen, O_2. Nitrogen oxides are thus of interest to combustion research due to their adverse health effects and role in atmospheric pollution, including the formation of acid rain and smog

[15]. Additionally, nitrogen oxides interact with the ozone layer, disturbing the equilibrium reaction [15].

Nitric oxide, NO, may be formed by three main mechanisms;

- Thermal (or Zeldovich) mechanism — dominates, especially where high temperatures are present
- Prompt (or Fenimore) mechanism — important in fuel rich environments
- Fuel bound mechanism — results from oxidation of nitrogen containing compounds in the fuel

The rate of formation of NO is highly dependent on temperature, time and stoichiometry [15]. For thermal NO_x formation, the reactants only need to remain at 1600°C for a few seconds and above 2000°C for a few milliseconds [118].

NO_x reduction techniques try to cut peak temperatures, keep the residence time at high temperatures low and avoid high O_2 concentration in these areas [118]. Various configurations have been attempted at reducing high temperature regions, and it has been found that if temperatures can be limited to 1800K thermal NO emissions are kept quite low [26].

While such steps may be taken to limit formation of thermal NO, these tend to be different to those required to reduce prompt NO. To complicate matters, fuel NO abatement strategies generally require an increase in fuel consumption. The task of reducing all three NO formations is therefore very difficult, however due to thermal NO being the major contributor, most strategies aim at limiting the peak temperatures. While modest reductions can be made by reducing the residence time at high temperature, greater reductions may be achieved by reducing temperatures, using techniques including [15];

- Water injection
- Premixed lean burn combustion
- Staged combustion

- Exhaust Gas Recirculation (EGR)

These techniques all aim, in one way or another, to reduce peak flame temperatures. One problem with flame cooling is that the lower temperatures can increase CO emissions [118].

Water injection and premixed lean burn combustion use water and air respectively as a diluent in order to reduce the peak temperature. Lean premixed combustion, where the amount of excess air can be used to control the temperature, has problems with flame stability and issues with flashback [118]. In staged combustion, primary combustion takes place under rich conditions, subsequently followed by a very lean region. Exhaust gas recirculation uses exhaust gases mixed upstream to the fuel and/or air, and may be achieved either internally or externally, thereby reducing peak temperatures. Of these techniques, the first three may be used in gas turbines, while exhaust gas recirculation is generally not used in this application due to the increase in compressor work required (due to the large amount of extra air), however can be used in power plants [15]. Another way to enhance flame cooling is by increasing radiation by means of luminous flames, but can have problems with soot emissions [118].

Another alternative to reduce NO_x emissions is to insert ceramic rods into the flame zone, this has the effect of lowering the peak flame temperature by radiating heat [15]. This has lead to the development of porous burner technologies, whereby the premixed fuel and air flow through a porous media. Studies (e.g. [69]) have shown that insertion of such devices into flames does reduce NO_x, but can also increase the output of CO due to the reduction of temperatures, hence it is important to set a minimum temperature for these types of burners. Therefore, simply inserting objects into a flame in an attempt to reduce peak temperatures and hence NO must be done with extreme care to avoid increases in toxic emissions such as CO [63]. Additionally, the feasibility of this methodology of inserting objects into flames or porous burners is generally restricted to small and medium sized burners.

An alternative theoretical way of reducing NO formation is to use pure O_2 as the oxidiser, but this concept has numerous practical limitations [118].

The techniques mentioned above are designed to limit formation of NO_x. Re-

burning can be used to reduce NO_x after the combustion process [118].

When pollution control was first introduced, it was primarily concerned about reducing emissions of carbon monoxide, hydrocarbons and soot [26]. The steps taken to address these issues tended to increase levels of NO_x, and as such, emission standards of NO_x soon became tightened. This highlights the fact that conventional techniques to reduce emissions of particulate matter, carbon monoxide, sulphur dioxide and hydrocarbons typically lead to an increase in nitrogen oxide emissions [15].

2.3.3.2 Carbon dioxide (CO_2)

Carbon dioxide is a product of combustion of any carboneous fuel. Carbon dioxide is one of the most significant contributors to the greenhouse effect leading to global warming. Reducing CO_2 emissions from combustion systems is therefore vital in ensuring a stable climate and environment. Unfortunately, reducing CO_2 emissions from a given quantity of fuel is virtually impossible. The only way to lower CO_2 emissions is to increase efficiency of the system so that less fuel needs to be burned.

2.3.3.3 Carbon monoxide (CO)

Carbon monoxide is a significant health hazard, as inhalation of even trace quantities have the capability of causing death [26]. Carbon monoxide emissions are often accompanied by hydrocarbon emissions and indicate pockets of gas with insufficient time at high temperature and insufficient oxygen to complete the reactions [15]. As such, the use of water cooling or steam injections proposed to reduce NO_x formation can lower peak flame temperatures but result in increases of CO [88].

2.3.3.4 Soot

Soot is particulate matter of carbon within the flame. These soot particles are heated by the flame and then incandesce (glow due to the high temperature). It

Figure 2.4: Example of soot emission

is this incandescence that gives sooty flames their distinctively yellow colour and also excellent heat radiation. While soot within the flame is an excellent way in which heat radiation can occur, this also can lead to soot being emitted from the flame, which is undesirable. Release of soot from combustors is both unsightly and can also be a health hazard. Figure 2.4 shows an example of soot emission from a combustion source.

Altering the amount of O_2 in the oxidiser can suppress soot formation by partial premixing [102]. In a coflow situation, with lower O_2 in the coflow, more soot is seen toward the flame tip, but overall, the soot volume fraction is known to decrease [3]. More soot is seen at the tip because there is not enough oxidiser to "burn out" the soot. The diluent used to reduce the O_2 level also has an effect. With CO_2 dilution it has been shown that CO_2 reduces soot formation, but not affect soot oxidation [3]. As well as reducing the O_2 level to reduce soot, addition of oxygen to the fuel (by means of partial premixing) can also be used to suppress soot formation by providing enough opportunity to combust the soot [102]. It is also noted that soot levels increase if the temperature of the coflow is increased [3].

2.4 Spectroscopy Overview

2.4.1 Introduction to Spectroscopy

Energy, irrespective of its form, was always thought to exist as a continuum such that it could exhibit any feasible quantity. In 1900, Maxwell Planck proposed that this is not always the case, and that energy can behave discontinuously. Soon after, Einstein applied this concept to light, stating that light also exists in discrete quantities of energy, which later were termed *photons*. Photons may be thought of as discrete particles, each having a certain amount of energy. The respective amount of energy that they possess is characterised by their frequency (ν). The relationship between the two variables is given by;

$$\nu = \frac{E}{h} \tag{2.36}$$

Where;
ν is the frequency (Hz)
E is the energy (J)
h is Planck's constant ($h = 6.626 \times 10^{-34}$ J·s)

The consequence of the theory of energy quanta is that an atom or molecule can exist only at discrete energy levels, and in order to move from one energy state to another would imply that the amount of energy required/released would correspond to the exact difference in energy between the two states. Bohr applied this to his model of the atom, whereby to move from one energy state to another would result in the emission or absorption of a photon possessing the energy equivalent to the energy change.

Combining these theories, it may be seen that an energy change of an atom will be associated with an absorption or emission of light. Since the energy changes are known to be restricted to finite values, then the light associated with this process will also have finite energy, and thus a unique frequency. It is this theory that gives rise to the field of spectroscopy. By examining the wavelengths of light that influence an atom, it is possible to relate this to the energy changes of specific

atoms, and thus determine the atom being investigated. The wavelengths that an atom are receptive to is referred to as a spectrum. These spectra are often shown in graphical form, and represent the relative amount of emission or absorption at each wavelength.

The existence of discrete atomic energy levels has been shown through countless observations. Due to the fact that the energy states of an atom are quantised, each state has a corresponding *quantum number*. Moreover, the theory of quantum numbers for atoms is quite easily extended to include molecules and radicals.

2.4.2 Quantum Numbers

In the preceding section it was introduced that energy is confined to certain states within molecules. Not only are there a set of quantum numbers for a particular species, within this, there are three energy modes; *electronic, vibrational & rotational*. The Born-Oppenheimer approximation permits the total energy to be considered as the superposition of the aforementioned modes, such that;

$$E_{tot}(e, v, J) = E_{elec}(e) + E_{vib}(v) + E_{rot}(J) \tag{2.37}$$

The following sections deal with the three modes of excitation, and the combined effects that they have on each other within a simplified diatomic molecule. While this is a simplified discussion, and a slightly different description is required for atomic and polyatomic situations, the fundamental concepts are similar.

2.4.2.1 Rotational energy

A molecule may rotate about its centre of gravity, along one of its three possible axes of rotation. Each of these rotations potentially has a different moment of inertia, the energy of each rotation however must be quantised. Each rotation has associated with it a quantum number of rotation, the rotational quantum number, J. Being a quantum number, J can only consist of discrete values, viz., $J = 0, 1, 2, ...$

As a consequence of the rotation of the molecule, it will possess angular momentum which will also be quantised. Being a vector quantity, angular momentum has both a magnitude and direction. It may be shown that for a given J value, the magnitude of the angular momentum, ℓ, is fixed and given by $\ell = \sqrt{J(J+1)}$ *amu* (*amu* is defined as the fundamental angular momentum unit, $h/2\pi$, where h is Planck's constant). Further to this, it may also be shown that the possible directions of ℓ possess $2J + 1$ degeneracy. Therefore there are $2J + 1$ possible combinations of angular momentum.

Through the use of the Schrödinger equations, the rotational energy associated with a certain J value is given by;

$$E_{rot}(J) = hcBJ(J+1) \tag{2.38}$$

Where;
h is Planck's constant ($h = 6.626 \times 10^{-34}$ J·s)
c is the speed of light
J is the rotational quantum number
B is rotational constant of the molecule

It is important to note that this assumes that the molecule is rigid, and while this is not the case, at modest temperatures provides a good approximation [41]. A better approximation may be found by adding higher order terms. Although centrifugal distortion terms may be included, these terms have only minor effects [5].

2.4.2.2 Vibrational energy

Bonds within a molecule are not rigid but elastic. This means that a molecule will also possess some energy due to this vibration. As may be expected, this vibrational energy is also quantised and is termed vibrational quantum number, v, with the limitation, $v = 0, 1, 2, ...$

Although the bonds within a molecule are elastic, they do not necessarily behave in a simple harmonic manner. A better representation is achieved through the

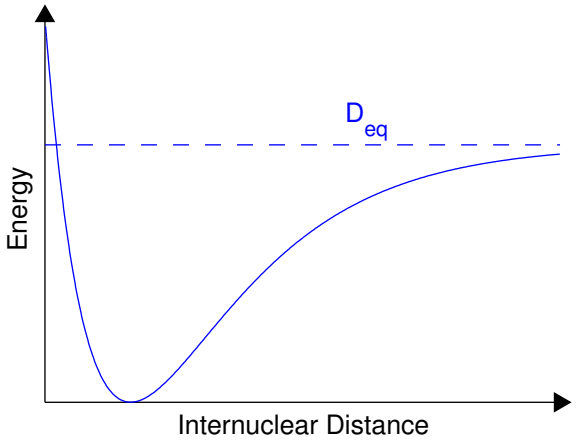

Figure 2.5: Morse curve energy well

Morse Curve. Whilst still an approximation, the Morse curve allows for such features as the dissociation energy (the energy at which the bonds of the molecule are stretched to the point of breaking). The expression for the Morse curve is given by [5];

$$E = D_{eq}\left[1 - \exp\left(a\left(r_{eq} - r\right)\right)\right]^2 \tag{2.39}$$

Where;
E is the energy associated with the system
D_{eq} is the dissociation energy
a is a molecular constant
r_{eq} is the equilibrium bond length
r is the internuclear distance

A plot of the energy well is shown in Figure 2.5.

The horizontal dashed line represents the dissociation energy. It is seen that as the internuclear distance is increased the energy approaches D_{eq}. Eventually the energy will be sufficient to reach D_{eq}, at which point the bond will break and the molecule will dissociate. The point where the energy falls to zero is the equilibrium bond length.

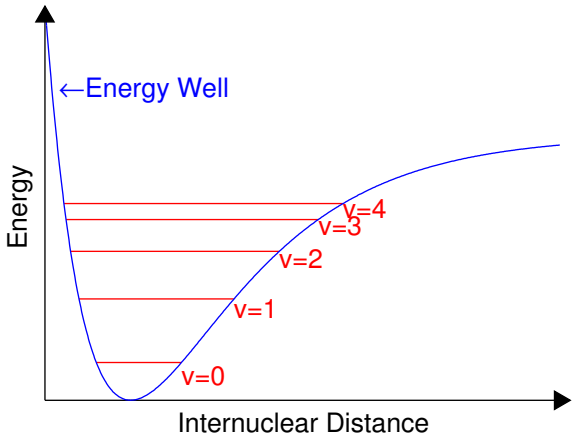

Figure 2.6: Vibrational energy levels

The Morse curve describes the *potential* energy limits associated with a molecule, but does not account for the actual energy levels. This requires the use of the Schrödinger equations. The Morse curve may be used as a basis in the Schrödinger equations to give the energy due to vibration. The subsequent solution is found to have the form [41];

$$E_v = hc\left[\left(v+\frac{1}{2}\right)\omega_e - \left(v+\frac{1}{2}\right)^2 \omega_e x_e\right] \tag{2.40}$$

Where;
h is Planck's constant ($h = 6.626 \times 10^{-34}$ J·s)
c is the speed of light
v is the vibrational quantum number
ω_e is the oscillation frequency
x_e is the corresponding anharmonicity constant

The vibrational energy levels are shown in Figure 2.6. It is also seen that they remain entirely within the energy well.

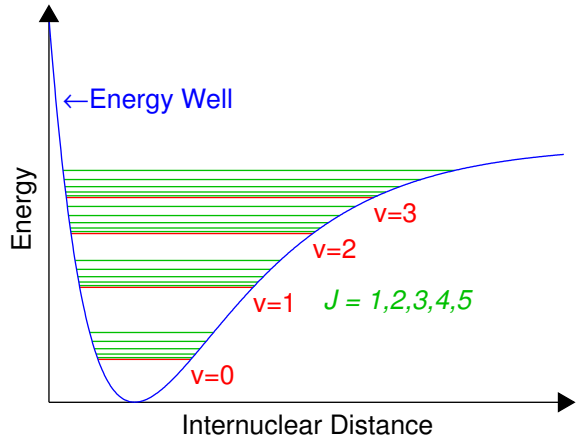

Figure 2.7: Combined effect of rotational and vibrational energy levels

2.4.2.3 Combined effect of vibration and rotational energy

So far it has been identified that the molecule may both rotate and vibrate. As indicated by the Born-Oppenheimer approximation, the total energy of a molecule that is both rotating and vibrating is simply given as the sum of these two effects. The effect of combining the rotational and vibrational energies is seen in Figure 2.7, and is the summation of equations 2.38 & 2.40, superimposed on a Morse curve.

Based on Figure 2.7 it may be seen that the total energy of a molecule is based on both the rotational and vibrational states. Therefore, in order to determine the energy of the molecule, it is necessary to specify both of these energy modes, being v and J (for vibrational and rotational respectively).

It is important to note that Figure 2.7 is only an approximation for a diatomic molecule. A real polyatomic molecule does not follow such a simple analysis, however, the principles presented are representative, and real molecules follow this quite well. Despite these minor deviations, the presented information is provided only to aid the understanding of the fundamental principles.

2.4.2.4 Electronic energy

Each molecule has associated with it a set of orbiting electrons. When the molecule becomes excited its electrons move to a higher energy state. This phenomenon is characterised by the the principle quantum number, n. The principle quantum may be thought of as a guide to the radius of the orbit of the electron. (This is purely from a descriptive aspect. Strictly there are no distinct orbits that the electrons follow, as described by the Heisenberg Uncertainty Principle.) Being a quantum number, n is restricted to a discrete set of values (viz. $n = 0, 1, 2, ...$), with $n = 0$ essentially representing a ground state (although not in a physical sense). The values of $n = 0, 1, 2, ...$ may be respectively represented by $X, A, B, ...$

The orbiting of the electron also implies that it will possess angular momentum, which may be described by the orbital angular momentum quantum number, l, which can assume values ranging from $0, 1, ..., n - 1$. Not only will the electrons orbit the nucleus, they also will spin, with a corresponding spin quantum number, s. Due to the charge of the electrons, in the presence of a field both the orbital angular momentum and to a lesser extent the spin will have preferred orientations, described by the respective quantum numbers m_l & m_s. Owing to the possibility of different orientations, n & l aren't themselves sufficient to uniquely identify a particular configuration. This leads to another quantum number, λ, where: $\lambda \equiv |m_l|$. It is important to note that λ still doesn't take into account whether m_l is positive or negative, and so λ states are said to be doubly degenerate.

The vast majority of situations involve more than one electron. For these situations, a given state may be represented by the total electronic orbital angular momentum quantum number Λ, defined as;

$$\Lambda = \sum_i \lambda_i \rightarrow \sum_i m_{l_i} \tag{2.41}$$

Where i represents each constituent electron.

The various states of Λ are $\Lambda = 0, 1, 2, 3, ...$ with corresponding symbols of $\Sigma, \Pi, \Delta, \Phi, ...$ respectively. Furthermore the spin can be incorporated into the

designation of the electronic designation, as follows; $n^{2S+1}\Lambda$. For example, the electronic ground state of OH is written as $X^2\Pi$; X indicates the electronic ground state, the 2 superscript indicates the multiplicity (since $|S|=1/2$), Π the total electronic orbital angular momentum quantum number, $\Lambda=1$.

Taking into consideration the presence of electrons about the internuclear axis of a diatomic molecule, the moment of inertia is no longer zero, such that [41];

$$E_{rot}(J,\Lambda) = hcBJ(J+1) - B\Lambda^2 \tag{2.42}$$

For $\Lambda \neq 0$ a degeneracy referred to as Λ-doubling occurs.

The spin associated with the electrons can couple with the rotational motion. Hund's case (a) and (b) describe the extreme cases of the rotational coupling. Further description of Hund's case are described in detail elsewhere (e.g. Eckbreth [41]).

2.4.2.5 Combined effect of rotational, vibrational and electronic energy

The combined effect of the rotational, vibrational, and electronic energy may be considered by the Born-Oppenheimer approximation, which states that each of the energy states are completely independent on one another. The total energy of a molecule may then be expressed as;

$$E_{total} = E_{electronic} + E_{vibrational} + E_{rotational}$$

It is important to note the approximate order of magnitude of each of the energy types: electronic energy is about 1000 times that of vibrational energy, which is itself 1000 times the rotational energy. The structure of the various energy states is seen in Figure 2.8.

Much like in §2.4.2.3, where the combined effects of rotational and vibrational energy were considered, it is now necessary to also include the electronic energy. With the rotational and vibrational states, the energy always remained within

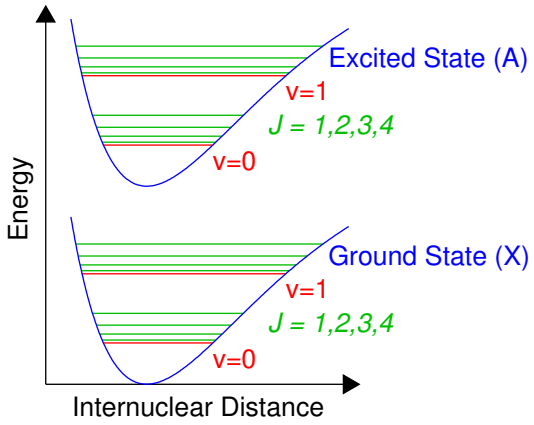

Figure 2.8: Combined effect of rotational, vibrational and electronic energy

a single energy well. Electronic energy states result from the excitation of an electron (not just its mode of motion). As such, each electronic energy state will have its own energy-well associated with it. This is represented in Figure 2.8, whereby there exists two distinct energy wells for each electronic energy level.

As was the case with other plots indicating energy levels, Figure 2.8 is indicative only, and in no way is meant to provide an accurate description of an actual molecule. Again, no effort has been made to accurately reflect actual energy proportions.

When a molecule is in its excited state, its properties are written with a prime ($'$), e.g. J', and in the ground state a double prime ($''$) is used, e.g. J'' (similarly for the vibrational quantum number, v' and v'').

2.4.3 Boltzmann Populations

In the preceding section, different energy modes have been identified, and that for each energy mode is a corresponding quantum number. The designation of a single quantum number defining each of the energy states can only be made for a single molecule. Within a gas, there are many many molecules, and each does not necessarily have the same energy levels. It is possible to determine the fraction of the population existing in state i (denoted f_i) by the Boltzmann distribution;

$$f_i = \frac{g_i \cdot exp\,(-E_i/kT)}{q} \tag{2.43}$$

Where;
g_i is the degeneracy of state i
E_i is the energy of state i
k is Boltzmann's constant
T is the (absolute) temperature
q is the partition function, and is generally found by knowing that the total sum of all the population fractions must sum to unity, such that;

$$q = \sum_i g_i \cdot exp\,(-E_i/kT) \tag{2.44}$$

2.4.3.1 Diatomic rotational Boltzmann populations

For the simplified diatomic rotational energy expression presented in §2.4.2.1 it is possible to derive some useful mathematical functions expressions for rotational Boltzmann distribution calculations. Combining equation 2.43 and the relationships for diatomic molecules from §2.4.2.1, viz. $g = 2J+1$ and $E = hcBJ(J+1)$, the Boltzmann distribution may be written as;

$$f_{rot} = \frac{(2J+1) \cdot exp(-hcBJ(J+1)/(kT))}{q_{rot}} \tag{2.45}$$

Where the partition function may be written as;

$$q_{rot} = \sum_{J=0}^{\infty} \left[(2J+1) \cdot exp\left(\frac{-hcBJ(J+1)}{kT} \right) \right] \tag{2.46}$$

Which may be solved to yield;

$$q_{rot} = \frac{kT}{hcB} \tag{2.47}$$

Therefore the rotational Boltzmann fraction (for a simplified diatomic molecule)

may be shown to be;

$$f_{rot} = \frac{hcB}{kT} \cdot (2J+1) \cdot \exp\left[\frac{-hcBJ(J+1)}{kT}\right] \tag{2.48}$$

The maximum population will occur when this function is at a maximum. In order to find the maximum of a function, it is differentiated and equated to zero. Doing this it is found that the J value which yields the peak population is;

$$J_{max} = \sqrt{\frac{kT}{2hcB}} - \frac{1}{2} \tag{2.49}$$

Clearly, the peak population is temperature dependent. Frequently, the temperature throughout a measurement area varies, and so it is important to make allowances for this. One way which this may be done is by selecting a J value which is least dependent on temperature. This is achieved in a similar way to finding the peak J value, however, this time differentiating with respect to the temperature to find the J value that is least sensitive to temperature. The result of this leads to;

$$J^{*^2} + J^* - \left(\frac{k}{hcB}\right) T = 0 \tag{2.50}$$

Where;
J^* is the value of J which is least sensitive to temperature
T is the evaluation temperature (often taken to be the average)
k, h, c, B previously defined in this section

It is generally the case that J^* is the value which is the unknown, and so equation 2.50 may be rearranged to give;

$$J^* = \frac{-1 \pm \sqrt{1 + \frac{4k\bar{T}}{hcB}}}{2} \tag{2.51}$$

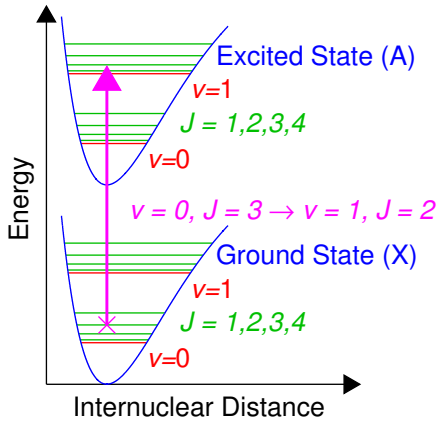

Figure 2.9: Electronic excitation process

2.4.4 Energy Transitions

It has been shown that the energy of a molecule may be described by its rotational, vibrational and electronic energy levels, with the total energy given by the sum of these energies. With changes in environment, the energy of the molecule will change, and so the energy states of the molecule will also change. Such an energy change is shown in Figure 2.9.

In Figure 2.9 an arbitrary transition is represented from the ground state, with $v'' = 0$ and $J'' = 3$ to the first electronically excited state with $v' = 1$ and $J' = 2$. Associated with each of these transitions is a unique energy difference, which will absorb or emit a photon of light with the exact energy of the transition. It is based on the wavelength (energy) of the absorption and emission of light that spectroscopy is based, and enables a certain transition of a particular species to be identified.

Notationally, the electronic transition is denoted with the corresponding upper-case letter (as outlined in §2.4.2.4), and following a hyphen, the lower electronic state. The vibrational transition is generally written in brackets, with the first number indicating the excited state and the second the ground-state vibrational level, with the two separated with a comma. The change in rotational quantum number associated with a transition, i.e. $\Delta J = -2, -1, 0, 1, 2$ is denoted as; O, P, Q, R, S. The ground-state rotational number follows the ΔJ and is included

in brackets (enabling the excited state rotational quantum number to easily be deduced). Following the example presented in Figure 2.9 the transition would be denoted $A - X(1,0)P(3)$.

2.4.5 Collision Processes

The energy transfer process described in the preceding section does not solely involve the absorption or emission of light. Collisions with other molecules can cause changes in the energy level of the species, and so the absorption and emission wavelengths will be different. The energy transfer resulting from a collision can be classified depending on its effect; Rotational Energy Transfer (RET) results in a change in the rotational quantum number, Vibrational Energy Transfer (VET) changes the vibrational quantum number, and electronic transfer changes the electronic state of the species. Quenching is a specific form of electronic transfer, where the species is returned to its electronic ground state without light emission. Erroneously, quenching is sometimes used to describe collision processes in general, but this is not strictly correct.

The complexity introduced by collision processes is the cause for the difficulty associated with obtaining quantitative LIF measurements, and is compounded by the fact that these processes are temperature dependent.

2.5 Laser Diagnostic Techniques

Outlined in this section is a brief description of a selection of the main laser diagnostic techniques applicable to reacting flows.

2.5.1 Mie Scattering

Mie scattering is probably the most elementary laser diagnostic technique, and simply involves the reflection of laser light from particles in a flow. These particles can either be deliberately seeded (for flow visualisation purposes), or naturally occurring. Mie scattering is referred to as an elastic process, implying that the

incoming and outgoing light is of the same frequency. The light that is scattered is readily captured on a camera, and the stronger the intensity of the signal the greater the concentration of particles. The great advantage of Mie scattering is that the resultant signal has intensities several orders of magnitude higher than any other technique.

For many laser diagnostic techniques involving flows with even slight particulate levels, Mie scattering can be a considered a hindrance as it potentially interferes with the recorded signal of other techniques. This interference can pose a considerable problem due to its strong intensity relative to other techniques. In cases where Mie scattering is undesirable, it is often necessary to take measures to avoid the occurrence of particulates, either by filtering the fluids, and in reacting flows by using fuel substitution to avoid generation of soot.

2.5.2 Rayleigh Scattering

Rayleigh scattering is the elastic scattering of light from molecules (as distinct from particles in Mie scattering). Due to the generic scattering nature of this technique it cannot be used for individual species concentration measurements. In fact, the extent of the scattering is dependent on the Rayleigh cross-section, which *is* different for each species, and so it is necessary to determine composition by some other means.

The Rayleigh cross-section is essentially a measure of the amount of light a particular species will scatter. The Rayleigh cross-section of species i (σ_i) for detection at 90° to the incident light (and assuming no de-polarisation) is given by [74];

$$\sigma_i = \frac{4\pi^2 \left(\eta_i - 1\right)^2}{\lambda^4 N_0^2} \tag{2.52}$$

Where;
σ_i is the Rayleigh cross-section of species i ($\mathrm{cm}^2/\mathrm{sr}$)
η_i is the refractive index of species i (–)
λ is the laser wavelength (cm)
N_0 is the Loschmidt number (2.687×10^{19} cm^{-3})

For a gas mixture, the cumulative Rayleigh cross-section is simply;

$$\sigma_{eff} = \sum_i X_i \sigma_i \tag{2.53}$$

Where;
σ_{eff} is the effective Rayleigh cross-section of the gas mixture
σ_i is the Rayleigh cross-section for species i
X_i is the mole fraction of species i

The Rayleigh scattering intensity is then given by;

$$I_R = K \cdot I_{incident} \cdot \sigma_{eff} \cdot N \tag{2.54}$$

Where;
I_R is the intensity of the scattered Rayleigh light
K is a constant which accounts for the geometry of the measurement system
$I_{incident}$ is the intensity of the incident light
σ_{eff} is the effective Rayleigh cross-section of the gas mixture
N is the total number density of the gas mixture

After taking into account the geometry constant and the variations in incident laser intensity, the Rayleigh signal depends on both the total number density and the Rayleigh cross-section of the composition. In reacting flows, the differences in temperature exclude the possibility of holding the number density constant so the Rayleigh cross-section must either be constant across the measurement volume or somehow accounted for. From this, it is then possible to find the total number density, which yields information about both the temperature and density.

2.5.3 Raman Scattering

Raman scattering is a very similar process to Rayleigh scattering, however, Raman scattering is inelastic, implying that the scattered light is frequency shifted from the incident wavelength. In fact, Rayleigh scattering is a subset of the Raman scatter, but without the frequency shift. Raman scattering can be frequency shifted to either longer wavelengths (Stokes Raman) or to shorter wavelengths (Anti-Stokes Raman). Raman scattering is a weak process, and so to obtain reasonable signal, high laser fluences are required, this generally limits the Raman technique to point or line measurements, although two-dimensional planar images are possible.

The weak nature of Raman scattering, coupled with the high laser fluences required, results in Raman signal being prone to interferences from potentially numerous sources:

- Mie and Rayleigh scatter
- Raman scattering from other species (also known as Raman cross-talk)
- LIF of other species
- Non-resonant fluorescence from polycyclic aromatic hydrocarbons (PAHs) and soot precursors
- Soot induced interferences
- Chemiluminescence
- Laser induced gas breakdown through the measurement volume

Some of these interferences may be eliminated through the use of a variety of techniques, while others are inherent and cannot be eliminated, depending on the nature of the flame and excitation/detection equipment.

Species identification can be obtained by analysing the recorded spectrum and identifying the location of peaks at differing wavelengths after passing the signal through a spectrograph. In a spectrograph the incoming light is separated into its

constituent wavelengths (spectrum), and based on the intensity of light emitted at a particular wavelength it is possible to determine the species which produced that wavelength, depending on the wavelength of the incident laser.

2.5.4 Laser Induced Fluorescence (LIF)

Laser induced fluorescence is the spontaneous emission of light from an upper energy level (which has been excited using laser light) to a lower energy level. Due to the energy level selectivity (and subsequently wavelength dependence) particular species may be identified. LIF has the advantage of being non-intrusive, flexible, high selectivity, high sensitivity, high spatial resolution, two dimensional, time resolved and single pulse measurements [65]. The ability to select individual species with high accuracy has lead to LIF seeing widespread application throughout combustion research for minor species detection.

Lasers are by far the most convenient way to provide spatially and spectrally selective excitation to facilitate the fluorescence. Most LIF measurements are made using a pulsed laser – the increased intensity during a short period ($\sim$10ns) usually eliminates the majority of the background chemiluminescent emission from the flame [65]. However, because of the low repetition rates generally associated with high power pulsed laser systems, temporal evolution of turbulent flames is generally not possible.

For diagnostic purposes, often the shifted fluorescence is recorded to avoid interferences from spuriously scattered laser light or Mie scatter. LIF possesses the ability to detect flame radicals and species at the ppm or even sub-ppm level. LIF has a much larger cross-section than some other techniques (e.g. Raman) but is not as strong as others (e.g. Mie).

There are several basic criteria which must be satisfied to perform fluorescence measurements [26];

- The species must have a known emission spectrum
- The molecule must have an absorption wavelength which is accessible by the laser source

- For quantitative measurements, the rate of radiative decay of the excited state must be known
- Relaxation effects must be considered

It is the requirement to correct the measured fluorescence for collisional quenching that is most troublesome in obtaining quantitative measurements by LIF. There are only a limited number of species that have well known quenching processes, for other species a lack of knowledge on the collisional quenching effects makes quantitative measurements virtually impossible [65].

2.5.5 Molecular Energy Transfer

As was indicated in §2.5.4, to obtain accurate and quantitative LIF results, issues surrounding the energy transfers among the various energy states of the species must be considered. These collisional processes were described in §2.4.5, and although not strictly technically correct, these energy transfers are commonly grouped under the title of quenching.

Some of the most commonly studied species, namely NO and OH, coincidentally have high collisional cross-sections. If the pressure, temperature and concentration of main species are accurately known, quenching of NO and OH may be predicted to levels of ±30% [65]. To make such corrections involves knowing the partial pressures of all species present other than the one of interest, as well as the rates for deactivation of the excited state of the species by all others present and the dependence of these rate constants on temperature be known [41]. There are only a limited number of species to which the required parameters are known, restricting the ability to obtain quantitative measurements to those species.

While it is possible to account for quenching effects for commonly studied species, this can still be very difficult, and it is preferable if such effects can be minimised. As an indication of the prevalence of quenching, at one bar pressure the quenching rate is typically 2–4 times that of spontaneous emission [65].

One way in which it is possible to minimise the effects of rotational energy transfer and rotational level dependent quantum yields is by using a temporarily narrow

detector gate, instead of capturing the entire fluorescence decay [101]. However, this technique can only feasibly be applied to low pressure cases. A variation on this technique is to use short-pulse spectroscopy, whereby the excitation time is less than that required for collisions. By not offering sufficient time to allow quenching to influence the emission, quenching effects may nearly be avoided [65]. A "short pulse" is defined as a pulse with a temporal width significantly shorter than the excited state lifetime, and is generally in the order of pico- or femto-seconds, requiring specialised short pulsed lasers.

A solution to minimising the effects of collisions and quenching is through the use of laser induced predissociative fluorescence, LIPF. Predissociation occurs when the spectral structure of the transitions collapses, and appears as a continuum, while it is in fact actually below the dissociation limit. Further details on predissociation may be found in the literature, e.g. Banwell [5]. The compromise of this technique is that the states used exist in lower populations, and so result in less yield. Also, the high laser powers required can de-populate the ground-state levels [65]. However, LIPF has been shown to be a viable technique and has been used to measure OH [94].

Of the various approaches to circumvent correcting for quenching issues, saturation has received significant attention. In saturated fluorescence, the incident laser intensity is made sufficiently large so that the absorption and stimulated emission rates are much greater than the collisional quenching rate so that it becomes unimportant. The other advantage of working in the saturated regime is that the fluorescence signal is maximised, providing the highest species detection sensitivity. Saturated fluorescence is not without its complications however. High intensity tuneable lasers are required to achieve saturation, but are difficult to achieve at certain wavelengths. Nonetheless, with careful attention to view only saturated signals it has been demonstrated that saturated fluorescence measurements of OH could be performed to within 20% of number density derived independently from absorption, and has also been applied successfully to measurements of NO in flames [65].

For linear LIF measurements, the amount of fluorescence is a function of the amount of incident laser energy. The greater the incoming laser energy, the greater the fluorescence. For moderate laser energies, the relationship between

laser power and LIF signal is linear. However, as is the case with most physical systems, this linear regime has a finite limit, beyond which, for an increase in input, the fluorescence signal no longer increases. This loss of linearity is termed saturation, and is shown schematically in Figure 2.10.

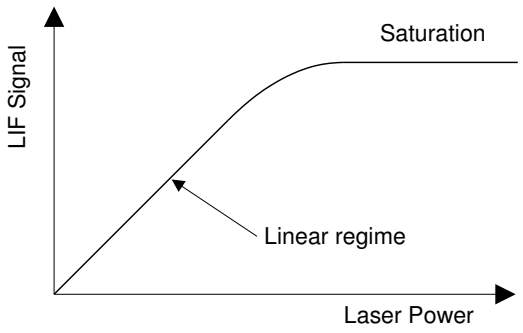

Figure 2.10: LIF saturation example

Although saturation can be useful for avoiding quenching effects, obtaining reliably accurate results is still an arduous task, further complicated by the strong effects of energy transfer in the ground state [65].

The main alternative to saturation to account for quenching effects is to measure the fluorescence lifetimes. This has the advantage of being able to perform corrections for a variety of species. Based on available techniques, fluorescence lifetime techniques are limited to point measurements, and can only be applied to averaged results [65].

While techniques have been identified to deal with the effects of collisional energy transfer, other pathways of energy loss exist [41];

- dissociation
- ionisation
- energy transfer to another molecule
- energy transfer within the same molecule
- chemical reaction

Generally however, the collisional losses dominate and so attention is drawn to these.

2.6 Laser Imaging of Key Scalars

2.6.1 Hydroxyl Radical (OH)

The hydroxyl radical, generally referred to simply as OH, is one of the most frequently studied flame intermediates. The reason for the interest in OH is that it is a primary component in most combustion chemistry, occurs in high levels, and is relatively easily detected [14]. Detection of OH is primarily achieved by the use of LIF [65] and may be accomplished through a variety of different excitation schemes, depending on the circumstances.

A popular method for obtaining LIF of OH is through the use of a KrF laser at 248nm ($A - X(3,0)$), and while often lacking quantitative data, this is not of importance in many circumstances [65]. The $A - X(0,0)$ band at ∼308nm is also used often due to its strong transitions. For the present study, a KrF laser is not available and while the $A-X(0,0)$ band has strong transitions, separating these from the laser scatter (of the same wavelength) gives rise to complications. Also, $A - X(0,0)$ excitation suffers as much as 20% absorption through a flame [10]. Instead of using either of these common schemes, alternative schemes will be investigated that are available.

Absorption issues related to the $A - X(0,0)$ excitation scheme may be reduced by a factor of three by using $A-X(1,0)$ band instead [101]. Several studies have used the $A-X(1,0)$ band for exciting OH, covering a wide range of wavelengths from ∼281 to 288nm. For example, Bengtsson [9] excited the R-band transitions of $A-X(1,0)$ around 281.5nm (and detection of $(0,0)$ at ∼310nm), the frequency doubled component of the 563nm he used to simultaneously examine C_2. Barlow et al. [8] also used the $A - X(1,0)$ excitation, but of an O-line at 287.9nm and detected both $(0,0)$ and $(1,1)$ fluorescence. Other $A - X(1,0)$ excitations have been reported, using a Q-line at ∼283nm [11, 91].

Using a Nd:YAG pumped dye laser for excitation of OH $A-X(1,0)$ around 287nm

offers the possibility of simultaneously exciting NO as well [115]. To generate the 226nm required for NO using such a laser system, a wavelength of 287nm is first generated (by frequency doubling the output of the dye laser), and mixed with the fundamental Nd:YAG 1064nm to produce the 226nm. Since during the doubling process there is a portion of 287nm that is not converted to 226nm, the residual 287nm beam may be used for OH excitation while simultaneously using the mixed 226nm for NO. Furthermore, the 226nm can also be used for excitation of atomic oxygen, O.

One problem with using $A-X(1,0)$ over $A-X(0,0)$ is that the $(0,0)$ and $(1,1)$ fluorescence from the $A-X(1,0)$ band overlaps [101]. This overlapping does not permit either to be uniquely identified, which in some circumstances may pose a problem. Also, the relationship between vibrational relaxation and quenching varies with collision partner for the schemes with different vibrational levels, implying that these effects will change throughout the flame, making corrections more difficult [101].

While not unique to any particular excitation scheme, OH has a high collisional cross-section, implying that this effect must be taken into consideration in any OH-LIF measurement – whether quantitative or qualitative, even though consideration for quenching has been neglected in many previous studies. One means of calibrating LIF signal is to use a calibrated signal from a known reference flame [23];

$$n = n_{cal}\left[\frac{I}{I_{cal}} \cdot \frac{f_{cal}}{f} \cdot \frac{E_{L,cal}}{E_L} \cdot \frac{Q}{Q_{cal}} \cdot \frac{g(\nu_0)_{cal}}{g(\nu_0)}\right] \tag{2.55}$$

Where;
n is the number density
I is the fluorescence signal
f is the Boltzmann fraction
E_L is the laser energy
Q is the quenching rate
$g(\nu_0)$ is the spectral overlap term

The *cal* subscript refers to the respective values in the calibration flame.

Comparing the ratios of the variables in equation 2.55 rather than absolute values simplifies the quantification process. Since OH exists over a relatively narrow range of conditions, corrections for Boltzmann fraction and collisional quenching are somewhat less important than for some other species, for example NO [6], but still important nonetheless.

2.6.2 Formaldehyde (H_2CO)

Formaldehyde (H_2CO) is an important intermediate in hydrocarbon oxidation in the cool region before the flame front [65]. Unlike many polyatomic molecules, the rotational structure of formaldehyde allows individual transitions to be accessed using a conventional pulsed dye laser [52]. Being a polyatomic molecule, the populations of formaldehyde are spread over a large number of rotational and vibrational levels, leading to lower signal intensity for the same concentration [65].

A major problem that plagues LIF measurements of polyatomic species is the complex temperature dependence of the Boltzmann fraction and collisional cross-section data [91, 103], and for formaldehyde these dependencies are compounded by large variations [64]. The quenching corrections of formaldehyde are not well known, leading to estimations, for example a simple $1/\sqrt{T}$ correction [52]. More recent work has facilitated quantitative results by using a calibration from a reference cell of formaldehyde at low pressure [103]. An alternative method is to use a combination of LIF and cavity ring-down (CRD) spectroscopy (e.g. [68]).

Predissociation is problematic in formaldehyde measurements below 320nm [64], and so the strongest $A - X$ 4_0^1 band (352-357nm) has been one of the most commonly used. Within this band, weak excitation may be achieved from a frequency tripled Nd:YAG laser at 355nm. The use of 355nm from a Nd:YAG leads to CH_4 Raman and polycyclic aromatic hydrocarbons (PAH) fluorescence contaminating the formaldehyde signal [52]. While excitation around 355nm is potentially subject to contamination from PAH, other aldehydes & ketones or OH, O_2 and NO are not likely to affect the formaldehyde LIF signal [19]. The background PAH fluorescence from excitation around 355nm has been shown to be insensitive to excitation wavelength in the region interest [52], and so there is

little advantage in using a dye laser over an Nd:YAG to improve signal quality. Nevertheless, Bombach & Käppeli [14] is an example of work where formaldehyde was excited using a dye laser (at 352.97nm), simultaneously with CN and CH. Due to excitation in this band, temperature differences would have significantly influenced the results, and since temperature was not recorded, these variations could not be corrected for. While acknowledging this fact, it is still possible to gain useful information from such an excitation scheme.

The potential for simultaneous excitation of formaldehyde and diatomic hydrides may appear to have advantages, this also highlights some complications that may arise. Due to the broad formaldehyde excitation and emission, this tends to overlap with the finer structure of the smaller species, and so uniquely identifying a particular species without contamination is difficult [63]. Similarly, when exciting formaldehyde the presence of other species can potentially appear in the formaldehyde signal.

Despite the apparent attractiveness of excitation at 355nm, the issues associated with the variation of partition function with temperature suggest that weaker transitions may have advantages, as these may be less dependent on temperature. Such an alternative has been identified by Klein-Douwel et al. [63], who excited at 370nm instead (albeit at a lower efficiency) in the $A - X\ 4_1^0$ band, covering the range 368 to 373nm [69]. Despite moving to a less temperature dependent band, the Boltzmann distribution still varies by a factor of two over the range 800–1500K [65]. While less temperature dependent, as a compromise, the populations are much lower in the 4_1^0 than the 4_0^1 by a factor of 10 at 700K and 2.5 at 1800K [69]. Conveniently, the $A-X\ 4_1^0$ band of formaldehyde has an overlapping spectral range with the $B - X(1, 0)$ band of CH [64].

Luque et al. [69] found that interferences on formaldehyde measurements are more prevalent in nonpremixed than in premixed flames, this was attributed to the presence of formaldehyde hot bands and PAHs in the nonpremixed flame. An important difference between the two types of flames used in the Luque et al. [69] study was that the premixed flame was at low pressure, which although not specifically identified, could also be a factor which contributed to the lack of interferences.

It has been concluded that dye laser excitation has problems associated with low

pulse energy and Nd:YAG excitation has problems arising from a low excitation efficiency [19]. Of the two excitation schemes presented so far, $A - X\ 4_0^1$ near 355nm suffers from interference problems and temperature dependencies, and the alternative $A - X\ 4_1^0$ is weaker and still subject to severe temperature effects. While the temperature effects and weaker signal plague the $A - X\ 4_1^0$ band, Klein-Douwel et al. [63] recommends this because it less effected by the background interference, which presents a difficult problem to otherwise solve.

An alternative to the techniques already mentioned, proposed by Burkert et al. [19], is to use an XeF excimer laser, capable of producing high power in the UV range. Another advantage of the use of an excimer laser for formaldehyde measurements is that its fast tuning capabilities permit wavelength switching at a sufficient rate to allow separation of the formaldehyde LIF from the total signal, including PAH and other non-formaldehyde sources [19].

A different excitation scheme was proposed by Paul & Najm [91], who used the $A - X\ 2_0^1 4_0^1$ band near ∼338nm, citing an improvement in signal of over ten-fold over the $A - X\ 4_0^1$ which itself is stronger than $A - X\ 4_1^0$. The excitation of the $A - X\ 2_0^1 4_0^1$ band has been subsequently in other studies [103]. Unlike the large off-wavelength background signals observed when using excitation around 355nm, Paul & Najm [91] claim backgrounds less than 2% of the peak formaldehyde signals, tending to indicate great advantages in 338nm excitation. Nonetheless, excitation around 338nm still has problems with this band being dissociative [103]. The impact of the predissociation rate is however reduced by the change in quenching rates [91].

For the case of excitation of the $A - X\ 2_0^1 4_0^1$ band, interferences from Raman signal of CH_4, N_2, and O_2 occurs between 360 & 370nm, allowing fluorescence of formaldehyde to be recorded in the range 380 to 500nm to be free from the mentioned forms of stray light [103]. The conclusion is then drawn that of the various excitation schemes that have been presented the $A - X\ 2_0^1 4_0^1$ band near ∼338nm appears to be the most advantageous.

2.6.3 Temperature Measurements

Temperature is one of the key quantities in combustion research, where it governs the overall efficiency of the combustion process. Furthermore, most of the chemical reactions in the flame which are responsible for the heat release or the formation of pollutants are strongly dependent on temperature [65]. Accurate knowledge of the temperature and information on the fluctuations and the distribution of the temperature are of utmost interest in any combustion study.

As highlighted by Dibble & Hollenbach [36], inadequacies of thermocouples lead to the development of temperature measurements by alternative means, predominately laser based techniques. While there are several options available to measure temperature using laser diagnostic techniques (e.g. cavity ring-down (CRD) spectroscopy or LIF thermometry) the most appropriate and simplest for two-dimensional temperature maps is to use the Rayleigh scatter method.

From a practical viewpoint, Rayleigh diagnostics suffer from Mie scattering interferences. Since Mie cross-sections are ten to twenty orders of magnitude stronger than Rayleigh, the measurement environment must be virtually free of particulates. Unlike some other methods, the elastic nature of Rayleigh scatter means that the signal to be recorded is the same wavelength as the laser used, as is the case for Mie scatter, and so filtering is unable to separate the two signals. The technique is thus restricted to very clean situations, and filtering of all gases is absolutely necessary. Despite these limitations, Rayleigh scattering is of interest since its cross-sections are orders of magnitude stronger than most other techniques.

In §2.5.2 it was outlined how the Rayleigh signal gives a measure of the total number density. From this it is possible to determine the temperature (or alternatively density) through the use of the ideal gas law, which for constant pressure leads to;

$$N \propto \frac{1}{T}$$

Referring back to equation 2.54;

$$I_R = K \cdot I_{incident} \cdot \sigma_{eff} \cdot N \tag{2.54}$$

It is therefore apparent that;

$$I_R \propto \frac{1}{T}$$

From an experimental perspective, determination of the constant in equation 2.54 can be difficult. A better alternative, if the other parameters are held constant, is to calibrate the Rayleigh scatter against the signal at a known reference condition [86];

$$\frac{I_R}{I_{R,ref}} = \frac{N}{N_{ref}} \cdot \frac{\sigma_{eff}}{\sigma_{eff,ref}} \tag{2.56}$$

Which, assuming the ideal gas law, may alternatively be expressed as [105];

$$\frac{I_R}{I_{R,ref}} = \frac{\sigma_{eff}}{\sigma_{eff,ref}} \frac{T_{ref}}{T} \tag{2.57}$$

To quantify temperature from Rayleigh measurements it is therefore necessary to account for the Rayleigh cross-section. The chemical composition varies throughout a flame, which means that the Rayleigh cross-section is not necessarily constant. In combustion experiments with simple hydrocarbon fuels, the variation in Rayleigh cross-section from reactants to products can be of the order of 10% [41]. By judicious tailoring of the fuel and oxidiser flows (e.g. by adding H_2 to the fuel), the Rayleigh cross-section variation with combustion can be reduced to $\sim$2% [36]. In this way, the effect of differing Rayleigh cross-section throughout the measurement volume can be held essentially constant, and so the Rayleigh signal then only depends on the total number density (temperature). In some circumstances, changing the fuel composition is not practical, and it is necessary to correct for the variation in Rayleigh cross-section.

2.7 MILD Combustion

2.7.1 Overview

There is a continual demand to develop combustion systems that lead to reductions in emissions and increase efficiency, thereby reducing fuel consumption. It is well known that thermal efficiency may be increased by preheating of the reactants [88]. An immediate drawback of preheating techniques is that the increased peak flame temperature results in increased NO_x emissions. Alternatively, to reduce NO_x the aim is to reduce peak temperatures, which is often accompanied by an increase in other emissions, for instance carbon monoxide (CO). It is this conflict in requirements which makes the combination of low emission, high thermal efficiency burners difficult to design.

A significant development towards combustion which offers both low emissions and high efficiency was found when exhaust gases are recirculated into the reaction zone [27, 53, 58]. The heat from the exhaust gases is recovered, increasing system efficiency and also preheating of the reactants. The low oxygen concentration in the exhaust gases acts as an inert diluent which basically serves to increase the thermal mass of the system. It is this combination of using high temperature and high dilution which is the basis of the Moderate or Intense Low oxygen Dilution (MILD) combustion regime.

It has been suggested that there is an excellent potential for the use of recirculation of exhaust gases to exploit the simultaneous heating and dilution effects to achieve improvements in both the emissions and efficiency, narrowing the gap between the two objectives of low pollutant emissions and fuel savings [58].

2.7.2 Terminology / Related Technologies

In this field, a bewildering number of different terms are used to describe processes which are very similar in nature. While the descriptive titles attempt to highlight some of the subtleties of the various systems, overall many share the same, or at least very similar, underlying principles. The sheer number of terminologies which are in use leads to many being misinterpreted or being confused for another.

Rather than getting entangled in the twisted web of seemingly endless acronyms and overly descriptive names, for the sake of simplicity, in this discussion the processes will be segregated into one of two groups; preheated air combustion or MILD combustion – with MILD itself being a subgroup of the preheated group.

To some, preheated air combustion refers to a highly specific combustion regime with completely unique and characterisable features. In essence however, the origins and fundamental principle of preheating is the heating of the reactants prior to combustion; whether this is done by means of recirculation, recuperation, external heating or some other means is not particularly relevant to the fundamental aspects of the combustion for the sake of this work. While there are very important physical differences in the implementation, and in fact in the chemical processes too, preheating will be used to describe any system where the reactants are preheated. Although this may seem an oversimplification, it avoids getting bogged down in the details where this is not necessary for the issue at hand.

Preheating combustion air by means of recovering heat from the exhaust gases is recognised as one of the most effective ways of increasing the thermal efficiency of a combustion system [15, 113, 118]. The use of such exhaust gas recirculation (EGR) has been developed since the 1970's as a way of increasing furnace efficiency, and subsequently minimising fuel consumption [113]. The main drawback of increasing thermal efficiency with EGR is there can be an increase in temperatures, leading to increases in NO_x emissions. Depending on the implementation, recirculation of exhaust gases increases the content of inerts in the mixture [118].

In the extreme case of significant recirculation of combustion products, where the amount of inerts introduced by the recirculation is sufficient to alter the structure of the reaction zone, is where the MILD combustion regime lies. It can therefore be said that there is a close resemblance between preheating processes and MILD combustion. As such, it may be concluded that MILD combustion is a subset of the more general preheating principle, the difference arises from the dilution effects associated with the MILD regime. A further difference between the two is the extent of the preheating. To achieve MILD combustion conditions the temperature prior to combustion must exceed the auto-ignition temperature of the mixture, and is therefore classified as being highly preheated [27, 58].

The exact definition of the amount of preheating and recirculation required to

move from a simple preheated mode to MILD combustion is somewhat ambiguous, and this is where several different combustion regimes have been identified. One attempt at making a definition of MILD combustion has been made by Cavaliere & de Joannon [24]; "*A combustion process is named MILD when the inlet temperature of the reactant mixture is higher than mixture self-ignition temperature whereas the maximum allowable temperature increase with respect to inlet temperature during combustion is lower than mixture self-ignition temperature (in Kelvin)*". Cavaliere & de Joannon [24] claim that this definition of MILD combustion is unambiguous because the conditions are well defined and univocal — however, it is based on the theory of a well-stirred reactor (WSR) and is therefore not particularly well generalised. An alternative criterion for MILD combustion has been suggested based on the temperature variations in the flow field by Kumar et al. [66], but no definitive values were placed to indicate to general definition.

There are a number of combustion regimes that have been developed which exhibit very similar properties to MILD combustion, each having different names. While each implementation is slightly different, they all operate on very similar principles. Based on the observation that under certain conditions the MILD combustion process may result in no visible or audible flame it has been termed *flameless oxidation* (FLOX®) by Wünning & Wünning [118]. On a related theme, some similar names are flameless combustion [24], colourless combustion [113] or invisible flames [27]. Alternatively, other names have been derived using the requirement of preheating; high temperature air combustion (HiTAC), high temperature combustion technology (HiCOT) [24] or excess enthalpy combustion [113]. There are subtle differences in each of these combustion technologies, but they all rely on the fundamental principle of the reaction taking place with high dilution levels and in a high temperature environment. For this reason, a single grouping of MILD combustion seems appropriate.

2.7.3 Principles of MILD

The two basic conditions required for MILD combustion are high dilution and increased temperature of the reactants. Typically, both of these criteria are

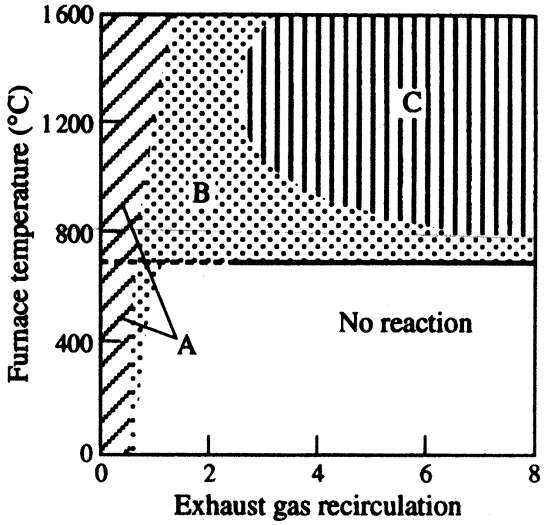

Region A - Conventional Combustion
Region B - Unstable Combustion
Region C - MILD Combustion

Figure 2.11: Stability limits of conventional and MILD combustion [118]

met by recirculation of the exhaust gases into the reaction zone. Entrainment of exhaust gases into the combustion zone is very important for the initiation of MILD combustion [88]. Depending on the characteristics of the recirculation, it is possible to achieve various combinations of recirculation rates and temperatures, resulting in different combustion modes as shown in Figure 2.11 [118].

Along the horizontal (x-axis) of Figure 2.11 is exhaust gas recirculation, and is a measure of the proportion of exhaust gas to "clean" air. Mathematically, the recirculation rate may be written as; $K_V = \dot{M}_E / \left(\dot{M}_F + \dot{M}_A\right)$ where $\dot{M}$ refers to mass flow rate, and the subscripts represent; E– recirculated exhaust gas, F– fuel, A– "clean" combustion air. The vertical (y-axis) labelled 'Furnace Temperature' refers to the temperature of the reactants.

Region A shows the domain of conventional flames, where the recirculation rate is less than ≈30%. Such flames are stable. When the recirculation rate is increased, into region B, the resultant flame has been found to become unstable. If the temperature is below the self-ignition temperature (the horizontal line at ∼700°C), these flames will extinguish. In region C, it has been found that if the

recirculation rate is increased sufficiently, and the temperature is above that of self-ignition, that stable combustion results. It is this mode of operation that is known as the MILD combustion regime.

Figure 2.11 gives an indication of a fundamental difference between conventional and MILD combustion; the vast increase in the flammability limits [87], as well as improved flame stability limits [53]. To facilitate a reaction at very low oxygen levels, and the improvement in flame stability under MILD conditions, is attributed to the temperature being above that of self-ignition, implying that the flame will always be sustained inside the furnace [58].

By diluting the oxygen stream, the combustion reaction is more distributed, in turn distributing the heat release. With the heat release occurring over a larger volume temperature peaks are avoided, thereby thermal NO formation is largely suppressed [118]. Although the heat release occurs over a larger volume, the total is the same, implying that under MILD combustion conditions the heat release rate per unit volume is lower [53].

2.7.4 Characteristics of MILD

One of the most significant effects of dilution under MILD combustion conditions is that the extent of the reaction zone increases. This in turn has the effect of creating a far more uniform temperature distribution throughout the combustion region. In addition to the spatial uniformity of the temperature distribution, there is a significant reduction in the temporal fluctuations too — a reduction in the temporal temperature RMS of 98% has been reported [53].

The distributed thermal field associated with MILD combustion also leads to the reduction of peak flame temperatures. By eliminating regions of high temperature the formation of NO_x is largely suppressed. Ten-fold reductions in NO_x emissions are possible with MILD combustion, and no specific region is identified where NO_x is formed [113]. Although the amount of NO_x produced by MILD combustion is significantly less than conventional combustion systems, some NO_x is still generated. Factors such as composition and mixing can affect the local combustion properties and thus the amount of NO_x produced. For instance, the location of the inlet nozzle (hence the mixing process) drastically affects NO_x

emissions, and cannot be attributed to imperfect combustion since no unburned hydrocarbons are measured in the exhaust [27]. Different diluents also influence the production of NO_x, with much less NO_x being formed with CO_2 dilution as compared to N_2 [53].

Despite the less intense reaction surrounding MILD combustion, both unburned hydrocarbons and carbon monoxide (CO) level are very low, or even not detectable, at the outlet of a MILD combustion furnace [113, 114]. The low emission of CO (<100ppm) suggests stable combustion conditions exist with such furnaces [53]. The temperature range encountered in MILD combustion also has significant advantages in the reduction of soot [24].

To achieve stable combustion at the low oxygen levels associated with the very high recirculation rates of MILD combustion it is necessary for the initial temperature to exceed the autoignition temperature [58]. The method of achieving recirculation can be internal or external with regard to the combustor [107]. The recirculation, typically achieved with high velocity nozzles [24], and the resultant reduction in oxygen concentration, leads to MILD combustion flames being associated with low Damköhler numbers [58]. In conventional flames, the chemical kinetics occurs much faster than the mixing, whereas under MILD conditions, the combustion is controlled by both the kinetics and the mixing [80]. As an extension to this, in a furnace environment, MILD combustion may be likened to a well-stirred reactor (WSR) as the chemical time scales becoming larger in relation to the turbulence time scales [94]. The link between MILD combustion and a well-stirred reactor may tend to indicate that this regime should be readily modelled, since a well-stirred reactor is well defined. The interaction between the turbulence and the chemistry in describing the nature of MILD combustion is expected to play a significant role however [58], and so the analogy to a WSR may not always be applicable.

One of the most noticeable characteristics of MILD combustion is the differences in visual appearance compared to other flames. When operating in MILD conditions, furnaces have been described as “glowing”, with no actual flame visible [113]. This type of description of the appearance of MILD combustion is very typical. MILD combustion is frequently described as appearing weak, with diffuse and distributed reactions zones [58].

The visible emission from MILD combustion is measured to be less than two orders of magnitude lower than from conventional flames [34]. In the case of methane, the predominate sources of colour in typical flames is due to C_2 and CH, both of which are formed at relatively high temperatures, which are avoided in MILD conditions, therefore the lack of colour [24]. Descriptions of combustors typically describe a very weak, bluish coloured flame which is barely visible [66]. The colour of the flame is also dependent on the type of fuel, with LPG fuel possibly resulting in a blue/green colour [53], but this is dependent on the diluent [24].

2.7.5 Application / Implementation of MILD

Driven by the industrial relevance, the MILD combustion process has so far predominately been implemented and investigated in furnaces. In most combustion systems, combustion efficiency is sufficiently high, but there is room for improvement in terms of heat utilisation [27]. Economical benefits are sought by increasing thermal efficiency, which can be accomplished by using preheating, and can achieve fuel savings up to 60% [114].

Large amounts of waste heat can be recovered in furnaces using heat-recovery devices to preheat the combustion air, typically above 1300K [58]. To achieve preheating, energy from the exhaust gases is transferred back to the combustion air either by recuperative or regenerative heat exchangers [94].

As an extension to using preheated air to achieve energy savings, dilution with exhaust gases has been seen to lower NO_x emissions, although the low O_2 levels require even higher preheat temperatures than generally used for previous heat recovery systems [27]. Using highly preheated air (>1100K), in conjunction with low O_2 levels (<15%), can accomplish energy savings, improved thermal performance and lower NO_x emissions [53]. Worth highlighting is that although the oxygen levels used in MILD combustion are very low, on a global level, furnaces are operated lean [66].

Preheating can also be achieved internal to the combustor by means of internal flow recirculation to provide heating of the unburnt gases (e.g. [66, 94]). Due to the high temperatures, self-ignition in MILD combustion conditions is assured

and so high-velocity jets can be used [24]. The use of high-velocity jets is advantageous to ensure adequate mixing of the fuel, air and recirculated exhaust gases is achieved to simultaneously heat and dilute the reactants [94]. Such internal recirculation is the key principle of the FLOX® burners which are at the forefront of the industrial application of MILD combustion [118].

The key features of furnaces operating in the MILD combustion regime are the increased thermal efficiency, flat thermal field and lower NO_x emissions. In relation to a conventional combustion chamber, the radiation flux is higher in the first zone on the combustor, and lower in the second part, which overall leads to a more uniform thermal field [24]. In the work of Kumar et al. [66], they found that the normalised spatial temperature variation is 15% for MILD, compared to 50% for their classical jet flame. Moreover, the heat flux uniformity achieved through MILD combustion is a highly desirable feature that often cannot be met with conventional burner technology [53]. The heat flux of a furnace operating in MILD regime has an almost constant heat flux throughout the furnace, which may provide high heat transfer rates, and is very desirable for a number of industrial processes [113]. It is estimated that MILD combustion technologies are capable of a 30% energy saving [58]. Although achieving greater efficiency can be achieved using MILD combustion, improved product quality as a result of the thermal field is also a major driving force behind the process [24].

The lack of flame and lower peak temperatures in MILD combustion may be thought to be less efficient at heat dissipation, but because of the larger reaction volume the total heat radiation flux can actually be higher in MILD combustion than in conventional flames [113]. This has been shown previously, where radiation emitted downstream from the reaction zone is about five times that emitted upstream [117], implying that although the peak temperature within MILD combustion is lower there is significant radiation emitted. Moreover, while chemiluminescence is low in MILD combustion, and may provide flames with their distinctive colours, the associated energy transfer by this mechanism is negligible in comparison with radiation from major stable compounds (such as H_2O and CO_2) [117].

As an example of the increased efficiency offered by MILD combustion, Wünning & Wünning [118] used CFD modelling to determine the input energy required to

achieve 160kW output from a furnace. Without any preheating, the burner capacity was 400kW, with 600°C preheat using a recuperator the input was 245kW [118]. For FLOX® (MILD combustion) mode, with 950°C preheat the required input was as low as 200kW – half that of the no preheat case [118]. Furthermore, the peak production rate of NO_x is reduced by several orders of magnitude [118]. This highlights why industry is seeking this technology to deal with reducing fuel costs and meeting more stringent NO_x emission targets [18].

From a practical standpoint, MILD combustion has predominately seen application in the steel industry [118]. An example is a heavy forge furnace whereby internal exhaust gas recirculation enabled the furnace to meet strict environmental regulations and an energy saving of 55% [87]. Furthermore, the homogeneous temperature field of MILD combustion makes it advantageous for use in some applications in the steel industry [24].

A schematic layout of a MILD combustion furnace is shown in Figure 2.12 from Choi & Katuski [27]. This furnace is based on an alternating flow system, and comprises of two sets of regenerators. In one flow direction, the incoming air passes over a hot ceramic honeycomb, which preheats the incoming air. As the hot exhaust gases leave the furnace at the other end they pass through another ceramic honeycomb, and subsequently heat it. After a certain period of time, the temperature of the incoming honeycomb decreases, whilst the exhaust side honeycomb has increased, and the flow direction is then reversed. The now hot honeycomb acts to heat the incoming air, whilst the cooler honeycomb is now heated by the exhaust gases. The process is then again reversed and continues the alternating heating and cooling of the regenerators.

In addition to furnace design, MILD combustion has potential for inclusion in other practical applications too. The implementation used for furnaces clearly require significant alteration for use in other applications, but, at least in principle, the underlying aspects of MILD combustion can be extended to other fields. The low temperatures and uniform thermal fields are advantageous attributes in the design of gas turbines, particularly from the materials standpoint [24]. Advancement in the application of some aspects of MILD combustion to the design of gas turbines has been made, but issues with self-ignition and dilution has meant generalised application has not yet been achieved [24].

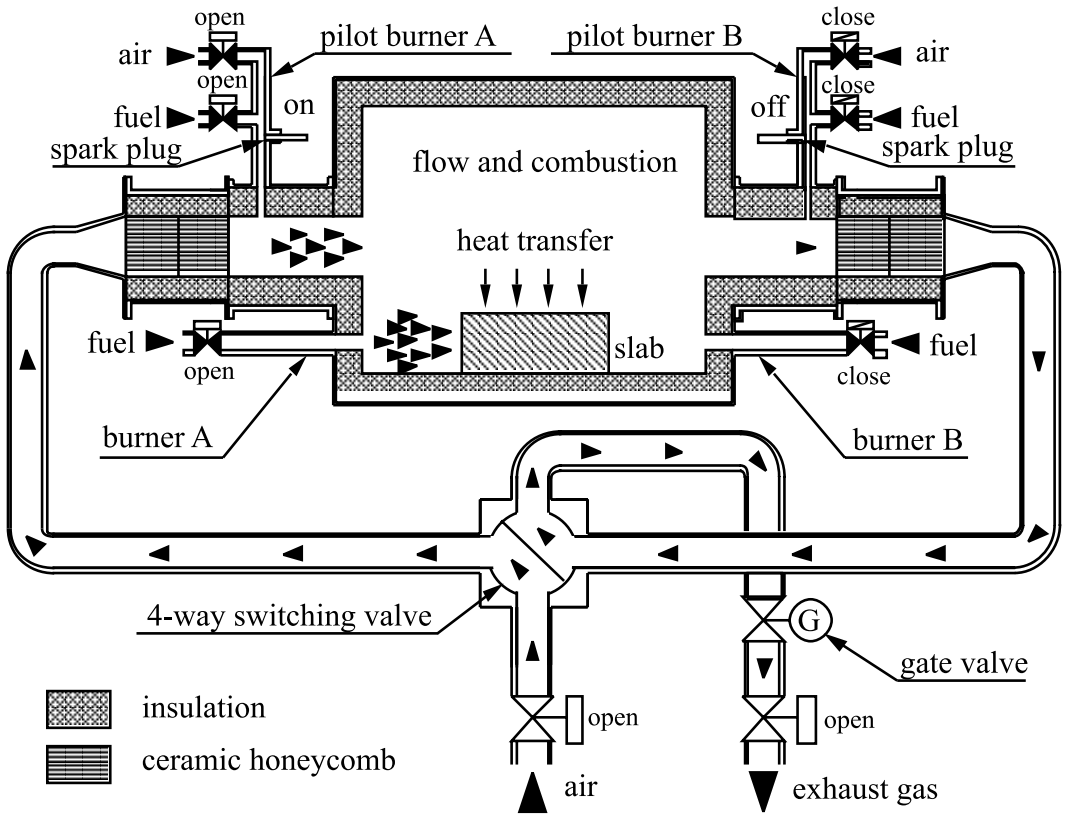

Figure 2.12: Industrially implemented MILD combustion furnace [27]

Along a similar vein, some developments which are similar to MILD combustion have been applied to diesel engines, but to date these are not what could be considered a fully fledged MILD combustion system [3, 27]. An engine which is much closer to practical implementation of MILD combustion is the homogeneous-charge compression-ignition (HCCI) engine [24]. A complete review of HCCI is well beyond the scope of this study, but there is potential for MILD combustion to advance this technology.

The preheating of combustible mixtures, which is central to MILD combustion, offers the ability to use fuels that would not typically be used – in particular, low calorific fuels [27, 58].

There is clearly potential for MILD combustion to offer significant benefits in a number of applications. One of the biggest impediments related to the implementation of this promising technology is the lack of fundamental knowledge of the reaction zone structure. A better understanding of the flame structure is needed to see widespread implementation of MILD combustion [73].

2.7.6 MILD Combustion Studies

As was highlighted in the preceding section, MILD combustion has potential for use in a number of practical applications, but this is limited by a lack of detailed understanding of fundamental aspects. Although previous research has been conducted in the area of MILD combustion, this work has predominately concentrated on large scale systems. Despite the importance of these systems, such methodology fails to address the fundamental issues of the regime.

This project seeks to differ from much of the existing research by using a well controlled experimental burner. The use of such a burner enables a wide range of combustion parameters to be easily varied, whereas the existing research has been limited in this respect. In addition, the use of an experimental burner enables laser diagnostic measurement techniques to be employed, which cannot be used effectively in the existing systems. In this way, utilising an experimental burner will avoid the limitations of previous investigations, whilst simultaneously enabling the required conditions to be emulated.

Although much of the previous study of MILD combustion has tended to be directed towards industrial systems, there have been some studies on the fundamental aspects. Due to the lack of visible flame, it has been necessary to resort to non-luminosity based techniques. As an example, Plessing et al. [94] used laser induced predissociative fluorescence (LIPF) of OH to visualise the reaction zone. In conjunction with the OH-LIPF, Rayleigh measurements were also recorded. Rayleigh scatter is particularly suitable for MILD combustion systems as the high levels of dilution result in the Rayleigh cross-section varying by less than 2% between the burnt and unburnt gases [94], further enhanced by the lack of particulate matter.

The furnace from Plessing et al. [94], has been used in further studies, including Özdemir & Peters [88], Coelho & Peters [29] and Dally et al. [32]. Özdemir & Peters [88] extended the OH and temperature measurements of the furnace by including flow field measurements, finding that strong shear is an important criteria for attaining the high mixing rates necessary to create MILD combustion conditions. Coelho & Peters [29] numerically simulated the same furnace and compared the results to the previous measurements. The models qualitatively matched the experimental results, although differences were noted near the burner exit and also in NO formation. The same furnace has also been used by Dally et al. [32] to study the effects of fuel dilution, both numerically and experimentally. They found that the shift in stoichiometry caused by fuel dilution helped in the establishment of MILD combustion.

Other furnace designs have been studied both experimentally and numerically. For instance Weber et al. [113, 114] and subsequently modelled by Mancini et al. [71]. Similar to Coelho & Peters [29], Mancini et al. [71] found that simulations matched the experiment findings, except near the jet.

On a more fundamental level, Dally et al. [30, 31] reported on the structure of hydrocarbon nonpremixed laminar and turbulent flames stabilised on a jet in a hot and diluted coflow (JHC) burner. They used single-point Raman-Rayleigh-LIF diagnostic techniques to simultaneously measure temperature, major and minor species at different locations in these flames. They found that major changes in the flame structure occur when reducing the oxygen concentration and that, at higher jet Reynolds number and low oxygen concentration, oxygen

leakage from the surroundings may cause local extinction of the flame front.

As an extension to the experimental work of Dally et al. [30, 31], CFD modelling has subsequently been applied to the same flame conditions [28, 61]. In these CFD studies, the models have shown that the experimental results can be reproduced, albeit with significant deviations in some situations. Furthermore, only some of the model variants gave good agreement. In all cases, obtaining reliable CFD models proved most difficult at the very low O_2 conditions, and the downstream measurement locations where the entrainment of surrounding air introduces an addition degree of complexity. Overall, these modelling studies indicate that there is potential for application of CFD to MILD combustion conditions, but some further work is still required.

Ahn et al. [2] reported on a heated and diluted jet of premixed methane fuel propagating against its products. The jet impinges on a cup that circulates the products back to the jet exit before it is exhausted from the side. Temperature was measured using a thermocouple and turbulence quantities were measured using Laser Doppler Velocimetry. It was shown that increasing the Karlovitz number (Ka) from $\sim$0.44 to 1.72 caused the PDF of temperature to change from Gaussian to a bimodal distribution. It was suggested that the current criteria for the transition from thin reaction zone regime to broken reaction zone regime needed to be modified when applied to a preheated and diluted mixtures.

Albeit not quite a study on MILD combustion per-se, the work of Cabra et al. [20, 21] in the vitiated coflow burner (VCB) exhibits many of the same trends as the JHC burner used in the present study of MILD combustion. Several studies have continued work using this burner. Where the JHC burner was intended to study the fundamental aspects of MILD combustion, the VCB was intended to look at lifted flames. Despite the different motivation, both of these burners consist of a jet issuing into a hot and diluted coflow of exhaust products from a secondary burner. The VCB burner was designed to decouple the chemical kinetics from the complex recirculating flow typical of practical combustors [21]. In the VCB the coflow is intended to act as a pilot – advantageous for studying lifted flames – whilst providing a uniform environment.

In a study of a laboratory MILD combustion burner it has been shown that reactions under the MILD combustion regime occur in disconnected zones where

the OH and temperature intensities differ [33, 94]. The explanation for this discontinuity between the reaction and the temperature is attributed to the varying amounts of recirculated exhaust gases, which change the balance required for MILD combustion. The conclusion of the work of Plessing et al. [94] is that MILD combustion resembles a reaction in a well-stirred reactor, although further investigations are necessary for complete analysis of MILD combustion.

It has been suggested that a furnace operating under MILD conditions is similar to a well-stirred reactor (WSR) [114]. Based on the concept of attempting to infer MILD combustion from a well-stirred reactor, de Joannon et al. [34] has attempted to model a WSR with MILD combustion conditions. This work did not compare the composition of a well-stirred reactor to any experimental data, but did examine the effect of the diluent composition. They found that there is a dramatic effect on the combustion composition, depending on the composition of the diluent. Also, the effect of the residence time on the reaction was of no significance for the majority of the temperature range 500–2000K. However as identified in their work, de Joannon et al. [34] acknowledge that a well-stirred reactor is unfeasible for a practical combustor.

The oxidation kinetics of hydrocarbon fuels is in general fairly well understood, but combustion in highly preheated oxidants with low O_2 process becomes more complicated and identification of the fuel consumption is more difficult, with only a little information available on the fundamental aspects [24, 113].

In an experimental furnace operating in the MILD combustion regime, it has been shown that the chemical composition of the diluent gas does indeed alter the structure of the exhaust gases [53]. Hasegawa et al. [53] obtained higher levels of NO_x emissions when using N_2 as the dilution gas compared to CO_2, concluding an advantage in using the burned gases. The implication of burned gases being the preferred diluent is that this saves the need to introduce an additional gas.

In summary, the experimental burner used in this study will permit MILD combustion conditions to be achieved in a well controlled environment, yet simulate operation in an industrial application. This burner will then enable a fundamental study of the factors influencing MILD combustion to be quantified by using advanced in-situ measurements of key scalars relevant to this unique type of combustion.

Chapter 3

Experimental Details

3.1 Introduction

In this study, the hydroxyl radical (OH), formaldehyde (H_2CO), and temperature are imaged simultaneously and instantaneously for various flames conditions using the Jet in Hot Coflow (JHC) burner. The JHC burner consists of a central fuel jet which issues into hot exhaust products from a secondary burner. The burner provides complete and independent control of several conditions, including fuel type, velocity/Reynolds number and coflow composition. Imaging of the identified scalars are by laser diagnostic techniques. Each of the identified scalars are measured and quantified using separate systems, incorporating several burners, which are integrated into a single experimental entity.

3.2 Burner Design

3.2.1 JHC Burner

The Jet in Hot Coflow (JHC) burner is designed to simulate conditions of strong recirculation of exhaust products, while decoupling the complex flow structures typically associated with recirculation in practical combustion devices. The motivation for this design is to simplify the conditions required to achieve MILD

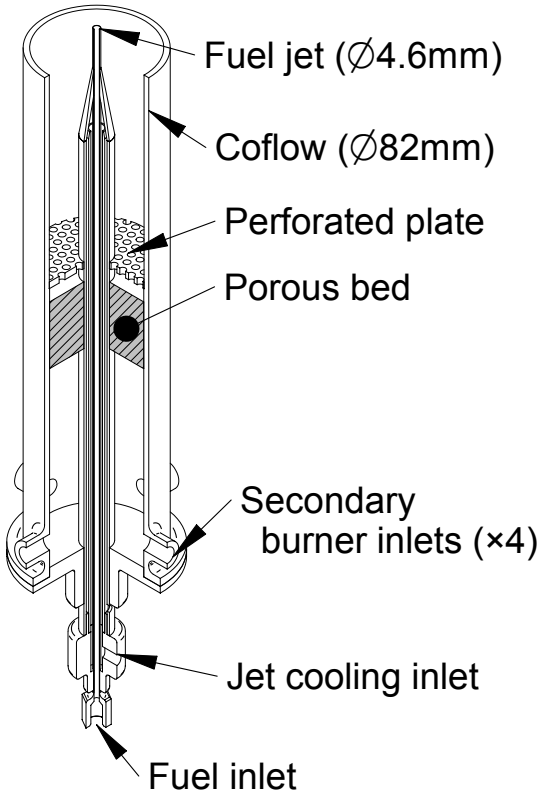

Figure 3.1: JHC burner schematic diagram

combustion in a nonpremixed mode.

The JHC burner is shown in Figure 3.1 and consists of a central insulated fuel jet (inner diameter 4.6mm, outer diameter 5.0mm) within an annular coflow (inner diameter 82mm, outer diameter 90mm) of hot exhaust products from a secondary burner. The secondary burner is a porous bed burner, with a ∼50mm layer of flint clay (approximate nominal size ∼5mm) and a perforated stainless steel plate mounted 160mm upstream of the jet exit plane. The fuel pipe is more than 100 jet diameters in length to ensure fully developed pipe flow at the exit. The outer annulus is insulated with a fibrous blanket (20mm thick) to minimise heat losses to the surrounds.

The influence of the hot coflow remains ∼100mm downstream of the jet exit plane. Beyond this the surrounding air begins to mix with the jet and coflow. The entrainment process is shown diagrammatically in Figure 3.2. The jet spreads,

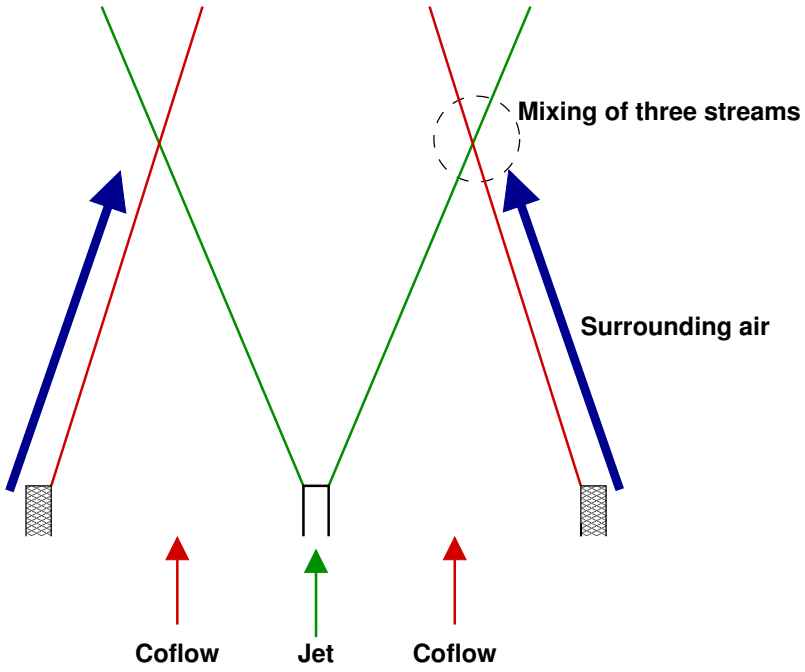

Figure 3.2: Schematic diagram showing entrainment of surrounding air on the JHC burner flame

while the internal width of the jet narrows. At the point where the jet width becomes wider than the width of the coflow, surrounding air can mix with the jet fluid, changing the composition of the oxidant stream. The surrounding air entrainment facilitates the additional study of these effects on the reaction zone.

3.2.2 Slot Burner

For reference and calibration purposes, a slot burner is incorporated into the experiment. The slot burner consists of a low velocity partially-premixed diffusion flame of natural gas and air issuing from a rectangular slot. The fuel slot is bordered by two coflowing air slots to help keep the flame steady. Figure 3.3 shows a schematic of the slot burner. A chimney fitted with a perforated plate is mounted above the burner to suppress flame fluctuations. A photograph of the slot burner with the chimney is shown in Figure 3.4.

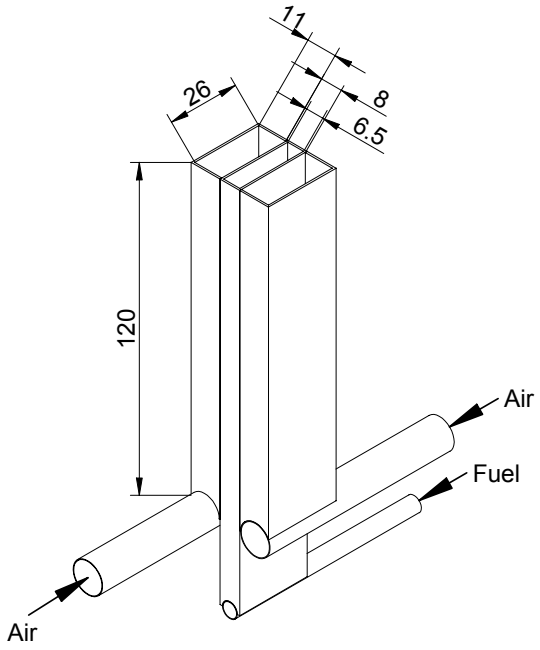

Figure 3.3: Slot burner schematic diagram

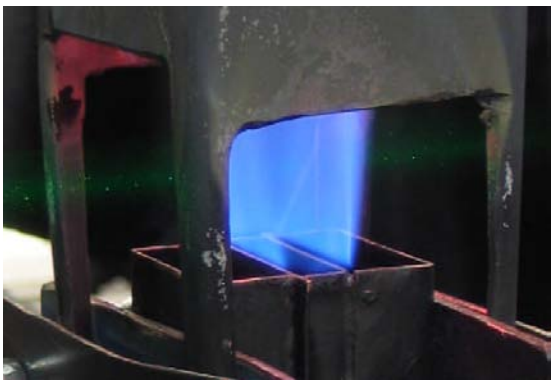

Figure 3.4: Photograph of the slot burner and partially-premixed flame

(a) (b)

Figure 3.5: Flat-flame burner photographs in two operating modes

3.2.3 Flat-Flame Burner

For validation of the laser measurements, a premixed flat-flame burner consisting of a ⌀82mm sintered bronze plate is fitted over the exit plane of the JHC burner via a 100mm extension to the outer annulus. In this arrangement, the calibration will be conducted at the same location as the experiment. This ensures the same optical properties. Flat-flame burners have been used extensively in the past as a uniform medium which is suitable for simplified modelling.

Ideally the flame front would be uniformly separated from the burner face to reduce heat losses. Due to slight imperfections in the bronze plate this was not possible. As a compromise, measurements were taken with the burner operated in two different modes. In one mode the flame was set to be "flat". When operated like this however the flame attached to the burner face, resulting in significant heat loss to the burner and subsequently affecting the ability to model this situation. To limit the effects of heat losses to the burner, the flow-rates were adjusted such that the premixed flame front is attached to the burner face at only a few locations, leaving parts of the flame front to become separated by up to ∼20mm. Photographs of the flat-flame operating in the two modes are shown in Figure 3.5. In Figure 3.5a the premixed flame is seen to be flat, but attached to the burner face. Despite the lifting of the flame, as seen in Figure 3.5b, the premixed flame is steady and is sufficiently distant from the burner face to restrict influences of heat loss to the burner. It is the second (lifted) flame that is used for calibration purposes.

Table 3.1 shows the inlet flow conditions for both modes of the flat-flame burner.

Burner mode	Nat. Gas	Hydrogen	Air	Nitrogen	Φ
1	7.22	0.13	84.5	0	0.817
2	7.22	0.13	75.4	29.7	0.916

Table 3.1: Inlet flowrates (L_n/min) and equivalence ratio for the two operating modes of the flat-flame burner

3.3 Laser Systems

3.3.1 Rayleigh Laser System

The 532nm output of a frequency-doubled Q-switched Nd:YAG laser (Quantel BrilliantB/Twins) is used as the source for the Rayleigh scatter. Although this is a double head laser, only the master head is used in this experiment. At the laser output, the measured 532nm power was ∼340mJ/pulse.

3.3.2 OH Laser System

To generate the required 283.222nm wavelength light to excite OH, a pulsed tuneable dye laser is used. A Lambda-Physik ScanMate 2E dye laser is pumped at 532nm with a frequency-doubled Q-switched Nd:YAG laser (single head Quantel BrilliantB/Twins). Using Rhodamine 590 dye, the ∼566nm output of the dye laser is frequency doubled using a doubling unit extension to obtain the ∼283nm. To isolate the desired wavelength, the output is also passed through a four-element Pellin-Broca array. The measured output power was ∼2mJ/pulse, with a linewidth of 0.5cm^{-1}.

3.3.3 H_2CO Laser System

The 340.836nm to excite H_2CO is generated with a separate tuneable dye laser. A Quantel TDL90 dye laser is pumped with a 532nm beam from a Quantel YG980 Q-switched Nd:YAG laser. The dye used is Pyridine 1, which is frequency-doubled within the TDL90 to obtain the required ∼340nm. The measured output power was ∼10mJ/pulse, with a linewidth of 0.26cm^{-1}.

3.3.4 Wavelength Calibration

The output wavelength from the dye lasers were determined using a calibrated Burleigh WA-5500 UV-pulsed wavemeter. It was found that the wavelengths from the lasers were very stable, and although confirmed periodically, these did not require regular adjustment. For LIF excitation, to verify the wavelengths, the lasers were tuned on- and off-resonance around nearby excitation peaks to confirm excitation occured at the expected locations. Furthermore, for the H_2CO-LIF, the peak response wavelength was verified against the signal from the vapour from a formaldehyde solution.

3.4 Experimental Layout

The experiment involves the integration of numerous systems which are required to be integrated. Two main systems are identified, viz.; the optical and the electrical/timing systems, which are detailed in the proceeding sections.

3.4.1 Optical Layout

The experimental layout is shown diagrammatically in Figure 3.6. The three laser wavelengths are formed into overlapping co-planar laser sheets. The laser sheets pass through a laminar slot burner (for reference purposes) in the same field of view as the JHC burner. The laser pulses are fired sequentially to reduce interferences on the other systems. Each species is detected normal to the laser sheet with a gated intensified CCD (ICCD) camera. To accommodate three separate cameras, a dichroic mirror is used between the OH and Rayleigh cameras. The dichroic mirror is centred at 308nm, and has a reflectance greater than 80% in the range 270–340nm, therefore acting as a broadband filter for the OH camera. The H_2CO and Rayleigh cameras were each fitted with long wave pass optical filters, GG-385 and GG-495 respectively. To minimise elastic scatter from particulate matter, gases were filtered and measurement locations chosen which were free of visible soot. The Rayleigh and H_2CO cameras were both used with $f_{\#}1.2$ lenses, and OH with a $f_{\#}4.5$ lens. The in-plane resolution of all three

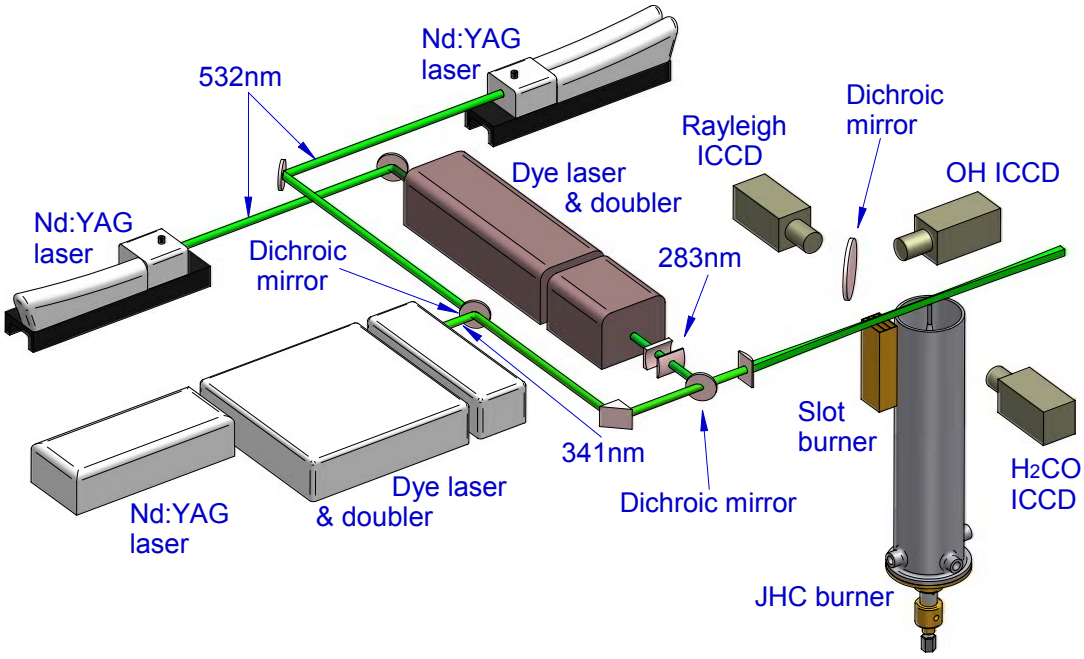

Figure 3.6: Pictorial representation of experimental layout

ICCD cameras is 160µm, after spatial matching. The light sheet thicknesses are estimated to be slightly larger than this, but of a similar order based on burns from photosensitive paper. The laser sheet heights were all ∼12mm, of which the central 8mm portion is presented herein. Figure 3.7 shows the details of the optical layout.

3.4.2 Timing Details

To ensure that all laser and camera systems are synchronised, a centralised timing system is adopted. In addition to the lasers and cameras, a few additional components are used for control purposes, namely two DG-535 Stanford Research Systems pulse/delay generators, and some minor logic gates. The various devices are all TTL (+5V high; high impedance) and connected as shown in Figure 3.8.

The lasers each require two inputs (when operated in external mode); one to trigger the flashlamp(s) and another for the Q-switch. Although other timing configurations are possible, this fully externally triggered mode has been chosen

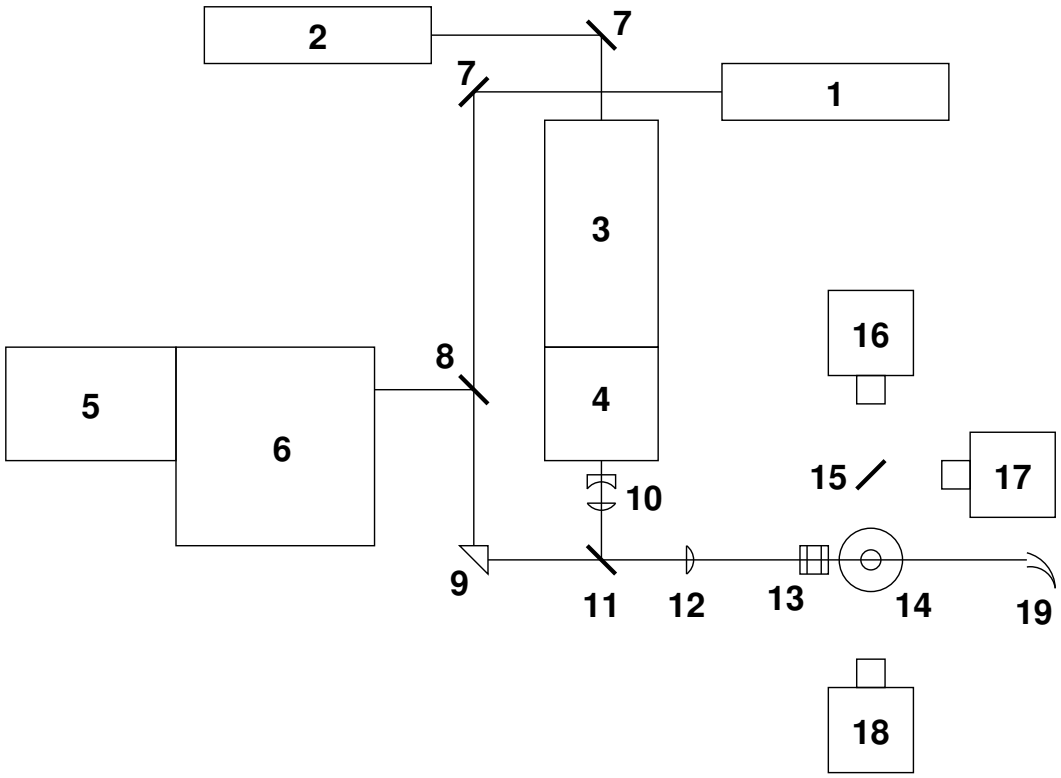

1) Quantel BrilliantB/Twins double-head Nd:YAG laser
2) Quantel BrilliantB/Twins single-head Nd:YAG laser
3) Lambda-Physik ScanMate 2E dye laser
4) Lambda-Physik ScanMate 2E doubling unit
5) Quantel YG980 Nd:YAG laser
6) Quantel TDL90 dye laser
7) High reflectivity 45° incident angle 532nm mirror
8) 1″ Dichroic mirror (transmit 532nm, reflect 340nm)
9) Fused silica prism
10) Fused silica cylindrical lens vertical telescope (f=–25mm & f=100mm)
11) 1″ Dichroic mirror (transmit 340 & 532nm, reflect 283nm)
12) Fused silica cylindrical lens (vertical optical axis), f=750mm
13) Reference slot burner
14) JHC burner
15) 2″ Dichroic mirror (transmit 532nm, reflect 308nm)
16) Rayleigh camera: Princeton Instruments ICCD, $f_{\#}$1.2 lens & GG-495 filter
17) OH camera: Roper Scientific ICCD, $f_{\#}$4.5 lens
18) H_2CO camera: Princeton Instruments ICCD. $f_{\#}$1.2 lens & GG-385 filter
19) Beam dump

Figure 3.7: Schematic details of experimental layout

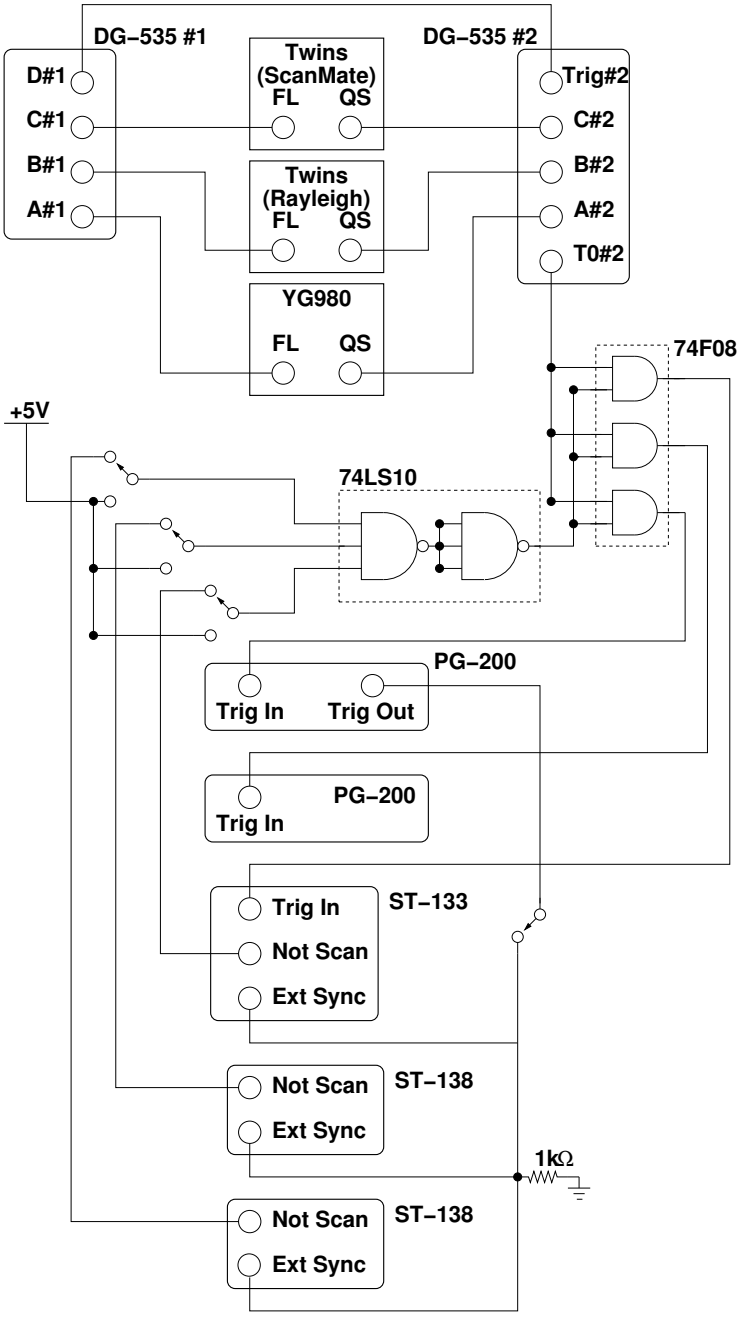

Figure 3.8: Timing connexions for the lasers and cameras

for the additional control required. For thermal stabilisation, both the flashlamps and Q-switches of all lasers need to operate at 10Hz.

The exposure of each camera needs to be synchronised with the firing of the corresponding laser pulse. While the lasers must be operated at 10Hz, the cameras are not capable of operating at this repetition rate, and in fact, the maximum repetition rate of each camera is different, and is not necessarily constant. It is therefore necessary to take care in the control of each camera.

Two somewhat different model ICCD cameras are used (Princeton Instruments ICCD or Roper Scientific ICCD), each requiring a slightly different timing arrangement. Both cameras feature a combined intensifer/CCD within a single camera head, and an external controller/controllers (depending on the model). The Princeton Instruments cameras have a separate high-voltage controller (PG-200) to trigger the intensifier, and a camera controller (ST-138) to read and control the CCD. The Roper camera controller has the intensifier and CCD controllers integrated into a single unit (ST-133). Each of the intensifier controllers features an internal delay so that the delay between receiving a pulse on the input trigger terminal and triggering the intensifier can be adjusted to match the arrival of the laser pulse.

The different camera models required a slightly different controlling arrangement, but essentially, each of the ICCD cameras requires a trigger for the intensifier, and subsequently a pulse to read the CCD array. The trigger to read the array is generated within one of the PG-200 HV controllers and delayed sufficiently after all of the laser pulses have fired. This pulse, which is sent to all of the camera controllers to read the CCD arrays will always occur *after* the intensifier has been triggered.

While the data is being transferred from the camera to the host computer it is important not to attempt to record a new image as this would corrupt both the existing and the new images. The ST-138 type controllers do not inherently limit such "double exposures" and so these must be avoided externally. The NOT SCAN of each of the controllers facilitates the use of preventing a new image whilst an existing data transfer is occurring. The NOT SCAN from each of the controllers are tied together as a single line which inhibits the triggering of the intensifiers, and subsequently the reading of the CCD arrays.

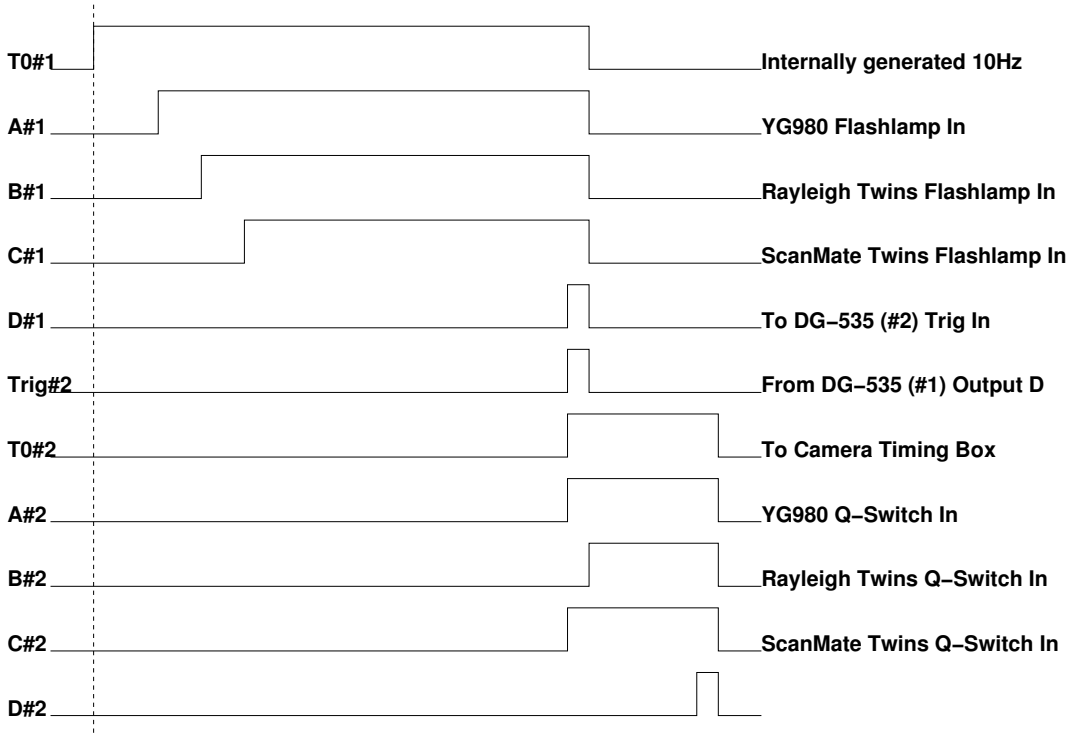

Figure 3.9: Timing diagram of Stanford DG-535 pulse delay/generator

Figure 3.9 shows the relative timing sequence for a single pulse, as controlled by the two DG-535 Stanford pulse delay/generators.

The three switches seen at the input of back-to-back triple-input NAND gate pair in Figure 3.8 are provided for testing purposes, so that any of the NOT SCAN signals can be over-ridden if a particular laser system is not in use. This is solely for preliminary testing, and was never used during experimentation. The other switch in Figure 3.8 is used to ensure that all cameras start recording on the same pulse. Due to noise issues, in some of the later runs, the control of the PG-200 Out — EXT SYNC signal was achieved by switching a 50Ω terminator to the $\overline{\text{INHIBIT}}$ of the PG-200 to prevent output from Trig Out. This alternative has exactly the same effect as physically switching the signal line itself. (Note that for either configuration the switch *does not* prevent the intensifiers, and so multiple exposures are able to accumulate on the CCD, therefore the first few images in a data set are discarded to ensure the CCD has been thoroughly cleaned.) The

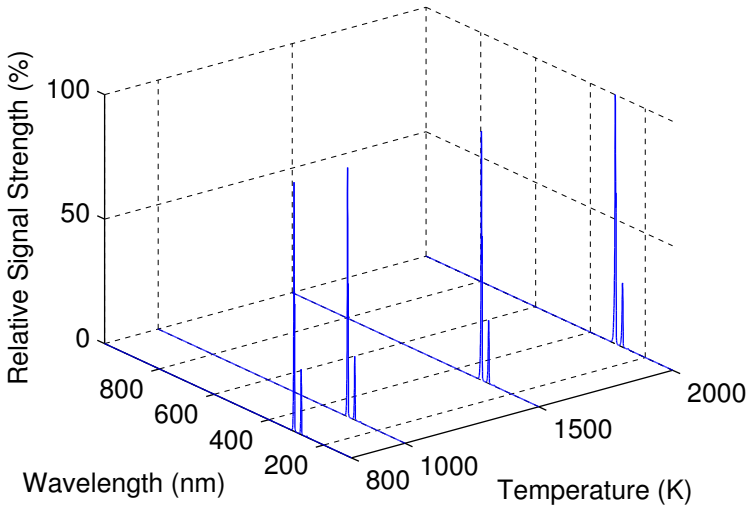

Figure 3.10: OH-LIF excitation

resistor shown ensures that the EXT SYNC inputs are pulled low when a pulse is not being received.

3.5 OH Spectroscopy

3.5.1 OH Major Features

One of the most important in-situ flame species is the hydroxyl radical (OH). Due to its importance, it has been well studied and much of the spectroscopy has been already identified. Use of this previous knowledge has been compiled in the software programme LIFBASE [67], which permits the excitation wavelengths to be calculated as a function of temperature, as is seen in Figure 3.10.

For generation of Figure 3.10 the $A - X$ transition of OH was selected since it results in the strongest signal, and has previously been the most widely implemented scheme. Figure 3.10 clearly shows that over the temperature range of interest, the only region in which there is LIF signal is 200–400nm. By concentrating on this wavelength region, Figure 3.11 shows the excitation spectra overlaid for various temperatures.

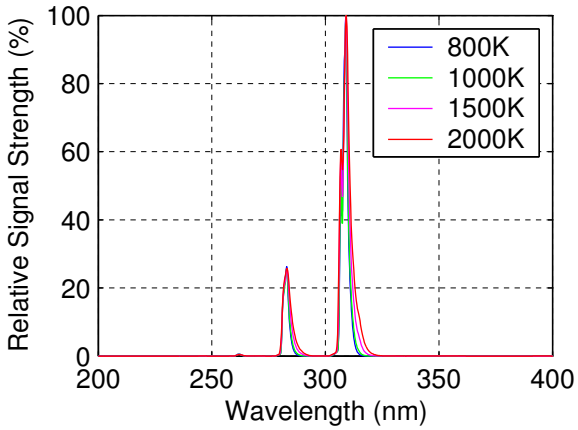

Figure 3.11: OH-LIF excitation features

v'	0	1	2	3	4
Wavelength (nm)	308.900	282.792	262.089	245.407	231.835

Table 3.2: OH-LIF excitation wavelengths of the $A - X$ electronic band from ground state vibrational level v''=0

Figure 3.11 indicates that the effect of increasing the temperature is to slightly broaden the peaks, although this effect is relatively minor. The effect of temperature on the actual signal strengths cannot be inferred from this figure since each temperature is shown relative to its peak. The dominate peaks seen in Figure 3.11 correspond to the vibrational levels originating from the $v'' = 0$ vibrational level in the ground state, and may alternatively be expressed in tabular form, as in Table 3.2. Over the temperature range of interest, only the $v' = 0$ and $v' = 1$ transitions are identifiable.

From Figure 3.11 it is apparent that the peak at ∼308nm ($A - X$ $(0 - 0)$) transition is the strongest. From a practical standpoint, excitation of a $A - X$ $(0 - 0)$ transition has problems since elastic scatter of the incident beam cannot be separated from the LIF emission. Excitation of the $A - X$ $(0 - 1)$ transition helps alleviate this issue, whilst still providing a strong excitation scheme.

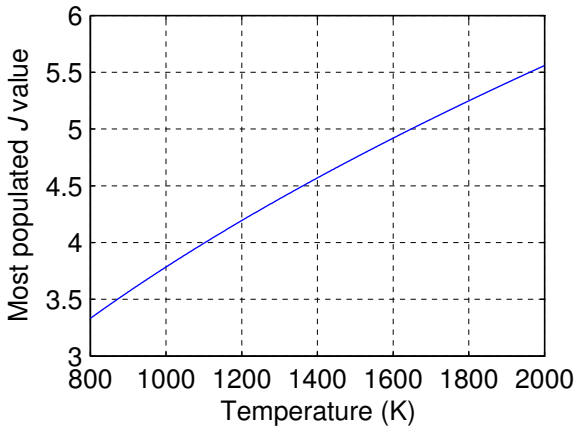

Figure 3.12: Maximum J value for OH

3.5.2 OH Rotational Energy

The rotational constant of OH is: B=18.9 cm^{-1} (=1890 m^{-1}) [41]. Based on this constant, and the previously defined equation 2.49, it is possible to find the rotational energy J value that will yield the peak populations for OH.

$$J_{max} = \sqrt{\frac{kT}{2hcB}} - \frac{1}{2} \tag{2.49}$$

In equation 2.49, it is seen that the only variable is the temperature, T, with k, h, c and B all being constant. As such, it is possible to create a plot of the J value that will give the maximum population depending on the temperature, as is shown in Figure 3.12.

While Figure 3.12 enables a J value to be chosen that results in the maximum population, this will not necessarily be the most suitable value. In this experiment, the OH will exist over a range of different temperatures. As such, it is advantageous to select a J value that will essentially be insensitive to temperature variations. Previously equation 2.51 was derived which gave the J value for a diatomic that is least sensitive to temperature (J^*).

$$J^* = \frac{-1 \pm \sqrt{1 + \frac{4k\bar{T}}{hcB}}}{2} \tag{2.51}$$

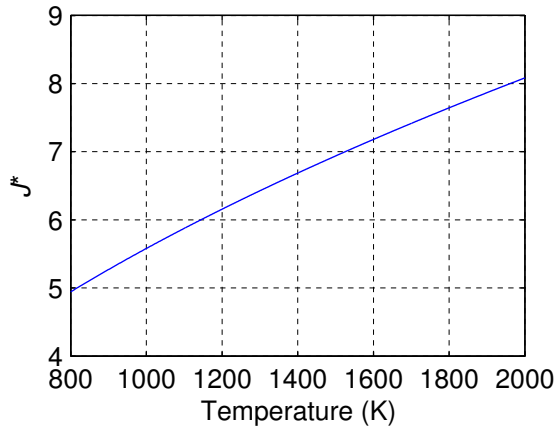

Figure 3.13: Least sensitive J value for OH

Again, in equation 2.51 the only variable is the temperature, enabling a plot of J^* against temperature to be produced, as in Figure 3.13.

Comparing Figure 3.12 and Figure 3.13 it is seen that the J value that yields the maximum signal does not correspond to that which is least sensitive to temperature effects. In situations such as this, where the temperature is not isothermal, it is common practice to simply select the J value based on J^* evaluated at some average temperature. Rather than simply using J^* as a guide to the optimal J value, the actual distribution of the energy states will be examined for the temperature range of interest. This may be performed using the previously defined equation 2.48;

$$f_{rot} = \frac{hcB}{kT} \cdot (2J+1) \cdot \exp\left[\frac{-hcBJ(J+1)}{kT}\right] \tag{2.48}$$

Based on equation 2.48, it is possible to create a plot of the populations for differing J values over a temperature range, as shown in Figure 3.14.

From the data obtained in Figure 3.14 it is then possible to determine the extent of the population variation over the temperature range, as shown in Figure 3.15.

Figure 3.15 indicates that a J value around 7 results in the minimum population variation ($\sim$10%) over the full temperature range.

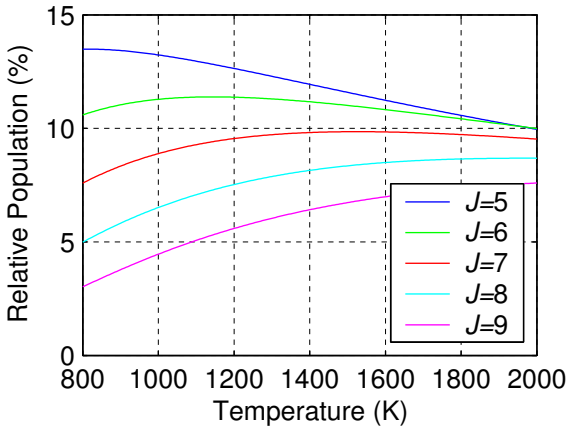

Figure 3.14: OH population distribution for various J values

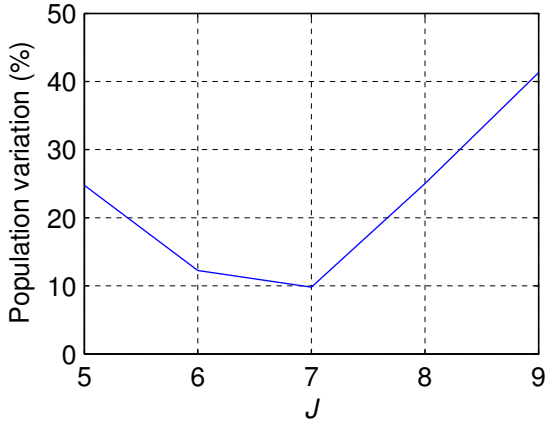

Figure 3.15: Population variation of OH between 1000–2000K for various J

3.5.3 OH Excitation Scheme

From the information in the preceding sections, the excitation scheme consists of $A - X$ electronic excitation from ground state vibrational level $v'' = 0$ to $v' = 1$, with rotational level $J'' = 7$. After experimental investigation, spin-state 1 is selected. The OH-LIF excitation scheme is therefore;

$$\mathrm{OH - LIF} \ : \ A^2\Sigma - X^2\Pi\,(1,0)\,Q_1(7)$$

Using the LIFBASE software [67], it is found that the wavelength corresponding to this transition is 283.222nm (in air).

3.5.4 OH Boltzmann Distribution

The rotational population in the preceding section was selected to give a relatively constant ground-state population, nevertheless, these calculations were based on simple diatomic theory, and without any consideration given to the other energy level populations.

Electronic Even at the elevated temperatures experienced in flames, prior to excitation, virtually the entire ground-state population exists in the X level. It is therefore unnecessary to calculate this effect.

Vibrational Using the constants from [37], the vibrational energy may be calculated from the previously defined equation 2.40;

$$E_v = hc\left[\left(v + \frac{1}{2}\right)\omega_e - \left(v + \frac{1}{2}\right)^2 \omega_e x_e\right] \tag{2.40}$$

The vibrational partition function (q_{vib}) is found from;

$$q_{vib} = \sum_v exp\,(-E_{vib}(v)/kT) \tag{3.1}$$

The vibrational Boltzmann population is then;

$$f_{vib}(v) = \frac{exp\left(-E_{vib}(v)/(kT)\right)}{q_{vib}} \tag{3.2}$$

Rotational The ground electronic energy level of OH is a $^2\Pi$ state (i.e. $\Lambda = 1$) therefore both lambda-doubling and electron spin coupling occurs, both affecting the rotational energy levels. The impact of the lambda-doubling is very minor [41] however, and is neglected herein. Hund's case (b) may be used to approximate the spin-coupling, such that two rotational energy levels may be identified (corresponding to parallel and anti-parallel spin respectively);

$$E_{rot,1}(N) \quad : \quad J = N + \frac{1}{2} \tag{3.3}$$

$$E_{rot,2}(N) \quad : \quad J = N - \frac{1}{2} \tag{3.4}$$

Where J is the rotational quantum number and N is the angular momentum quantum number (apart from spin). The assumption of Hund's case (b) is valid only at high J (at low J, Hund's case (a) is a better approximation). To account for the intermediate case, Dieke & Crosswhite [37] suggest modified rotational energy level expressions;

$$E_{rot,1}(N) = B\left[(N+1)^2 - 1 - \frac{1}{2}\sqrt{4(N+1)^2 + a(a-4)}\right] - DN^2(N+1)^2 \quad ; \; J = N + \frac{1}{2} \tag{3.5}$$

$$E_{rot,2}(N) = B\left[N^2 - 1 + \frac{1}{2}\sqrt{4N^2 + a(a-4)}\right] - DN^2(N+1)^2 \quad ; \; J = N - \frac{1}{2} \tag{3.6}$$

The rotational partition function is given by the summation over all rotational levels, therefore;

$$q_{rot} = \left\langle \sum_{J=0}^{\infty} [(2J+1) \cdot exp\,(-E_{rot,1}(J)/(kT))] \right\rangle + \left\langle \sum_{J=0}^{\infty} [(2J+1) \cdot exp\,(-E_{rot,2}(J)/(kT))] \right\rangle \quad (3.7)$$

Since the rotational energy level is dependent on the spin-state, to find the rotational Boltzmann population it is necessary to stipulate the spin-state, such that;

$$f_{rot,1}(J) = \frac{(2J+1) \cdot exp\,(-E_{rot,1}(J)/(kT))}{q_{rot}} \quad (3.8)$$

$$f_{rot,2}(J) = \frac{(2J+1) \cdot exp\,(-E_{rot,2}(J)/(kT))}{q_{rot}} \quad (3.9)$$

Combining equations 3.2 & 3.8 gives the ground-state Boltzmann population distribution for spin-state 1;

$$f(v,J) = f_{vib}(v) \times f_{rot,1}(J) \quad (3.10)$$

Figure 3.16 presents the variation of the $X^2\Pi_{3/2}$ (ground-state, spin-state 1 (i.e. aligned parallel)) with $v'' = 0$ and N=7.

3.6 Formaldehyde Spectroscopy

This section describes the methodology to select the optimal excitation scheme of formaldehyde LIF. Primarily, consideration is given to the Boltzmann fraction distribution in order to find the most suitable quantum energy levels to excite.

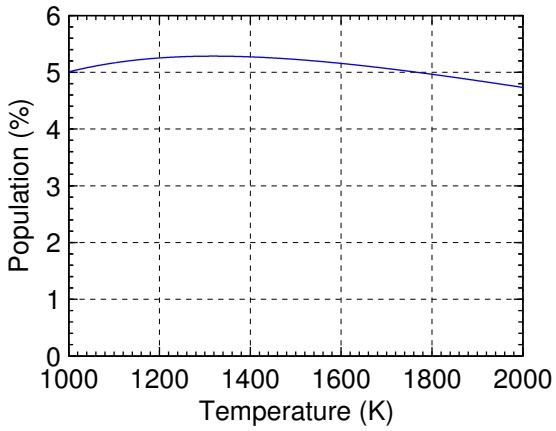

Figure 3.16: OH Boltzmann population distribution (X-state, $v'' = 0$, $J'' = 7.5$, $\Omega = {}^3/_2$).

The purpose is to find an excitation scheme which yields a large population fraction (and hence maximum LIF signal) but also be relatively independent on the temperature. In the survey of previous formaldehyde LIF experiments in §2.6.2, based on the work of Paul & Najm [91] the $A - X$ $2_0^1 4_0^1$ band has been shown to be the most advantageous in terms of signal strength. Nevertheless, the optimal rotational energy levels must still be found, and also the temperature dependence of the selection excitation scheme so that appropriate corrections for Boltzmann fraction may be made.

3.6.1 Formaldehyde Notation

Being a polyatomic molecule, formaldehyde (H_2CO) has a slightly different notation to simpler diatomics, such as OH. Out-of-plane motions also gives rise to multiple vibrational modes (each having numerous energy levels). For formaldehyde these vibrational modes occur as shown in Figure 3.17 from Emery et al. [42].

Annotation of the vibrational modes is of the form; $\nu_{v'}^{v''}$. For example, 4_0^1 implies the excitation of vibrational mode 4 from level 0 to 1. It is also possible to have more than one simultaneous vibrational mode excitation, for example the $2_0^1 4_0^1$ combination transition.

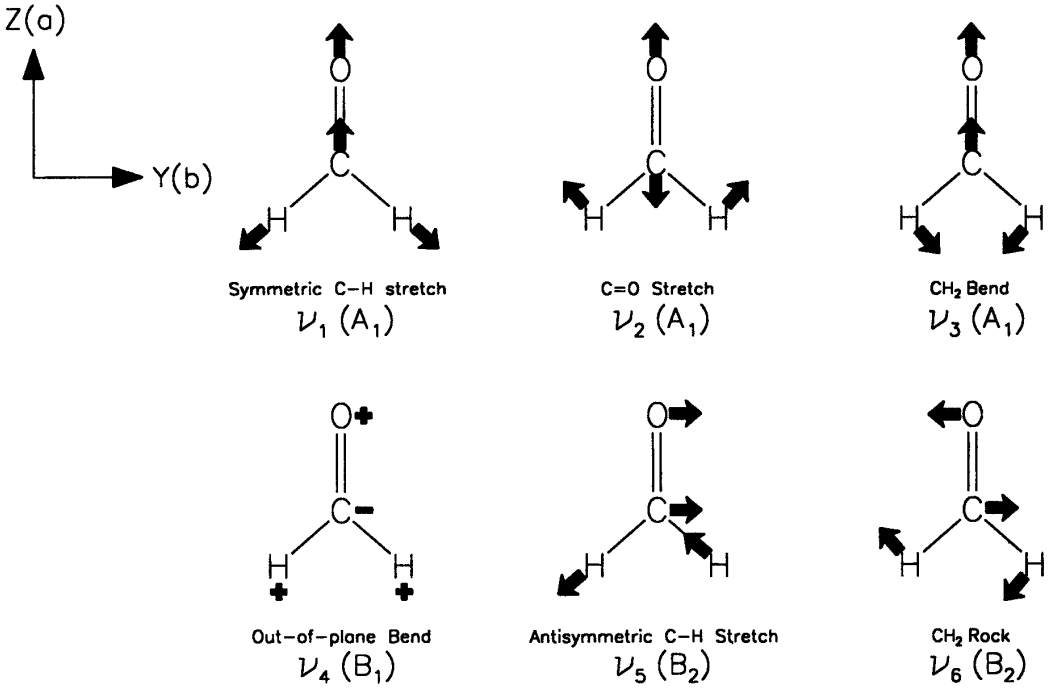

Figure 3.17: Vibrational modes of formaldehyde [42]

The rotational designation of formaldehyde is similar to diatomics, but includes a second rotational energy as follows; ${}^{a}b_{c}(d)$, where; $a = \Delta K$, $b = \Delta J$, $c = K''$, $d = J''$. For example, ${}^{p}R_3(9)$ is equivalent to; $\Delta K = -1$, $\Delta J = +1$, $K'' = 3$, $J'' = 9$.

3.6.2 Formaldehyde Vibrational Population

The vibrational energy states are taken from the work of Maessen & Wolfsberg [70]. From the tabulated vibrational energy levels, the vibrational Boltzmann population distribution may be found, using the standard Boltzmann distribution definition defined previously, and repeated here;

$$f_i = \frac{g_i \cdot exp\left(-E_i/kT\right)}{q} \tag{2.43}$$

Since the vibrational energy levels have been individually identified, there is in-

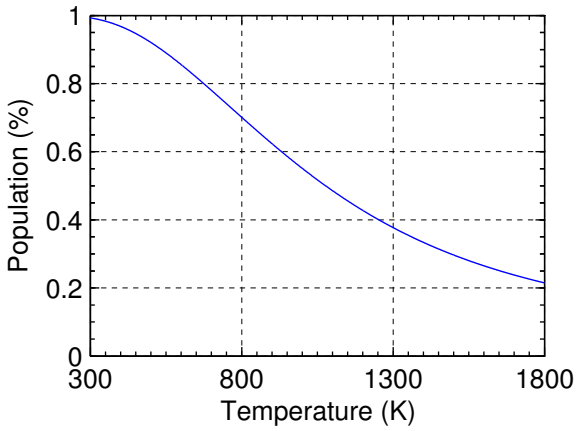

Figure 3.18: Vibrational ground-state formaldehyde Boltzmann distribution for v=0

herently no degeneracy.

From the tabulated energy levels (E_{vib}), the vibrational partition function (q_{vib}) is simply given by the summation of each energy level (v);

$$q_{vib} = \sum_{i} exp\left[-E_{vib}(v_i)/(k \cdot T)\right] \tag{3.11}$$

The Boltzmann population at a given temperature, for a particular vibrational energy state (v) is then given by;

$$f_{vib}(v) = \frac{exp\left[-E_{vib}(v)/(k \cdot T)\right]}{q_{vib}} \tag{3.12}$$

As identified in the introduction of this section, it has already been identified that that vibrational mode which is being targeted in the experiment is the $2_0^1 4_0^1$ band. This means that the ground-state is vibrationless (v=0). Using equation 3.12, Figure 3.18 presents the effect of temperature on the vibrationless ground-state population.

From Figure 3.18 it is apparent that at low temperatures almost the entire ground-state population is vibrationless, but at higher temperatures this is not the case, as the population becomes spread over a greater number of vibrational modes.

3.6.3 Formaldehyde Rotational Population

Formaldehyde is a slightly asymmetric, near prolate molecule [25]. The level of asymmetry however is quite small, with an asymmetry parameter, $\kappa = -0.96$ [83]. The extent formaldehyde differs from a symmetric top is small, and is further reduced at increased rotational (K) quantum numbers [38], permitting an approximation of the energy using symmetric top theory. For a symmetric top molecule [4];

$$\frac{E_{ang}(J,K)}{hc} = BJ(J+1) + (A-B)K^2 \tag{3.13}$$

Where;
E_{ang} is the angular energy level – a function of J and K
h is Planck's constant ($h = 6.626 \times 10^{-34}$ J·s)
c is the speed of light
J, K are the rotational quantum numbers. $J = 0, 1, 2, ...$ and $K = -J, ..., J$
A, B, C are the rotational constants of formaldehyde [82];

$$\begin{aligned} A &= 281,970\,\text{MHz} = 939.1\,\text{m}^{-1} \\ B &= 38,836\,\text{MHz} = 129.45\,\text{m}^{-1} \\ C &= 34,002\,\text{MHz} = 113.34\,\text{m}^{-1} \end{aligned}$$

Using the definition given by equation 2.44, the angular momentum partition function (q_{ang}) is found from;

$$q_{ang} = \sum_{J=0}^{\infty} \sum_{K=-J}^{J} \left(g \cdot exp\left[-E_{ang}(J,K)/(k \cdot T)\right]\right) \tag{3.14}$$

Where;
g is the state degeneracy; $g = 2J + 1$
k is Boltzmann's constant ($k = 1.38 \times 10^{-23}$ Joules/Kelvin)
T is the temperature in Kelvin

The rotational Boltzmann distribution for a given J and K is then given by;

$$f_{ang}(J,K) = \frac{2 \cdot g \cdot exp\left[-E_{ang}(J,K)/(k \cdot T)\right]}{q_{ang}} \tag{3.15}$$

Note that the multiplier of two (2) which appears at the front of this expression is as a result of the K^2 term ($K \neq 0$) in equation 3.13. As a result of the assumed symmetry in this expression, symmetric molecules are said to be doubly degenerate, known as k-degeneracy. This degeneracy is the result of in- and out-of plane vibrations [41]. The k-degeneracy is in effect a selection degeneracy and was not included in the definition of degeneracy $g = 2J + 1$, but was inherently taken into consideration with the $-J...J$ limits on K in finding the partition function (equation 3.14).

To determine the effects of temperature on the rotational energy levels, Figure 3.19 has been generated. Each of the subplots of this figure shares the same (arbitrary) vertical scaling.

Figure 3.19 shows that higher Boltzmann fractions are possible for low K values, however for a single J value the temperature dependence is a lot greater than at higher K. From an experimental standpoint, it is desirable to have a large Boltzmann fraction to achieve the best signal (i.e. low K), but also minimise the temperature variation (i.e. high K). It is therefore apparent that a compromise will be required.

3.6.4 Formaldehyde Boltzmann Population Distribution

By combining the Boltzmann fraction population of the vibrational and rotational energy modes, the combined ground-state population fraction is simply found from;

$$f_{pop}(v,J,K) = f_{vib}(v) \times f_{ang}(J,K) \tag{3.16}$$

From this expression it would be possible to plot the combined Boltzmann fraction population, however not only does the ground-state population need to be determined, but there is an addition aspect that should also be considered, namely the intensity weighting depending on the transition.

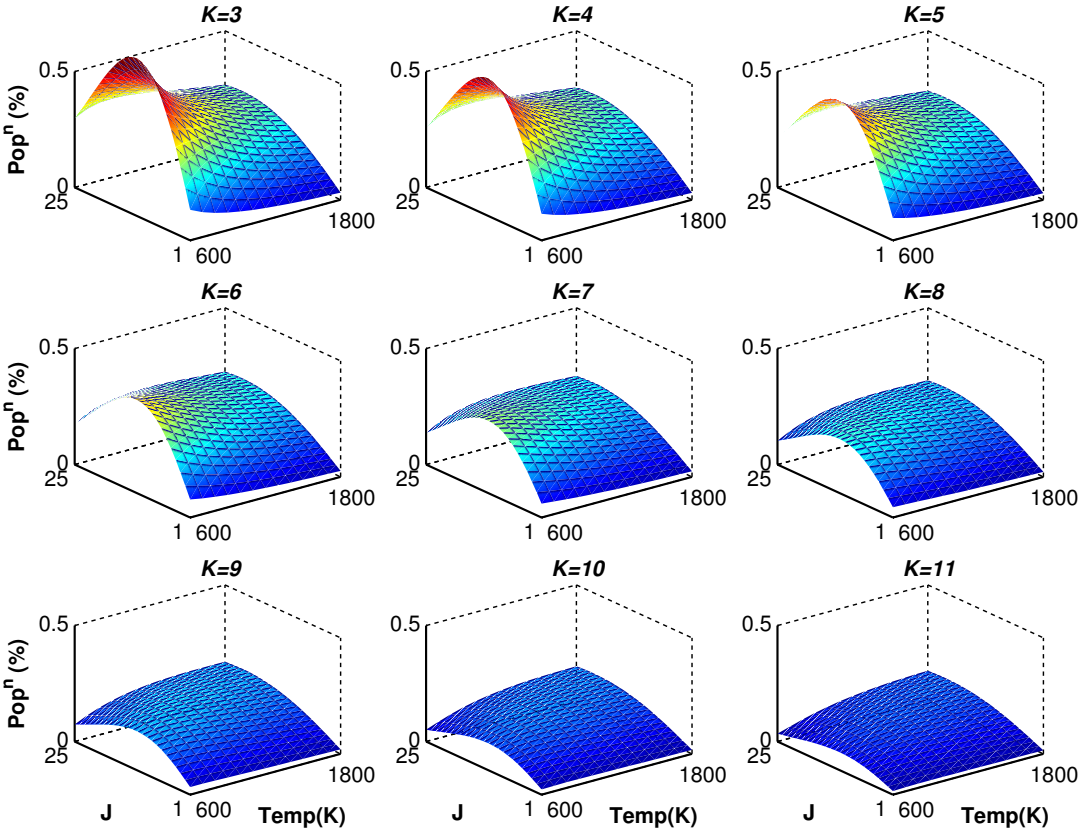

Figure 3.19: Formaldehyde rotational Boltzmann distribution for various K (Note: constant vertical scaling)

3.6.5 Formaldehyde Spectral Intensities

Depending on the nature of an individual transition, the intensity factor for the branch is different. The intensity weightings are given as follows [38];

$$\left.\begin{array}{l} rR(K-1,J-1) \\ pP(K,J) \end{array}\right\} \frac{A(J+K-1)(J+K)}{8J}$$
$$\left.\begin{array}{l} pQ(K,J) \\ rQ(K-1,J) \end{array}\right\} \frac{A(2J+1)(J-K+1)(J+K)}{8J(J+1)} \qquad (3.17)$$
$$\left.\begin{array}{l} pR(K,J-1) \\ rP(K-1,J) \end{array}\right\} \frac{A(J-K+1)(J-K)}{(J+K)(J+K-1)}$$

From Dieke & Kistiakowsky [38] it has been ascertained that the pR and rP branches are so weak that they are not worth considering. The remaining combinations share one of two intensity factors, each of which has been plotted separately, although with the same vertical scaling. It should be noted that the rR and rQ branches have slightly different J and K values caused by an offset of 1 unit (as indicated in equation 3.17). Using the Boltzmann fraction equation 3.16 coupled with the intensity weightings of equation 3.17, Figures 3.20 & 3.21 have been generated. Each of the subplots of these figures share the same (arbitrary) vertical scaling.

Figures 3.20 & 3.21 indicate that there are some differences in the intensity between the different branches. The key points of interest may be summarised as;

- pQ& rQ branches have a greater intensity than rR & pP for low K, but this trend is reversed at high K.
- Small K values (irrespective of the branch) are stronger. However, at small K (for a given J) the variation in intensity is more temperature dependent than at higher K.
- In either branch the intensity appears to reach a maximum over the range of $J \gtrsim 20$.

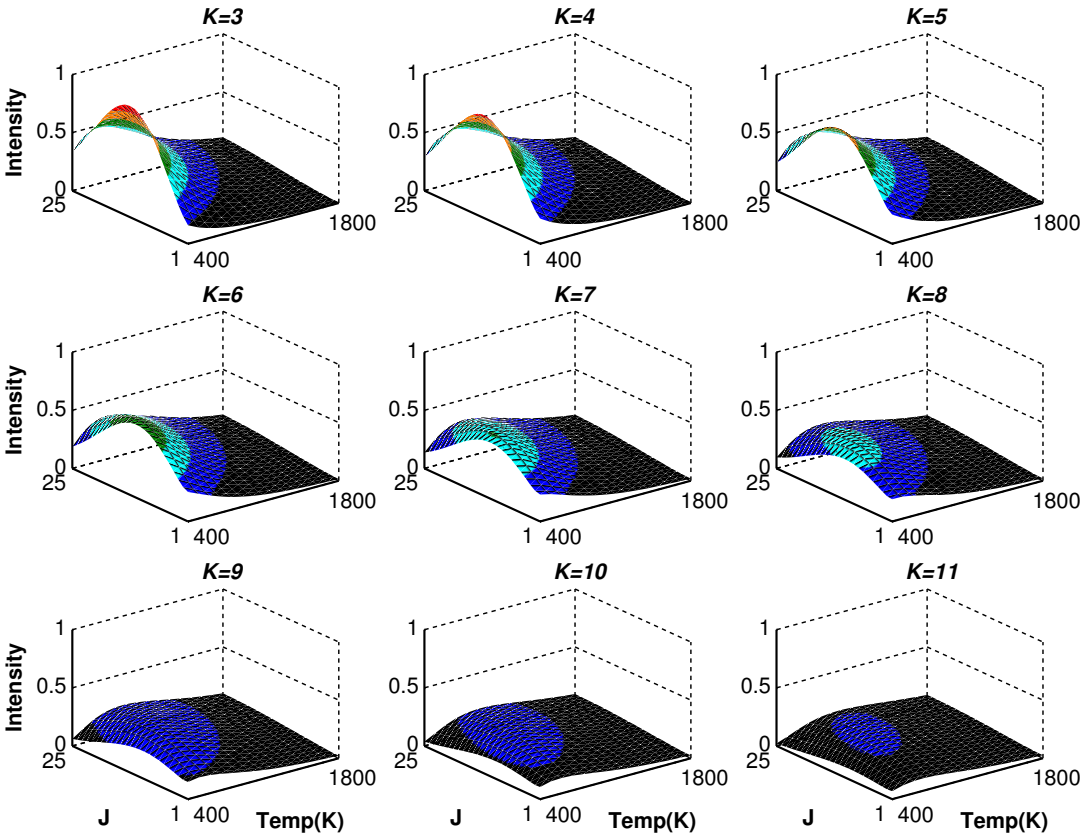

Figure 3.20: Combined formaldehyde branch intensity and Boltzmann fraction distribution for various K for rR and pP branch (i.e. $\Delta J = \Delta K = \pm 1$). Vibrationless ground-state. Note: rR branch translated -1 units for both J and K.

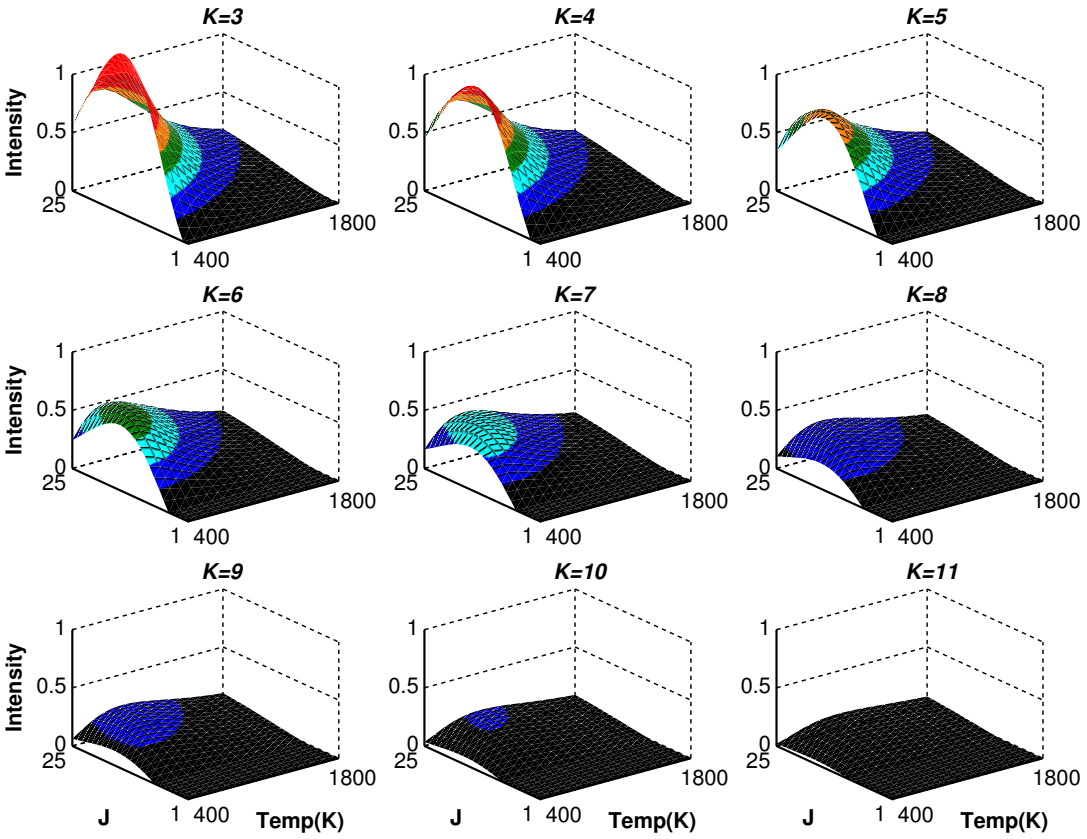

Figure 3.21: Combined formaldehyde branch intensity and Boltzmann fraction distribution for various K for pQ and rQ branch (i.e. $\Delta J = \pm 1, \Delta K = 0$). Vibrationless ground-state. Note: rQ branch translated -1 units for K.

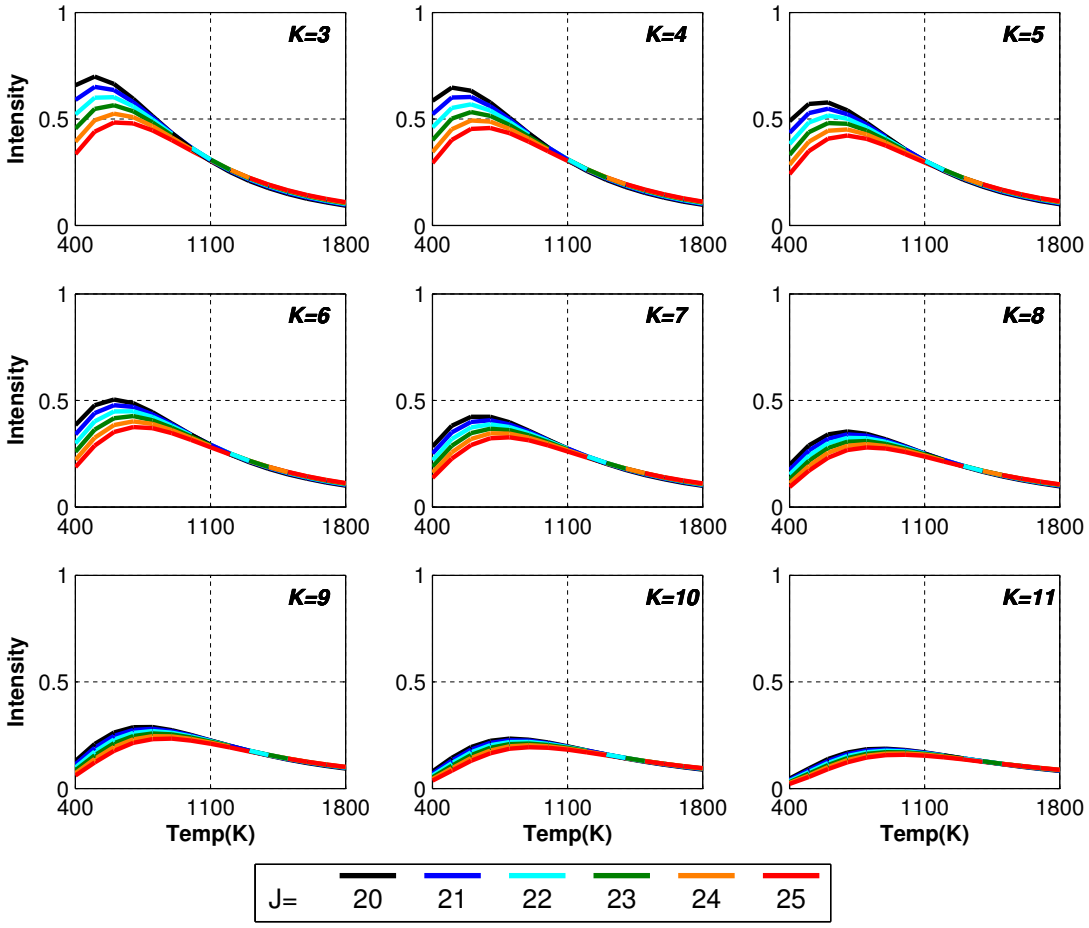

Figure 3.22: Combined formaldehyde branch intensity and Boltzmann fraction distribution for various K for rR and pP branch (i.e. $\Delta J = \Delta K = \pm 1$). Vibrationless ground-state. Note: rR branch translated -1 units for both J and K.

While the surface plots give a good visual indication of the trends of the various branches, two dimensional line plots may give a more definitive visualisation. Figures 3.22 & 3.23 show the same information as the surface plots of Figures 3.20 & 3.21, but now as a series of lines.

Selection of the best excitation scheme is dependent on a combination of the maximum signal intensity, and the temperature independence of the intensity. While it is possible to correct for the temperature dependency of the recorded signal, preferentially the extent of the required corrections will be kept to a minimum.

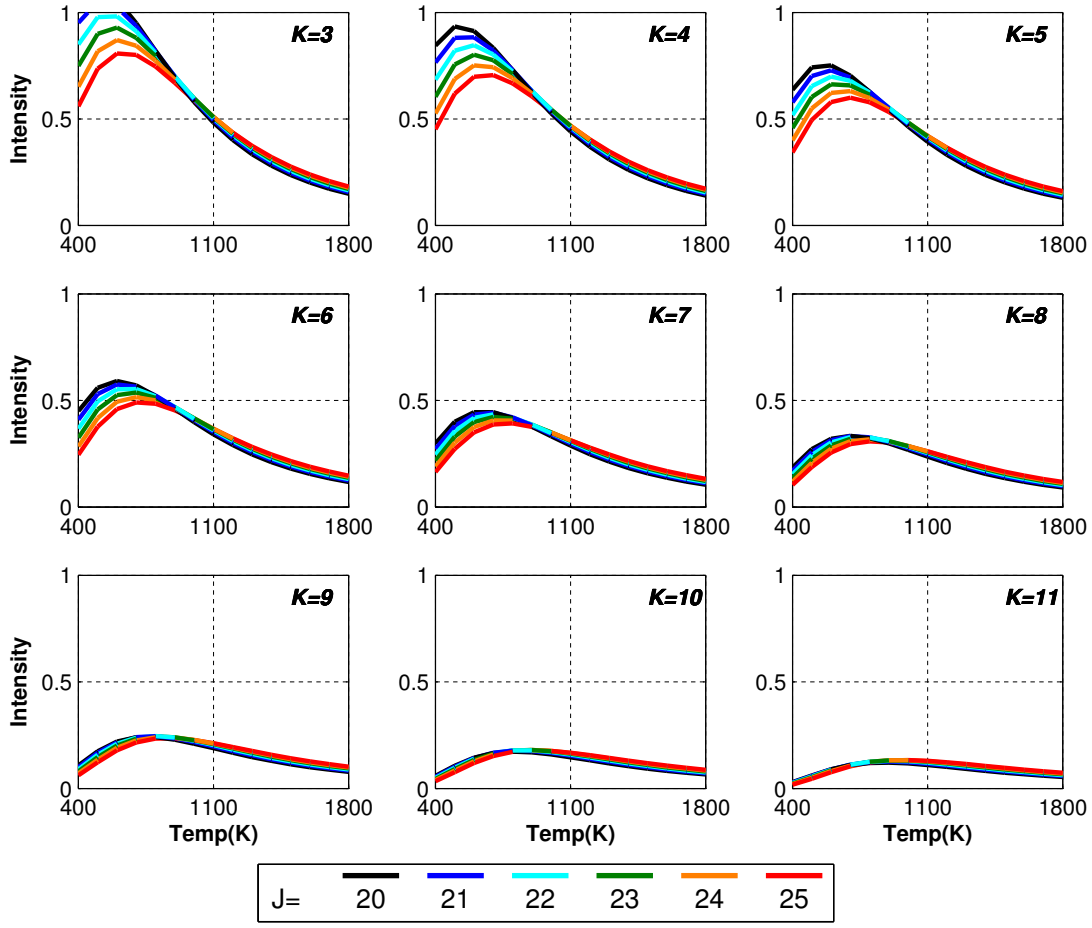

Figure 3.23: Combined formaldehyde branch intensity and Boltzmann fraction distribution for various K for pQ and rQ branch (i.e. $\Delta J = \pm 1, \Delta K = 0$). Vibrationless ground-state. Note: rQ branch translated -1 units for K.

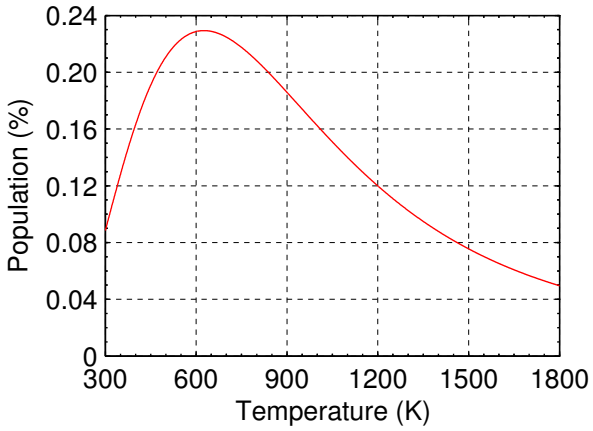

Figure 3.24: Temperature dependence of selected formaldehyde excitation scheme (X-state, $v'' = 0$, $J'' = 21$, $K'' = 5$).

3.6.6 Formaldehyde Excitation Scheme

In light of examination of the previously used excitation schemes, the electronic excitation scheme to be used is $A - X$, and the vibrationally, the $2_0^1 4_0^1$ scheme (at 339nm). The analysis presented in the preceding section, coupled with experimental testing, suggested that the ${}^pQ_{21}(5)$ line be selected.

$$H_2CO - \text{LIF} \ : \ A - X \ \left(2_0^1 4_0^1\right) \ {}^pQ_{21}(5)$$

From Dieke & Kistiakowsky [38] this excitation corresponds to 29,339.62 cm^{-1} (340.836 nm).

With the excitation scheme identified, the dependence on temperature is presented in Figure 3.24. From Figure 3.24 it is apparent that there is a significant dependence of the selected ground-state population on the temperature. Clearly correction for this population distribution will need to be made based on the corresponding temperature measurements recorded simultaneously with the H_2CO-LIF.

3.7 Rayleigh Cross-Sections

The principle behind converting Rayleigh scatter to temperature was introduced in §2.5.2. For calibration from a known reference condition, equation 2.57 may be applied;

$$\frac{I_R}{I_{R,ref}} = \frac{\sigma_{eff}}{\sigma_{eff,ref}} \frac{T_{ref}}{T} \tag{2.57}$$

Apparent from equation 2.57 is that the Rayleigh cross-section (σ) needs to be determined, or at least estimated. For a gas mixture, the Rayleigh cross-section may be found from equation 2.53 ($\sigma_{eff} = \sum_i X_i \sigma_i$) and is clearly dependent on the constituent species concentration.

The Rayleigh cross-section for each species is determined from Namer & Schefer [86]. The quoted Rayleigh cross-sections are presented for irradiance at 488nm, whereas for this experiment 532nm is used. To convert the Rayleigh cross-section to a different wavelength, the following relationship is used;

$$\sigma_2 = \sigma_1 \left(\frac{\lambda_1}{\lambda_2} \right)^4 \tag{3.18}$$

The calculated Rayleigh cross-sections from Namer & Schefer [86], after correction to 532nm, have been verified to the available values in Masri et al. [74].

For each flame condition, at various strain rates, a set of OPPDIF calculations have been performed. The resulting major species concentrations have been used to determine the Rayleigh cross-section across the reaction zone. Figure 3.25 presents an example of the Rayleigh cross-section plotted against the axial distance for a representative flame condition. Details of this calculation are included in Appendix A.5. Here, the axial distance is arbitrary, with X=0 indicating the fuel side and X=1 the oxidiser side. Overlaid on Figure 3.25 is the OH profile (in arbitrary units) to indicate the location of the reaction zone.

Of particular note from Figure 3.25 is that the Rayleigh cross-section is constant from the reaction zone (as indicated by the OH) to the oxidant stream, X=1. This similarity in Rayleigh cross-section is because the coflow itself consists of

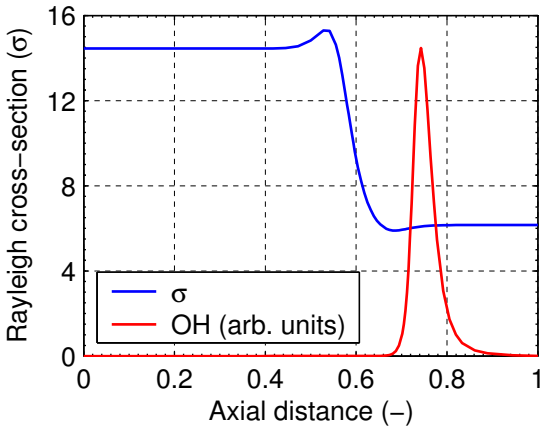

Figure 3.25: Rayleigh cross-section variation across width of reaction zone. Fuel: C_2H_4/H_2, 300K. Oxidant: 3% O_2, 1100K.

combustion products and hence has a very similar composition to the reaction zone.

In order to apply the Rayleigh cross-section to the temperature images, the Rayleigh cross-section has been mapped to a non-dimensional temperature, τ, defined as;

$$\tau = \frac{T^* - T^*_{min}}{T^*_{max} - T^*_{min}} \tag{3.19}$$

In equation 3.19, T^*=T/σ, where the Rayleigh cross-section is evaluated at the location corresponding to the temperature. T^*_{min} is representative of the unreacted jet fluid, as it will have a high Rayleigh cross-section and lowest temperature, both leading to a low T^* value. Conversely, T^*_{max} indicates the peak temperature in the reaction zone. Note that on the lean side of the reaction zone, the non-dimensional τ becomes meaningless with regard to the Rayleigh cross-section since the Rayleigh cross-section remains essentially constant from the centre of the reaction zone to the coflow (Figure 3.25). Figure 3.26 presents the Rayleigh cross-section plotted against the non-dimensional temperature, τ (for the same conditions as Figure 3.25).

For each flame condition, at a range of strain rates, a series of plots similar to Figure 3.26 are produced. It is found that over a wide range of strain rates

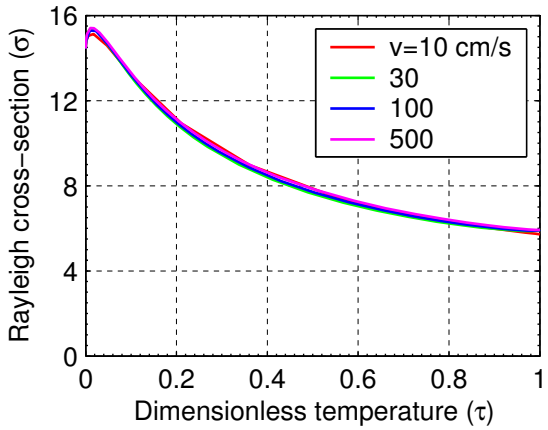

Figure 3.26: Rayleigh cross-section variation as a function of non-dimensional temperature, τ for a range of velocities. Fuel: C_2H_4/H_2, 300K. Oxidant: 3% O_2, 1100K.

the lines overlap, indicating that a single relationship may be developed for a particular flame condition.

Due to the very high Rayleigh cross-section of propane, to reduce the high gradient in the σ-curve, for C_3H_8/H_2 flames a relationship based on $1/\tau$ is used instead. Nevertheless, the same principle is used.

3.8 Data Processing

The data processing consists of a series of stages, some of which are common to each scalar image, whilst some are species specific. Three basic steps may be identified: spatial matching, where the images from each of the cameras are aligned so that each pixel in each image corresponds to the same point in the flame ; corrections, which involve correcting the images for imperfections within the various experimental systems ; quantification, where the values in the images are turned into identifiable values.

3.8.1 Image Matching

It is practically impossible to have three cameras all imaging exactly the same area so that each pixel within the images exactly matches. It is necessary to undertake a series of steps so that the images do in fact all image the same area. So that a common set of reference points can be identified within each image, at the beginning and end of each data set images are recorded of a transparent target with a grid printed on it. This grid image forms the basis of the image matching procedure.

Firstly, referring back to Figures 3.6 & 3.7, because there are cameras on either side of the imaging plane it is noted that the images from the various cameras will appear back-to-front. Furthermore, the images from the dichroic mirror will in turn be opposite to the other images recorded on that side of the imaging plane. Simple image reversal is applied where necessary to ensure the correct orientation of each image.

Once certain that each of the images includes a shared region of the image (and in the correct orientation) a three-point image matching procedure is applied. By identifying three unique points in a pair of the images, triangulation algorithms are used as necessary to translate, resize, and rotate the first pair of images so that the initial three points now share the same pixel co-ordinates in both of the first pair of "matched" images. The resultant co-ordinates of the three points are then matched to the third image, so that finally all three images are spatially matched.

The matched images are subsequently rotated so that the raster orientation (rows in the image) aligns with the laser sheet propagation.

3.8.2 Image Anomalies

Due to potential interferences from unavoidable scatter, some of the images contain artefacts which either need to be rectified, or cause a particular image to be excluded. If the original image contains too many pixels above a certain threshold then the image is simply discarded.

Despite filtering of the gases, particulate matter from the environment leads to Mie scatter from small particulate matter (dust). Providing an image does not contain too much dust interference (in which case it would have been discarded because of too many high valued pixels) measures are taken to "clean" the image. Since Mie scatter is much stronger than the LIF and Rayleigh signal, dust interference manifests itself as regions with higher pixel intensities than the surrounding area. The high gradients which surround the high pixel regions enable the dust particles to be identified. If the gradients exceed a certain threshold, then the surrounding pixels are used to fill the "islands" that are formed.

3.8.3 Background and Dark-Charge Correction

For each species, a background image is subtracted from the raw data image to account for extraneous signal — a combination of dark-charge from the CCD array and signal from inanimate objects. The background image is found by blocking the laser, so that any signal detected is due to non-laser sources. It was found that when laser was blocked, even in a highly luminous environment, because of the very short gate-width, the only signal remaining was due to CCD dark-charge. Similarly, when the flame was extinguished and the laser fired no LIF signal was recorded, and only CCD dark-charge was measured. These two observations give confidence to not requiring a background other than the CCD dark-charge needing to be stripped from the LIF data. For all cases, when the other laser systems are stopped no change is noted in the remaining detection system, confirming the independence of the systems.

3.8.4 Detector Attenuation

Vignetting of the detection optics results in non-uniform light response over the entire image. To account for this, a uniformly illuminated target is imaged. The data images are simply normalised by the uniform target image.

3.8.5 Laser Power and Profile Corrections

The power and profile of the laser beam varies between pulses, particularly for the dye lasers. The variation in the laser energy affects the resultant signal, it is therefore necessary to make corrections for the changes in the laser beam. The laminar slot burner included in the imaging area is assumed constant across the sheet height and between laser pulses, and may be used as a reference source to normalise by.

The region of the image containing the signal from the slot burner is summed in the direction of the laser propagation, giving the distribution of laser energy across the sheet height. The entire image is normalised by this profile.

The normalised slot burner signal is then used to scale the entire image to a constant value, thereby correcting for variations in the laser energy between pulses.

To ensure that the sheet correction has been successful, the profile of the corrected slot burner is again determined. If the ratio between the minimum and maximum values along the sheet height of the normalised slot burner exceeds a predetermined value, the image is flagged as being invalid.

3.8.6 OH-LIF Quantification

Quantification of the OH-LIF is based on the previously defined equation 2.55;

$$n = n_{cal}\left[\frac{I}{I_{cal}} \cdot \frac{f_{cal}}{f} \cdot \frac{E_{L,cal}}{E_L} \cdot \frac{Q}{Q_{cal}} \cdot \frac{g(\nu_0)_{cal}}{g(\nu_0)}\right] \tag{2.55}$$

The peak OH from the laminar slot burner is used as the calibration point. The particular OH-LIF excitation scheme outlined in §3.5 was chosen so that, over the temperature range of interest, the Boltzmann fraction is relatively constant (Figure 3.16) and variation is considered negligible. Corrections are made for the laser energy (§3.8.5) so that each image has already been scaled for laser energy variations. Given the similarity of the jet flame and the laminar diffusion reference flame, the spectral overlap term is also considered negligible. Equation 2.55 may now be written as;

$$n_{\mathrm{OH}} = n_{cal}\left[\frac{I}{I_{cal}} \cdot \frac{Q}{Q_{cal}}\right] \tag{3.20}$$

While equation 3.20 is simplified from equation 2.55, there are still terms which need to be determined in order to apply this equation to the data. The OH number density at the location of peak OH in the calibration flame is found from laminar flame calculations. Over a range of strain rates the peak OH number density is quite constant, and found to be $2.2{\times}10^{16}$ cm^{-3}. The LIF intensity terms are simply given by the pixel values from the corrected OH-LIF images. Since the laser energy is scaled from the signal from the calibration burner, the I_{cal} term is constant, and I is simply the OH-LIF image. The remaining terms are the quenching rates.

To determine the quenching rates, a series of laminar flame calculations are performed, at a range of strain rates for each of the flame conditions to determine the major species concentrations. From the constituent species, at each point in the flame the combined quenching rate is found.

For a gas mixture of i species, the quenching rate is given by;

$$Q = \sum_i n_i \sigma_i v_i \tag{3.21}$$

Where n_i is the number density, σ_i the collision cross-section and v_i the average relative velocity between collision species and the quenched species, given by;

$$v_i = \left[\frac{8kT}{\pi\mu_i}\right]^{1/2} \tag{3.22}$$

With μ_i representing the reduced mass of the colliding species (subscript i) and the quenched species (subscript q);

$$\mu_i = \frac{m_i \cdot m_q}{m_i + m_q} \tag{3.23}$$

Where m represents the mass of each molecule ($m = u \times M$); the molecular weight (M) multiplied by the atomic mass unit ($u = 1.66 \times 10^{-27}$ kg).

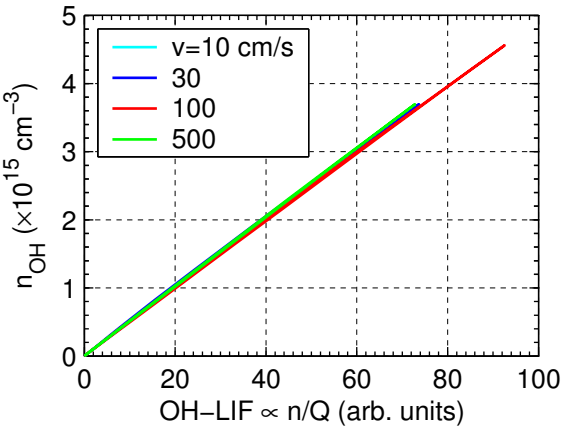

Figure 3.27: Example of OH-LIF quenching rates at different inlet velocities. Fuel: C_2H_4/H_2, 300K. Oxidant: 3% O_2, 1100K.

The collisional cross-sections (σ) for each species are obtained from temperature dependant polynomial fits of the data from Garland & Crosley [45]. It should be noted that the quenching cross-section is not only dependent on the temperature, but also the energy state of the molecules. The quenching cross-sections at various vibrational levels in the excited A-state have been observed to be similar however [89]. Moreover, quenching cross-sections exhibit weak dependence on rotational level for temperatures above 1000K [90]. It is therefore a reasonable assumption to use only the v'=0 quenching rates.

In addition to quenching, rotational and vibrational relaxation effects also occur within the flame. The broadband detection scheme used in this experimental arrangement for the OH-LIF covers the range 270–340nm. This range is sufficient to include fluorescence to the X-state (v''=0) from either v'=0 or v'=1, such that either RET or VET in the A-state will not affect the fluorescence.

To examine the variation in the quenching rate throughout the flame, the OH number density (n_{OH}) is plotted against OH-LIF ($I \propto n/Q$), in effect, creating a look-up table of the OH number density for the particular OH-LIF values. An example of the results of the quenching calculations for the C_2H_4/H_2, 3% O_2 flame is shown in Figure 3.27 for a range of strain rates (where the strain rate varies with the imposed inlet velocities). Details of these calculations are included in Appendix A.6.

The results seen in Figure 3.27 show a linear relationship, indicating a constant quenching rate, which is given by the slope of the line. For each flame condition a plot similar to Figure 3.27 is generated. It is found that in all cases the relationship appears relatively linear, indicating that for each flame condition a single quenching rate may be used. Upon closer inspection it is noted that the relationship is not completely linear, and that different strain rates slightly alter the slope, but in general it is considered sufficient to assume linearity. Furthermore, at very low OH-LIF values ($\ll$5%) the linearity can deviate more significantly, but the accurate quantification at very low concentrations in comparison to the peak is not overly important.

3.8.7 H_2CO-LIF Corrections

In the preceding section, the process to quantify LIF of OH was described. Quantification of H_2CO via a similar means is not as easily applied. The quenching rates for H_2CO are not sufficiently developed to enable routine corrections for quenching. While it may be possible to try and determine quenching rates experimentally, it is deemed adequate for the purposes of this investigation to assume that the quenching rate remains approximately constant. For OH, the calculations presented in §3.8.6 suggest that the quenching rate remains constant over the region of interest. While this may not necessarily be the case for H_2CO as well, it seems a reasonable assumption that the quenching rate will be relatively close to being constant, albeit with some uncertainty.

Referring back to equation 2.55, an important aspect to consider for the H_2CO-LIF signal is the ground-state Boltzmann fraction. Calculations of the ground-state Boltzmann fraction for H_2CO were presented in §3.6.6. From Figure 3.24 it is clearly apparent that the Boltzmann fraction varies significantly over the expected temperature range of interest. As such, unlike for OH, it is necessary to correct for the H_2CO Boltzmann fraction.

To make corrections for the ground-state Boltzmann fraction, the corresponding temperature image is used in conjunction with the profile shown in Figure 3.24.

3.8.8 Rayleigh / Temperature Quantification

The Rayleigh image processing described up to §3.8.5 has been corrected for dark-charge, detector attenuation and laser power and profile variations. Due to the elastic nature of Rayleigh scatter, experimental elimination of stray laser light is difficult, and additional background needs to be removed. Whilst a background (dark-charge) has already been removed from the Rayleigh images (§3.8.3), following corrections for laser power, an additional background needs to be removed to account for the laser scatter.

The number of surfaces around the slot burner and chimney is significantly greater than around the JHC burner, as such, additional background due to extraneous scatter needs to be removed for the part of the image around the slot burner as compared to the JHC burner. For simplification, a single value of background is determined for the slot burner side of the images and another single value for the JHC burner side of the image.

The process used to convert the Rayleigh data to temperature has been outlined in §2.6.3, using equation 2.57;

$$\frac{I_R}{I_{R,ref}} = \frac{\sigma_{eff}}{\sigma_{eff,ref}} \frac{T_{ref}}{T} \tag{2.57}$$

Applying equation 2.57 to the data images is performed in steps; firstly the division by the Rayleigh image, and then the Rayleigh cross-section is applied. The first step results in a temperature image, denoted T^*, which is yet to be corrected for Rayleigh cross-section (i.e. $T^*=T/\sigma$).

In §3.7, a relationship was developed between the Rayleigh cross-section (σ) and a non-dimensional temperature (τ, equation 3.19), based on the $T^*(=T/\sigma)$ image. An example (for a C_2H_4/H_2, 9% O_2, Re_{jet}=10,000 flame) of a corrected Rayleigh image, and the subsequent T^* image is shown in Figures 3.28a & b, respectively. Clearly apparent from Figures 3.25 & 3.26 is that the Rayleigh cross-section on the fuel-rich side varies significantly from the unreacted fuel to the reaction zone. Since it is only on the fuel-rich side that the intermediate Rayleigh cross-section values need to be determined, it is necessary to demarcate the fuel rich and lean sides. Depending on the specific flame conditions, either the corresponding OH

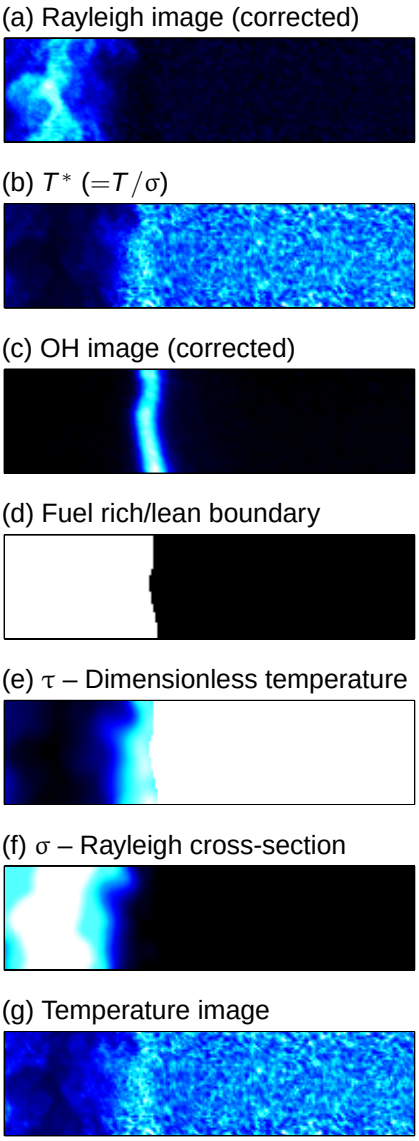

Figure 3.28: Processing of Rayleigh image to temperature

or formaldehyde image is used. Preferentially, OH is used to demarcate fuel rich/lean. For lifted flames however, the OH level cannot be used, in which case formaldehyde is used. Figure 3.28 shows the case of using maximum OH-LIF value in each row of the corrected OH image (Figure 3.28c) to mark the fuel rich/lean boundary, resulting in a mask as shown in Figure 3.28d. Using the T^* image in conjunction with the OH mask the τ image is generated, as in Figure 3.28e. From the τ image, a series of intermediate levels on the fuel-rich side are identified, and for each level the corresponding Rayleigh cross-section is determined, leading to a σ-image, as in Figure 3.28f. By combining the images of T^* and σ the temperature is determined, as in Figure 3.28g.

3.9 Error Analysis

3.9.1 General Error Sources

There are potential sources of error common to all of the measurements in the experiment, aside from the specific issues relating to each of the species measurements which are dealt with in the proceeding sections.

Flowmeters

Each of the gas flows for the JHC jet and coflow are measured using tube and float type flowmeters. Inaccuracies of the flowmeters will lead to differences in both the gas velocity and composition, affecting the overall accuracy and repeatability of the flame conditions. The flowmeter specifications list an accuracy of 2% with repeatability of 0.5%, both at full-scale reading [1]. While efforts were made to maintain the flowmeters operating near the full-scale, this is not always possible and so the flowmeter errors might be a little greater than the quoted values. Furthermore, the pressure gauges used in conjunction with the flowmeters will also lead to a further source of error, and are expected to be of a similar order as for the flowmeter itself.

Measurement errors

In addition to the inherent device inaccuracies of the flowmeters, and other measurement devices (e.g. thermocouple, calipers, etc.) there is a possible inaccuracy in the reading and recording of the values from these devices. While every effort is taken to ensure that measurements are accurate, slight inaccuracies may occur in collecting the flowrates, jet diameter (which may be subject to slight thermal expansion during operation of the burner), temperature of the coflow, and also the temperature of the inlet gases, affecting the volumetric flowrate both at the exit and through the flowmeters.

The results of this work have subsequently shown that the jet velocity has minor effects on the composition of the reaction zone, and so uncertainty of the gas velocity due to issues with the flow rates is not expected to present a problem for the experiment. Inaccuracy of the gas composition, particularly of the coflow, may lead to more noticeable effects however. Nevertheless, uncertainty of the gas composition due to slight errors with the flow rate measurements will be relatively small, and certainly does not effect the general trends which are identified.

Coflow composition

The composition of the coflow is not only dependent on the gas composition through the flowmeters, but also the combustion properties of the secondary burner. In determining the properties of the coflow, the composition was assumed to be comprised of the products of complete combustion. The stable appearance of the flame, and the measurements of the excess O_2 concentration supports this assumption, but some species apart from those associated with complete combustion may be present, and have minor effects on the flame front. When comparing different flame conditions it is also assumed that the behaviour is constant throughout, which may not necessarily be the case, although measurements of coflow temperature and the visual appearance throughout the course of the experiments indicate that the secondary burner was consistent. As with the gas composition noted in the preceding paragraph, the effect of variation in the coflow composition is expected to be rather small, and is definitely not likely to alter the trends between different coflow conditions.

Reference burner

The laminar slot burner is used for reference purposes to enable laser power and profile corrections and also for calibration purposes. It is assumed that the species distribution throughout the flame along the laser sheet height is constant, and also remains constant between laser pulses. The assumption of constant species distribution over the sheet height has practical limitations, but based on the corrected images, this normalisation technique yields surprisingly good results. Similarly, between laser pulses the species concentration seems to remain very constant, as corrected flat-flame images have minimal inter-pulse variation, which are dealt with in the following sections.

Processing parameters

For each of the laser measurements it is necessary to apply some processing before the images can be quantified. The general processing structure was outlined in §3.8, and involves the determination of several parameters within the processing algorithms, including; dark-charge, background, illumination uniformity, etc. A systematic approach is used to determine these parameters, but there is potential for inaccuracies in these values, which will subsequently lead to slight inaccuracies in the corrected measurements. In general the final result is quite insensitive to the correction/processing parameters, and in situations which are more sensitive, even greater care is taken to ensure that the values selected accurately represent the required variable.

3.9.2 OH-LIF

To validate the calibration of OH-LIF using the laminar slot-burner as a reference source, the OH number density in a flat-flame may be compared to premixed flame calculations. The same technique to quantify the images is used as described in §3.8.6 but replacing the jet flames with a premixed flat-flame, which consists of a sintered bronze plate which fits onto the JHC outer annulus via an extension tube.

Figure 3.29: Image of slot burner reference flame (left) and premixed flame front (right)

Premixed flame	Peak OH (cm^{-3})	Equilibrium OH (cm^{-3})
Experimental	1.15×10^{16}	0.70×10^{16}
Calculated	1.02×10^{16}	0.74×10^{16}

Table 3.3: Comparison of peak and equilibrium OH levels in premixed flame found experimentally and from calculations

As was noted in §3.2.3 the flat-flame burner can be operated in two premixed modes; a "flat" mode, and a premixed "lifted" flame mode where the flame is attached to the burner face only at a few locations (Figure 3.5). In the "flat-flame" mode there were significant heat losses to the burner, affecting the ability to model this situation accurately. As such, whilst not strictly a flat-flame, the lifted flame generated by the flat-flame burner does indeed provide a steady premixed flame suitable for validation purposes. Furthermore, with the premixed flame separated from the burner face, optical access is available across the full width of the flame front, enabling both the peak and equilibrium OH number density to be identified. A sample image of the OH-LIF from the laminar slot burner and the premixed flames is shown in Figure 3.29.

Shown in Figure 3.29 are the locations used for determining the OH number density. The left side of the image is the reference flame. In the premixed flame (right side of image), both the location of peak and equilibrium OH are identified.

Table 3.3 presents the peak and equilibrium OH number density found experimentally, and from the PREMIX code of the Chemkin package, with GRI-Mech 3.0 mechanism. It is apparent that the experimentally and theoretically calculated OH number density are in good agreement, deviating only by around 10%, suggesting that the proposed calibration technique is sound.

The calibration gives good agreement between the two techniques, nevertheless, there are still a number of sources of errors. Amongst numerous sources of error, some of the most significant follow.

Referring back to equation 2.55, and its simplification to equation 3.20, it was assumed that the Boltzmann fraction and the spectral overlap is constant throughout, and that the laser energy was perfectly corrected for. It is known from Figure 3.16 that the Boltzmann correction is not constant (∼10% variation across the temperature range shown), and similarly, the spectral overlap will not be constant. Furthermore, the laser energy corrections are also a source of errors. By imaging of the premixed flat-flame in its "flat" mode, the standard deviation throughout the data set was found to be 4.4%, primarily due to inaccuracies in the laser energy correction.

The assumptions relating to a constant quenching environment will also introduce errors in a number of ways. It is assumed that the composition obtained from the strained laminar flame calculations accurately represents the composition within the MILD jet flames, and that only major species effect the quenching rate. It is also assumed that a single quenching rate is appropriate throughout the region of interest, and that it does not change with flame stretch. The calculations suggest that both of these assumptions do in fact introduce errors, and are of the order of 10% for each.

The signal-to-noise (SNR) of the OH-LIF measurements is dependent on the specific flame conditions, but is typically better than 40:1.

The OH-LIF is detected using a dichroic mirror, covering the range 270–340nm. The excitation wavelength of 283nm is within this range, and so elastic scatter is not blocked by the dichroic, although the images show no evidence of such interference however. Stokes-shifted Raman scatter from C_2H_4 also falls within the detection range of the OH-LIF camera. As the LIF signal is much stronger, Raman interference does not pose a significant problem. Furthermore, fuel Raman is readily disregarded based on its spatial location relative to the reaction zone. Raman scatter from other fuel species are also within the OH-LIF detection range, but no evidence of such effects is noted.

In the quantification of the OH-LIF it has been assumed that the LIF signal is

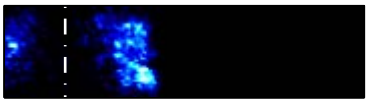

Figure 3.30: Example of raw H_2CO-LIF image

linear with laser energy. The linearity of the OH-LIF has been confirmed, as described in Appendix B.

3.9.3 H_2CO-LIF

The signal-to-noise (SNR) of the H_2CO-LIF varies significantly with the fuel and fuel composition. In the worst case the SNR is ∼5:1, but can be better than 20:1. It is acknowledged that higher SNR for all cases would have been desirable. Being a polyatomic molecule, H_2CO-LIF is inherently weak as the population is distributed over a large number of quantum states. Weak H_2CO-LIF is compounded in nonpremixed flames due to the low H_2CO concentrations in comparison to premixed and partially premixed flames.

It is acknowledged that the H_2CO signal may experience some encroachment of vibrational Stokes-shifted Raman scatter from H_2 passing the detection filter. This interference is only expected to be minor, and restricted to radial locations close to the centreline and have little effect near the flame location. Figure 3.30 presents a raw data image of the H_2CO signal near the jet exit for a natural gas / hydrogen flame. It is apparent that along the jet centreline, where the H_2 number density is highest, the H_2CO signal is low, supporting the notion of minimal effect of H_2 Raman interference. For some of the later flame conditions to be considered, it will be noted that H_2CO signal is indeed detected along the jet centreline. The absence of H_2CO signal in the cold coflow conditions of Figure 3.30 suggests that the conditions in the flames considered later are responsible for the H_2CO distribution, rather than interferences.

As outlined in §2.6.2, the excitation band selected for H_2CO has been reported to have lower broadband interference than other H_2CO schemes. Analysis of the measurements collected during the experiment have subsequently shown that the trends in the H_2CO signal at different flame conditions do not follow the trends of

increased PAH formation. This suggests that if there is any PAH interference, it is not affecting the conclusions of the work. This point is even further re-iterated from laminar flame calculations presented in §6.6.

Despite these issues, the H_2CO-LIF is sufficient to obtain reasonable understanding of the parameters that control its concentration and spatial distribution.

3.9.4 Temperature

The conversion of the Rayleigh image to temperature (as described in §3.8.8) is quite straight-forward in principle, but potentially introduces some additional errors to the Rayleigh signal itself.

Scaling the Rayleigh image for laser power and profile variations introduces a potential source of error if the reference region contains erroneous signal due to particulate matter, or other undesired effects. Attempts are made to discard images where the laser corrections have been unsuccessful, but it is possible that some of these images remain in the data set. Analysis of the data sets indicates that obviously flawed temperature images are very rare, and after applying filtering do not have any distinguishable affect on the mean or RMS values. The shot-to-shot variation from the flat-flame burner is $\sim$2.5%, suggesting that laser power and profile are usually well accounted for. The signal-to-noise (SNR) of the corrected Rayleigh images is around 10:1.

As undesired Rayleigh scatter from objects is near impossible to completely avoid, there is a component of background which needs to be removed. Throughout the course of the experiment, slight changes to the physical environment in turn lead to changes in the background on the Rayleigh data. To compensate for the background, for each flame condition based on regions where the temperature is known, the background value is determined, and subsequently removed from the data. This process is done with great care, but potentially leads to another source of error since any uncertainty in the temperature of the known points will be incorporated into uncertainty in the measurement itself. Nevertheless, the errors introduce by this technique are limited to the order of a few percent.

To convert the Rayleigh to temperature it is necessary to determine the Rayleigh

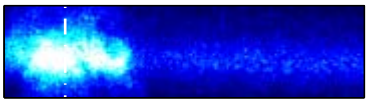

Figure 3.31: Example of raw Rayleigh image

cross-section, which varies with the composition from the jet through the reaction zone to the coflow. The process to assign the Rayleigh cross-section at various points in the flame was outlined in §3.7. In brief, the procedure involves splitting the image into fuel rich and fuel lean sides of the reaction zone. Based on laminar flame calculations, the Rayleigh cross-section on the fuel lean side remains constant from the location of peak OH to the coflow. On the fuel rich side, a single monotonic function exists between the peak OH and the unreacted fuel jet, which relates the Rayleigh cross-section (σ) to the variable T^* (where $T^*=T/\sigma$). This process relies on a number of assumptions, notably the ability to accurately distinguish the fuel rich and lean sides from the OH, and the ability of the laminar flame calculations to capture the major species concentration (and that the major species concentrations are sufficient to determine the Rayleigh cross-section of the mixture).

Demarcation of the fuel rich and fuel lean sides of the reaction zone from OH is a relatively reliable process, but troubles can arise if the OH layer becomes highly convoluted or locally broken. In situations where the OH is convoluted (e.g. Figure 6.10), there may be two (or more) peaks in OH. The algorithm detects the maximum OH in any particular row, and so may incorrectly identify the fuel rich/lean boundary. If the OH layer is broken due to extinction, or in lifted flames, identifying fuel rich and lean sides can become difficult. The use of formaldehyde to identify the flame front location in such situations alleviates this issue. These problems occur in only a few of the flame conditions, and even then, in only a limited number of images for those conditions.

In some of the images to be presented, the temperature rise across the reaction zone appears indistinguishable. The species measurements indicate a reaction, and flame calculations show a modest temperature rise. The lack of discernable change in temperature is also reflected in the Rayleigh images. To demonstrate this, Figure 3.31 shows a raw Rayleigh image. In this sample image, no change in

Rayleigh scattering is apparent in the region corresponding to the reaction zone, between the jet (centreline marked with dashed vertical line) and coflow (right-hand side of image). Without delving into the flame measurements, a reaction is evident for this flame. It is not clear why a temperature rise is not detected for some of the flames. The flames do not show evidence of soot, and any possible PAH would have a concentration far too low to influence the Rayleigh scattering. Since the Rayleigh images do not show signs of a density (i.e. temperature) change across the reaction zone, the lack of temperature change is not attributed to the Rayleigh to temperature conversion process. This is believed to be a genuine effect, or related to an unidentified local interference. The low temperature rise for certain flame conditions does not present a major problem. It is the trends in temperature that are most important.

At the furthest downstream measurement location, the occurrence of convolution (and extinction) becomes more frequent, and more significant, but is still relatively minor. Furthermore, at the most downstream location the assumption of unreacted fuel being present may not be valid due to mixing processes. Even though measurements further downstream are more susceptible to errors in the temperature, the results tend to indicate that the extent of any inaccuracies are comparatively minor. At most, the errors in temperature are believed to be of the order of 10%, but typically better than this.

3.10 Experimental Conditions

The jet in hot coflow (JHC) burner consists of two independent systems; the jet and the secondary porous bed burner. The flowrates and the operating conditions are completely separate, and so may be considered individually. A laminar slot burner is also incorporated into the experimental system. The gases for each of the burners are controlled separately, through a central gas distribution system.

Methane	91.99%
Ethane	4.28%
Propane plus (*)	0.24%
Carbon Dioxide	2.56%
Nitrogen	0.93%

Table 3.4: Natural gas composition – volumetric basis. (* Propane plus refers to propane and also includes higher-order hydrocarbons.)

3.10.1 Gas Supply

The natural gas used in the experiments (for the JHC secondary burner, slot burner, and for some JHC jet conditions) is supplied from a high-pressure town-gas line. Table 3.4 shows the average gas composition (as provided by the gas supplier, Origin Energy). It shows that the main constituent is methane, while ethane and other higher-order hydrocarbons are present as well.

The air for the experiments was supplied by an air compressor. This air was fitted with both a 0.5 micron filter for removal of particulate matter and also included a water trap, but the air was not dried. The presence of humidity in the air has been suggested that this may effect the levels of NO within a flame [6], but this is not expected to have any impact on this experiment.

Aside from natural gas and air, other gases were supplied from gas cylinders. The supplier lists the purity of each gas as follows; nitrogen – 99.99%, hydrogen – 99.5%, and ethylene – 99%. Liquified petroleum gas (LPG) was used in-lieu of pure propane, and although it contains many other species (notably butane), it serves the purpose of providing a different fuel type.

3.10.2 JHC Burner – Coflow Conditions

The coflow of the JHC burner consists of the combustion products from a pre-mixed porous bed secondary burner. To vary the O_2 concentration of the coflow, whilst maintaining a constant temperature and velocity, the fuel flow is held constant, and the balance between the air and nitrogen is altered. Table 3.5 shows the flow rate into the secondary burner for two different O_2 levels.

Excess O_2 (mol/mol)		3% O_2	9% O_2
Inlet flowrate (L_n/min)	Nat Gas	5.5	5.5
	H_2	7.0	7.0
	Air	96	148
	N_2	79	27
Premixed combustion products (mol/mol)	O_2	3%	9%
	N_2	84%	78%
	H_2O	10%	10%
	CO_2	3%	3%
Post-combustion products	Φ	0.72	0.47
	Temp.	1100K	1100K
	$\bar{U}$	∼2.4 m/s	∼2.4 m/s
	Re	∼1400	∼1400

Table 3.5: Coflow parameters

Table 3.5 also includes the mole fraction of the combustion products (assuming complete combustion). The temperature of the coflow was measured to be 1100K for either O_2 level, from which the velocity and Reynolds number have been calculated. The O_2 concentration in the coflow was determined assuming equilibrium conditions, and also measured in-situ.

3.10.3 JHC Burner – Jet Conditions

The jet Reynolds number (jet velocity) and fuel composition are both independently varied to examine the effect of each parameter. The fuel composition is altered in one of two ways; either the primary fuel type is changed (natural gas, ethylene or LPG, each diluted with hydrogen 1:1 vol/vol to reduce soot interference) or for ethylene, the fuel diluent is changed (undiluted, hydrogen, air or nitrogen).

Fuel dilution serves two purposes in this study. Addition of diluents to the fuel reduces soot and other sources of interference for the laser measurements. Each of the diluents used in this study have previously been shown to reduce laser interferences in flames [65]. Diluting the fuel also enables a systematic study of the effect of fuel dilution on the reaction zone under MILD combustion conditions.

Fuel (mol/mol)	Re_{jet}	$\dot{Q}$[L_n/min]	$\bar{v}_{exit}$ [m/s]
CH_4/H_2 (1:1)	5000	24.0	26.4
	10000	48.0	52.9
	15000	72.0	79.3
	20000	96.0	105.8
C_2H_4/H_2 (1:1)	5000	15.3	16.8
	10000	30.5	33.6
	15000	45.8	50.4
	20000	61.0	67.2
C_3H_8/H_2 (1:1)	5000	8.8	9.6
	10000	17.5	19.3
	15000	26.3	28.9
	20000	35.0	38.6
C_2H_4/Air (1:3)	5000	13.6	15.0
	10000	27.2	30.0
	15000	40.8	45.0
	20000	54.4	60.0
C_2H_4/N_2 (1:3)	5000	13.6	15.0
	10000	27.2	30.0
	15000	40.8	45.0
	20000	54.4	60.0
C_2H_4	5000	8.7	9.6
	10000	17.4	19.2
	15000	26.1	28.8
	20000	34.8	38.4

Table 3.6: Jet parameters

Table 3.6 presents the different fuel compositions and the jet Reynolds numbers used in this study. Also included in Table 3.6 is the jet volumetric flowrate (L_n/min) and the bulk jet exit velocity for an exit temperature of 300K. Although some heating of the reactants may occur along the non-insulated length of the jet pipe exposed to the coflow near the top, the effect of this heating is minimal. Previous experience of this burner indicates that the amount of preheating is no more than 50K.